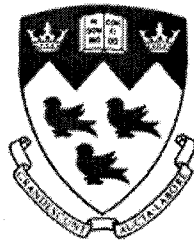


Deflection-Based Design of Fiber Glass Polymer (FRP) Composite Sheet Pile Wall in Sandy Soil

**By
Zeid Bdeir**

November 2001



Department of Civil Engineering and Applied Mechanics
McGill University, Montreal, Quebec

A thesis submitted to the Faculty of Graduate Studies and Research in partial fulfillment of the requirements of the degree of Masters of Engineering

© Zeid Bdeir 2001



National Library
of Canada

Acquisitions and
Bibliographic Services

395 Wellington Street
Ottawa ON K1A 0N4
Canada

Bibliothèque nationale
du Canada

Acquisitions et
services bibliographiques

395, rue Wellington
Ottawa ON K1A 0N4
Canada

Your file Votre référence

Our file Notre référence

The author has granted a non-exclusive licence allowing the National Library of Canada to reproduce, loan, distribute or sell copies of this thesis in microform, paper or electronic formats.

The author retains ownership of the copyright in this thesis. Neither the thesis nor substantial extracts from it may be printed or otherwise reproduced without the author's permission.

L'auteur a accordé une licence non exclusive permettant à la Bibliothèque nationale du Canada de reproduire, prêter, distribuer ou vendre des copies de cette thèse sous la forme de microfiche/film, de reproduction sur papier ou sur format électronique.

L'auteur conserve la propriété du droit d'auteur qui protège cette thèse. Ni la thèse ni des extraits substantiels de celle-ci ne doivent être imprimés ou autrement reproduits sans son autorisation.

0-612-79059-2

Canada

Abstract

Fiber Reinforced polymer composite materials offer great potential for waterfront structural applications due to their excellent corrosion resistance, and high strength to weight ratio.

A successful example is the fiberglass reinforced polymer composite sheet pile wall recently developed and installed as a waterfront retaining structure. Traditional design of sheet pile is strength based and does not account for the deflection. Compared to steel sheet piling, composites are flexible, thus large deflection is generated, both bending moment and shear force must be taken into consideration in the wall design.

The purpose of this thesis is to develop a deflection based design approach for composite sheet pile wall, based on the traditional free-earth support method, but modified to allow the use of deflection criterion. With a simplified earth pressure loading on the wall, the relationship between maximum bending moment and maximum bending deflection and the relationship between maximum shear force and maximum shear deflection were established. 16 case studies were carried out to include walls ranging from 1.5m to 4.5 m tall and water level to wall height ratio from 0.1 to 0.4. Two deflection limits, $L/60$ and $L/100$ were employed in developing the design charts. The results showed that the deflection based method was effective in designing a composite sheet pile wall with controlled deflection, reduced maximum bending moment and adequate penetration depth.

To implement the deflection based design, the proper characterization of flexural rigidity (EI) and shear rigidity (KAG) of the sheet pile panels was vital. Tests were conducted on the connected panels to obtain the rigidities. The flexural rigidity was found to be $495 \text{ KNm}^2/\text{m}$, and the shear rigidity 1493 KN/m . The EI was not sensitive to the spans used. However, the KAG value varied significantly. The failure tests showed that when the deflection of a sheet pile panel subject to 4 point bending reached $L/46$, the tensile strain developed in the panel was only 15% of the ultimate

failure tensile coupon strain, indicating, that tensile failure of sheet pile wall in flexure is not likely to occur.

Abrégé

Les matériaux de composite polymère renforcé de fibre (FRP) offrent un bon potentiel pour les structures en contact avec l'eau, dû à leur excellente résistance à la corrosion et à leur grande résistance au poids.

Un bon exemple est le mur palplanche en matériau composite FRP laminé qui fut récemment mis au point et installé en guise de structure pour contenir l'eau. Le design traditionnel du palplanche laminé tient compte de la tension mais ne tient pas compte de la déflexion. Quand on le compare aux palplanches en acier, le composite offre un élément de flexibilité, ce qui génère une grande capacité de déflexion et tant le moment de courbure comme l'élément de tension doivent être pris en compte lors du design du mur.

Le but de la présente thèse est de développer une approche où le design est axé sur la déflexion pour les murs en composite laminé, élaborés à partir de la méthode traditionnelle de support en terre meuble, mais comportant les modifications nécessaires afin de permettre l'utilisation d'un critère de déflexion. En considérant une charge simplifiée de pression du sol sur le mur, on a établi la relation entre le moment de flexion maximal et la courbure de déflexion maximale, ainsi que la relation entre la force de cisaillement maximale et la déflexion du cisaillement. 16 cas d'étude furent complétés avec des murs qui variaient entre 1,5 m et 4,5 m de haut et le rapport entre le niveau d'eau et le sommet du mur était 0,1 à 0,4. On a utilisé deux limites de déflexion $L/60$ et $L/100$ pour élaborer les tableaux de design. Les résultats montrent que la méthode axée sur la déflexion prouve être efficace dans le design d'un mur palplanche en matériau composite laminé à déflexion contrôlée et quelle réduit le moment de flexion maximale; elle proportionne une bonne profondeur de pénétration.

Pour exécuter le design axé sur la déflexion, une définition adéquate de la rigidité de flexion (EI) et de la rigidité de cisaillement (KAG) des panneaux laminés palplanches est d'une importance capitale. On effectua des tests sur les panneaux connectés pour obtenir les valeurs de rigidité. La valeur EI fut établie à $495 \text{ KNm}^2/\text{m}$, tandis que la valeur de KAG fut établie à 1493 KN/m . La valeur EI n'est pas affectée par les écarts utilisés. Cependant, la valeur KAG a montré une variation appréciable. Les essais à la ont montré que, lorsque la déflexion d'un panneau soumis à un essai de chargement a 4

points atteint $L/46$, la déformation de tension générée à l'intérieur du panneau n'excédait pas de 15% de la deformation a l'ultime du coupon de tension, ce qui démontra qu'une rupture par de tension d'un mur palplanche laminé est peu probable.

Acknowledgements

The author wishes first and foremost to acknowledge Professor Yixin Shao for his invaluable supervision and unquantifiable help throughout the research progress.

The composite seawall specimens were supplied by Pultronex Corporation of Nisku, Alberta. The author extends his gratitude to Mr. Mike Yeats of Pultronex Corporation for his support.

The author is indebted to others as well, Mr. Marek Przykorski for his help in the sensors' connectivity setup, and Mr. Ron Sheppard for assisting in setting up the lab equipment for testing.

To the author's brother and sisters, for their encouragement and continued support. Last but not least to his parents, without which this thesis would never have become a reality, for their support and love.

"The distance is nothing; it is only the first step that is difficult"

Mme. Du Defford, 1697-1780

Table of Contents

Abstract	i
Abrégé	iii
Acknowledgements	v
Table of Contents	vi
List of Symbols	viii
List of Figures	x
List of Tables	xii
Chapter 1 Introduction	
Introduction	1
Chapter 2 Literature Review on Design of Sheet Pile Walls	
2.1 Sheet Pile Walls	8
2.2 Conventional Design Methods	10
2.2.1 Free Earth Support Method	11
2.2.2 Fixed Earth Support Method	13
2.2.3 Computational Pressure Diagram Method (CPD)	15
2.2.4 Finite Element Method	16
2.3 Design Criteria	17
2.4 Flexural and Shear Rigidity of Composite Sheet Piling	19
Chapter 3 Objectives	
3.1 Experimental Investigation	21
3.2 Development of Deflection-Based Design Method	22
Chapter 4 Experimental Investigation of Deformation of Composite Sheet Piles in Flexure	
4.1 Introduction	23
4.2 Experimental Setup and Procedure	24
4.3 Experimental Results	28
4.3.1 Linear Tests	28
4.3.2 Flexural and Shear Rigidity	31
4.3.3 Apparent Flexural Rigidity	33
4.3.4 Sensitivity Analysis	35
4.3.5 Flexural Rigidity from Strain Gauge Reading	38
4.3.6 Failure Test	41
Chapter 5 Development of Deflection Based Design for Composite Sheet Pile Walls	
5.1 Introduction	47
5.2 Traditional Free Earth Support Method	47
5.3 The Simplified Pressure Diagram	53
5.4 Correction of the Linear Pressure Diagram	59
5.5 Deflection Equations	63
5.6 Relationship between M_{\max} and $(Y_b)_{\max}$	73

5.7 Relationship between V_{\max} and $(Y_s)_{\max}$	75
5.8 Rowe's Moment Reduction	79
5.9 Total Deflection of Sheet Pile due to Bending Moment and Shear Force	83
Chapter 6 The Design of Composite Sheet Pile Walls	87
6.1 Introduction	87
6.2 Case Studies	87
6.3 Comparison to fixed Earth Support Method	99
Chapter 7 Discussion and Conclusion	101
References	104
Appendix A	108

List of Symbols

A	Cross sectional area
a	The anchor position from the ground to the water level.
α	Constant, Equation 5.44
α'	Constant, Equation 5.49
β	Moment correction factor
c	Distance from ground surface to the water level
D	Penetration depth
D_d	Design penetration depth
δ_M	Midpoint deflection
δ_Q	Quarter point deflection
E	Modulus of elasticity of composite section
EI	Flexural Rigidity
f_a	Allowable stress
F_y	Yield stress
ϕ	Internal friction angle of sandy soil
I	Second moment of area
G	Shear modulus of composite section
γ	Unit weight or density of soil above water level
γ_{sat}	Unit weight or density of soil below water level
γ'	Effective unit weight of soil
γ_{av}	Average soil unit weight (simplified method)
γ_E	Equivalent soil unit weight
H	Height of sheet pile wall above dredge line
H_w	Height of water
K_a	Lateral active earth pressure coefficient
K_p	Lateral passive earth pressure coefficient
K	Shear coefficient

KAG	Shear Rigidity
L	Total length of sheet pile
M	Moment
M_{max}	Maximum bending moment
$(M_{max})_R$	Reduced maximum bending moment
p_1	Active pressure at depth c
p_2	Active pressure at toe of wall (bilinear pressure diagram)
p_3	Passive pressure at toe of wall (bilinear pressure diagram)
p_4	Active pressure at dredge line
P_{ar}	Anchor force
q_1	Active pressure at wall toe (simplified pressure diagram)
q_1^*	Corrected active pressure at wall toe (simplified pressure diagram)
q_2	Passive pressure at wall toe
R_a	Active resultant force
R_p	Passive resultant force
ρ	Rowe's flexibility number
S	Section modulus
$S.F$	Safety factor
ξ	Shear contribution factor
T	Anchor force
$(V_{max})_R$	Reduced maximum shear force
w	Distributed triangular loading
W_a	Width of computational pressure diagram on active side;
W_p	Width of computational pressure diagram on passive side;
V_{max}	Maximum shear force
$(Y_b)_{max}$	Maximum bending deflection
$(Y_s)_{max}$	Maximum shear deflection
η	H/L, ratio of depth to dredge level to total length of pile
Z	Distance between neutral axis and extreme tension element

List of Figures

Chapter 1

Figure 1.1	Replacement of existing decaying timber pile wall _____	4
Figure 1.2	Insertion of composite sheet piles _____	5
Figure 1.3	Anchor system positioned at the top of the sheet pile wall _____	5
Figure 1.4	Backfill material added behind the sheet pile wall _____	6
Figure 1.5	Final composite sheet pile wall _____	6
Figure 1.6	Fiberglass composite sheet pile section _____	7

Chapter 2

Figure 2.1	Construction Sequence, top: Back filled bulkhead, bottom: Dredged wall _____	9
Figure 2.2	Free earth support method, load and bending moment diagram ____	11
Figure 2.3	Fixed earth support method loading and bending moment diagram	14
Figure 2.4	CPD Loading diagram, simplified active and passive loading ____	15

Chapter 4

Figure 4.1	Experimental setup for four point bending at one third spacing ____	25
Figure 4.2	Roller support in simply supported beam test _____	26
Figure 4.3	Typical setup for linear test at a span of 6.1 m _____	27
Figure 4.4	Typical load-deflection curves from midpoint LVDT1 _____	29
Figure 4.5	Typical load-deflection curves from midpoint LVDT2 _____	29
Figure 4.6	Typical load-deflection curves from quarter point LVDT3 ____	30
Figure 4.7	Typical load-deflection curves from quarter point LVDT4 ____	30
Figure 4.8	Linear plot to determine flexural and shear rigidities _____	32
Figure 4.9	Variation of apparent flexural rigidity with span to depth ratio for two connected panels _____	33
Figure 4.10	EI and KAG versus data points for linear fit _____	37
Figure 4.11	EI and KAG versus data points for linear fit _____	37
Figure 4.12	Pure bending of mid-span in 4 point bending setup _____	39
Figure 4.13	Tensile strain of bottom surface versus load (strain gauge 1) ____	39
Figure 4.14	Tensile strain of bottom surface versus load (strain gauge 2) ____	40
Figure 4.15	Tensile strains versus moment _____	40
Figure 4.16	LVDT and strain gauge setup at midpoint in the failure test ____	41
Figure 4.17	LVDT setup for the failure test _____	42
Figure 4.18	Typical load versus deflection curves of failure test _____	43
Figure 4.19	Twisting of the connected panels about the center _____	44
Figure 4.20	Excessive beam deflection of connected panels in flexion ____	44
Figure 4.21	Load versus tensile strain curves up to a deflection of L/46 ____	46

Figure 4.22	Uni-axial tensile stress strain curves of the flange coupon test	46
-------------	--	----

Chapter 5

Figure 5.1	Load diagram for free earth support method	49
Figure 5.2	Sum of horizontal forces at a depth x	52
Figure 5.3	Simplified load diagram	54
Figure 5.4	Average Soil Unit Weight	55
Figure 5.5	Equivalent force method.	56
Figure 5.6	Active side area loss before correction	60
Figure 5.7	Correction factor β	62
Figure 5.8	Loading diagram broken up	64
Figure 5.9	Three sections in bilinear load diagram	66
Figure 5.10	A blow up of element calculations	67
Figure 5.11	Bending moment distribution due to bilinear load (Case 1.)	68
Figure 5.12	Bending deflection profile due to bilinear pressure diagram	69
Figure 5.13	Bending deflection comparison (Case 1.)	70
Figure 5.14	Shear force distribution due to bilinear load (Case 1.)	71
Figure 5.15	Simple triangular loading	73
Figure 5.16	Relationship between $(Y_b)_{\max}$ and M_{\max}	74
Figure 5.17	Relationship between $(Y_s)_{\max}$ and V_{\max}	78
Figure 5.18	Locations of maximum bending and shear deflection (Case 1.)	78
Figure 5.19	Rowe Reduction Curves	80
Figure 5.20	Maximum moment versus maximum shear for each c/H ratio	82
Figure 5.21	Maximum moment and shear relationship	82
Figure 5.22	Composite and steel sections	84
Figure 5.23	Comparison between a steel section (JSP 3) and a composite section on hand	85

Chapter 6

Figure 6.1	Comparison of deflection based design with strength based design	88
Figure 6.2	Design example (Case 1)	89
Figure 6.3	L/100 design chart for penetration depth	94
Figure 6.4	L/60 design chart for penetration depth	94
Figure 6.5	L/100 design chart for design moment	95
Figure 6.6	L/60 design chart for design moment	95
Figure 6.7	Total maximum deflection versus wall height (L/100)	97
Figure 6.8	Total maximum deflection versus wall height (L/60)	97
Figure 6.9	Anchor force versus wall height (L/100)	98
Figure 6.10	Anchor force versus wall height (L/60)	98

List of Tables

Chapter 2

Table 2.1	Deflection limit for various materials and applications _____	18
Table 2.2	Flexural rigidity (EI) and shear rigidity (KAG) of composite sheet piling [Giroux, 2000] _____	20

Chapter 4

Table 4.1	Linear plot to determine flexural and shear rigidities _____	32
Table 4.2	Sensitivity of flexural and shear rigidity to data points _____	35
Table 4.3	Sensitivity of flexural and shear rigidity to data points _____	36

Chapter 5

Table 5.1	Granular soil properties _____	48
Table 5.2	Comparison of simplified linear load pressure with bilinear load pressure _____	57
Table 5.3	Input parameters of the 16 case studies _____	58
Table 5.4	Comparison of M_{max} and T calculated from bilinear and linear pressure diagrams _____	59
Table 5.5	Correction factor β _____	61
Table 5.6	Result of the 16 cases after correction of linear pressure diagram _____	63
Table 5.7	Deflection position and value comparison _____	70
Table 5.8	$(Y_b)_{max}$ and maximum shear deflection $(Y_s)_{max}$ _____	72
Table 5.9	α' for corresponding c/H ratios _____	76
Table 5.10	Rowe's reduction corresponding to the 16 cases _____	81
Table 5.11	Steel section maximum moment and shear reduction for steel section JSP3 _____	86

Chapter 6

Table 6.1	Design of composite sheet pile wall using a deflection limit of L/100 _____	92
Table 6.2	Design of composite sheet pile wall using a deflection limit Of L/60 _____	93
Table 6.3	Comparison with fixed earth support method _____	100

Chapter 1

Introduction

Connected or semi-connected, sheet piles are often used to build continuous walls for waterfront structures that may range from small pleasure boat launching facilities to large dock facilities. Sheet pile walls are made out of sections driven vertically side by side to form a straight profile, with a plan of dimension sufficiently large that its behavior may be based on a typical unit vertical panel.

Several types of sheet pile are commonly used in construction: (a) wooden sheet piles, (b) precast concrete sheet piles, and (c) steel sheet piles. Wooden sheet piles are used only in light structures that are above the water table. The most common types are ordinary wooden planks and Wakefield piles. The wooden planks are about 50 mm × 300 mm in cross section and are driven edge to edge. Wakefield piles are made by nailing three planks together with the middle plank offset by 50 mm × 75 mm. Planks can also be milled to form tongue and groove piles. Metal splines are driven into the grooves of the adjacent sheeting to hold them together after they are driven into the ground.

Precast concrete sheet piles are heavy and are designed with reinforcements to withstand the permanent stresses to which the structure will be subjected after construction and also to handle the stresses produced during construction. In cross section, these piles are about 500 to 800 mm wide and 150 to 250 mm thick.

Steel sheet piles in the United States and Canada, are about 10-13 mm thick. European sections may be thinner and wider. Sheet pile sections may be Z, deep arch, low arch, or straight web sections. The interlocks of the sheet pile sections are shaped like a thumb and finger or a ball and socket for water tight connections.

Whether the waterfront applications are residential or industrial, the water environment has been proven to be severe on this type of structure. This harshness has been the main factor in the decreased durability of those traditional materials.

Wood represents a versatile material with high strength-to-weight ratio. Products made from wood can be easily handled and installed. But when timber sheet piles are immersed in brackish or saline water, they have to contend with molluscan or crustacean borers. The action of these organisms can be quite destructive. In many instances, these borers have decomposed the wood to the extent that large voids appeared in the material. As a result, the structure can no longer withstand the loading capacity it was designed for and failure is imminent. Damages of this nature can only be remedied by the total replacement of the deteriorated member. Timber piling manufacturers have resorted to chemical treatment, such as treatment with creosote, in an attempt to extend the service life of their products, which is the most popular wood treatment adopted in the industry. This chemical compound represents a growing environmental disposal problem and is listed as a toxin by the Environmental Protection Agency. These chemicals may also pose a health risk to installation workers and a threat to marine life, particularly when used in large quantities.

The concrete piling may not offer the flexibility encountered in the timber product but it does have the advantage of strength and stiffness. Its installation is more costly as concrete has a low strength-to-weight ratio and requires more labor and machinery for installation. In the marine environment, the disintegration of the reinforced concrete does occur and is most severe in the splash zone. The expansive action created by the crystallization of salts and the freezing of water in the pores of the concrete can cause spalling. This spalling will in turn lead to the exposure of steel in case of reinforced concrete. The direct actions of water, oxygen, carbon dioxide and chloride ions will help accelerate the corrosion process. The devastating nature of corrosion will lead to expansive rust being produced, leading to bursting pressure that may cause spalling of the cover in some areas.

The mechanical superiority of steel over the other two materials is well known. Also well documented is the corrosion phenomenon of steel in the water environment. Using weathering or galvanized steel or other special treated steel is expensive. Coating may pose a danger to marine life and the pollution of the water.

Overall, it is estimated that the deterioration of wood, concrete, and steel piling systems costs the U.S. military and civilian marine and waterfront communities \$1 billion annually [Tomlinson 1994]. For economical and environmental reasons there has been a need to find an alternative material to the traditional ones for piling systems.

To improve the durability of sheet piling in water, two polymer-based systems are recently developed and being experimented in the field for their corrosion resistance and lightweight properties. They are the vinyl-based sheet piling system and the fiberglass reinforced polyester sheet piling system. Vinyl sheet piling is manufactured from extruded, UV stabilized Polyvinyl Chloride (PVC) with a minimum nominal wall thickness of 5.7 mm, and moment of inertia of $17.1 \times 10^{-6} \text{ m}^4/\text{m}$. The PVC used for sheet piling has a tensile yielding strength of 44 MPa and a tensile elastic modulus of 2.6 – 3.0 GPa. The fiberglass composite sheet piling is typically fabricated by pultrusion with a wall thickness about 3 mm for web and 5 mm for flange, and a moment of inertia about $17.5 \times 10^{-6} \text{ m}^4/\text{m}$. Although the two sections have moments of inertia at the same order of magnitude, the tensile strength and stiffness of composites are at least four times higher than that of vinyl material. With about 40 – 50% of fibers, the tensile strength of the composites for sheet piling ranges from 187 MPa for web to 430 MPa for flange, and the tensile modulus 12 GPa for web and 30 MPa for flange [Kouadio 2001]. The comparison has shown that the fiberglass composite sheet piling has higher potential to replace the traditional timber and light duty steel sheet piling.

Composite sheet piling products have been currently used to a limited degree, or experimentally for light retaining structures along the waterfront and the coastline.

Because of the composite history lack, the height of composite sheet piling is presently limited to 1.5 - 3 m. Projects were mostly targeted to replace decayed timber walls. Standard procedure of installation is followed without any special equipment. Pictures in Figure 1.1-1.5 demonstrate different stages of installation of a composite sheet pile wall for a replacement project.



Figure 1.1: Replacement of existing decaying timber pile wall



Figure 1.2: Insertion of composite sheet piles, (man height not exceeded)



Figure 1.3: Anchor system positioned at the top of the sheet pile wall



Figure 1.4: Backfill material added behind the sheet pile wall.

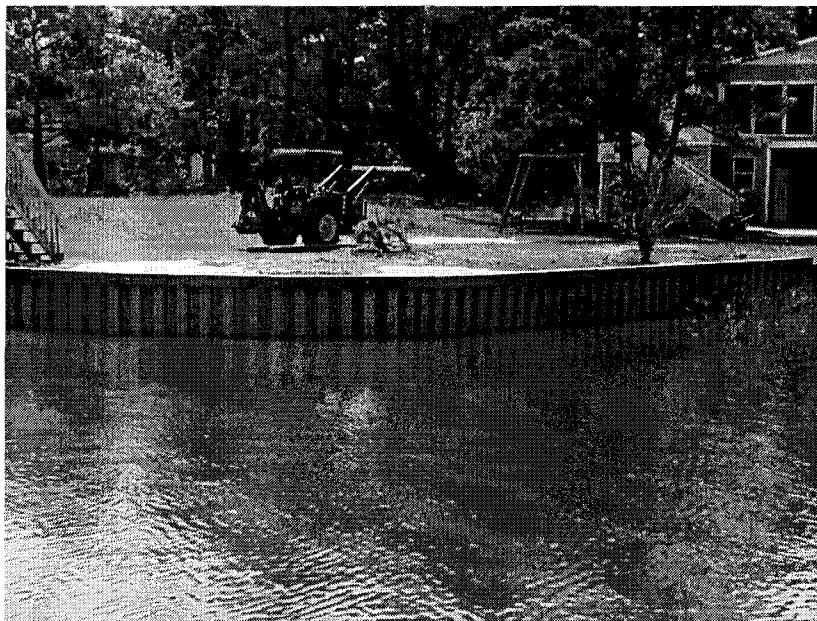


Figure 1.5: Final composite sheet pile wall.

To promote more applications of corrosion resistant and light weight composite sheet piling system, several disadvantages of the material should be overcome. Currently, composite materials depending on location, cost approximately two to three times the cost of creosote-treated timber piles. Second, the long term performance of composite under increasingly larger structural load is not well defined. Third, because of their low modulus compared to steel, composite-piling materials may exhibit large deformations in excess of design limits.

Higher initial cost is offset by the fact that composite piling costs less to maintain, lasts twice as long as treated timber piling and doesn't present an environmental disposal problem. Kouadio (2001) recently studied the long-term performance of composite sheet piling in water. The results indicated that tensile strength of fiberglass reinforced polymer composite in water was decreased with the increase of water absorption and stabilized at the state of saturation. However, there was no noticeable change in tensile modulus during hot water aging period. The saturated composites showed excellent resistance to freeze-thaw cycling from 4.4°C to -17.8°C. To control large deformation in composite structure due to low modulus; the optimum way is to develop a deformation based design approach to allow the use of deformation limit set by the design engineer. The purpose of this research is to explore the possibility of developing a deflection based design approach of fiber glass composite sheet pile wall to tackle the large deformation problem in the composite sheet pile wall structure. A fiberglass composite sheet section is shown below in Figure 1.6.

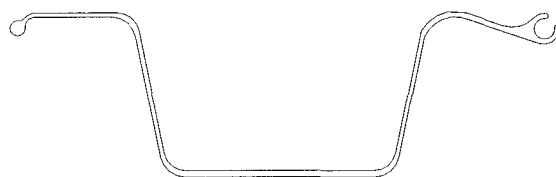


Figure 1.6: Fiberglass composite sheet pile section

Chapter 2.

Literature Review on Design of Sheet Pile Walls

2.1 Sheet Pile Walls

Anchored sheet piles can be classified according to (1) the material used, (2) type of anchorage, (3) construction sequence.

Material used: As discussed in Chapter 1., timber, steel and reinforced concrete are common materials used in manufacturing the sheet piles, only recently, vinyl and composites have entered the market. Steel sheet piles are the most commonly used in waterfront conditions. This is because in most instances steel piles are (1) most economical, (2) have a variety of cross sections, (3) stiff enough to be driven without buckling or springing, and (4) available in different combinations to allow for an increase in the section modulus.

Type of Anchorage: (1) Single dead-man; consists of a tie rod attached to anchor that is placed far enough back from the wall to ensure that its passive resistance zone in the backfill does not encroach on the active soil wedge behind the wall. (2) Double or more tie rod anchorage; these are usually used when a single anchor is inadequate to provide acceptable stresses in the sheet pile wall. The disadvantage of this anchorage is, because of the independent yield of both tie rods, the performance of the sheet pile is rather uncertain. (3) A frame type of pile anchorage; this is recommended for soft compressible soil which cannot be conveniently removed by dredging. A frame anchor usually has a larger load carrying capacity than other types of anchors. (4) Anchor piles; the basic advantage of this type of anchorage is its simplicity for construction.

Construction Sequence: the construction sequence has a great impact on the sheet pile design. There are two main ways in which a sheet pile might be constructed (Figure 2.1):

- 1) Backfill construction: dredge, drive, construct anchor system, backfill.

- 2) Dredging construction: drive, construct anchor system, backfill (when needed), dredge front of pile.

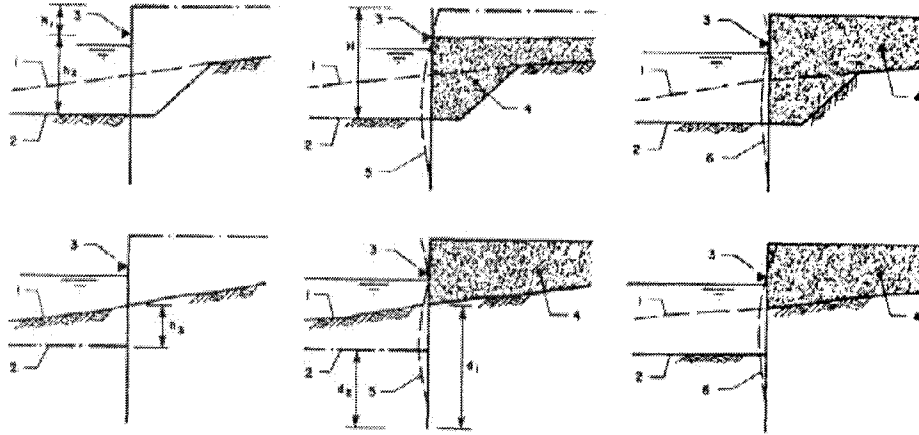


Figure 2.1: Construction Sequence, top: Back filled wall, bottom: Dredged wall.
[Tsinker 1997]

The traditional failure of a sheet pile wall can be classified into four modes, [Bowles, 1998]:

1. Sheet pile flexural failure by bending. To prevent the flexural failure, the strength based design is adopted. For steel sheet pile wall with design moment M from analysis and a properly selected section modulus S , is given as follows:

$$f = \frac{M}{S} \leq f_a \quad 2.1$$

For steel use of allowable stress of $f_a = 0.65 F_y$ gives an apparent Safety factor (SF) of 1.53 which will be amply adequate in most situations.

2. Anchor rod failure. This may be by pulling the anchor rod into, or either an anchorage failure at the wall or at the anchor. For the anchor rod one should limit

$$f = \frac{P_{ar}}{A} \leq 0.6 \text{ or } 0.7 F_y \quad 2.2$$

A SF of about 1.5 to 2 should be used for attaching the anchor rod to the wall and similarly for the anchorage.

3. A toe (or kick out) failure. This may occur if the embedment depth is not adequate. This mode is prevented by increasing the required penetration depth D by some amount perhaps 20 to 40 percent using either the Finite Element Method (FEM) or classical methods.
4. A system failure. This is a potential rotational failure of an entire soil mass containing an anchored wall. This potential failure is independent of the structural characteristics of the wall and /or anchor. The adequacy of the system against this mode of failure should be assessed by the geotechnical engineer through conventional analysis for slope stability. This mode of failure cannot be remedied by increasing the depth of penetration nor by repositioning the anchor. The only recourse when this type of failure is anticipated is to change the geometry of retained material or improve the soil strengths.

2.2 Conventional Design Methods

The design of sheet piles (flexible retaining structures) is somewhat more complicated compared to regular retaining walls. The soil pressure is the main force acting against the sheet pile wall. The magnitude of this pressure depends upon the physical properties of the soil and the character of the interaction of the soil/structure system. Two basic anchored sheet pile wall design procedures are commonly used, they are (1) the free earth support method, and (2) the fixed earth support method. In addition, the Simplified Computational pressure Diagram (CPD) method and the finite element method are also developed for the analysis. These methods, are independent of the sheet pile material, they are based on soil stability, and thus can be applied to composite sheet piling.

2.2.1 Free Earth Support Method

The free earth support method is the oldest and most conservative design procedure. The soil below the dredge line is assumed to have reached its limiting shear strength throughout the depth of the wall embedment. The wall is considered stiff and unyielding relative to the soil; failure is assumed to occur by rotation about the anchor location. The required depth of embedment is found by setting the sum of moments due to pressures on each side of the wall equal to zero. Since the full shear resistance of the soil in front of the wall is unlikely to be mobilized without unacceptable deflections and settlements, factors of safety are applied to the depth of embedment and the anchor force. After the required depth and anchor force are found, the shear and bending moment in the wall can be found as functions of depth. Wall deflection can be found by making an assumption about point of wall fixicity or deflection at a given point or by using calculated soil pressures in a finite element model of the system. The free earth support method is still in use in the United States, Brazil, and the United Kingdom. Figure 2.2 shows a typical pressure diagram and bending moment diagram for a free earth support design.

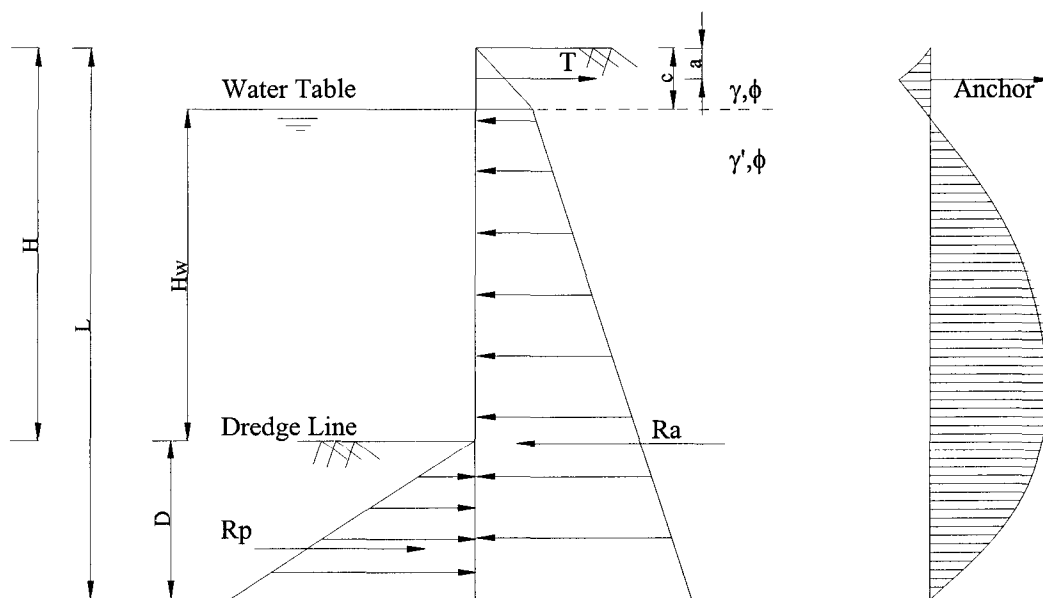


Figure 2.2: Free earth support method, load and bending moment diagram

Observations have shown that due to sheet pile flexibility, the actual maximum moment on the sheet pile wall is less than that calculated theoretically by the free earth support method of design. Hence, for the determination of the actual design moment, M_{\max} should be reduced somewhat. Based on model experiments, Rowe (1952), proposed a semi-empirical procedure for moment reduction which was referred to as Rowe's moment reduction procedure.

Using wall models of height (500-900 mm), Rowe established a relationship between the flexibility number, ρ , and the reduction of the maximum bending moment as compared to conventional methods employing active pressure as a basic load distribution. The flexibility number, ρ , is given in Equation 2.3:

$$\rho = \frac{L^4}{EI} \quad 2.3$$

Where L is the total wall height (i.e. height above dredge line plus penetration depth), E and I are the modulus of elasticity and the moment of inertia, respectively, per unit length of wall, of the pile section.

Lasebnik (1969) used wall models 1650 mm high, the total number of tests was about 500, models of sheets with different flexibility and sand of different densities were examined as foundation and backfill material. Unlike other investigations, Lasebnik's setup was more representative. He used individual sheet piles interlocked to form a wall for the model, this allowed the sheet piles to rotate in their clutches, thus reducing the interference of transverse forces in obtaining more realistic data on wall performance. The flexibility factor, ρ , used by Lasebnik was the same as that established by Rowe.

Lasebnik's principle conclusions were as follows:

- (1) The reduction in bending moments is especially drastic in the range of $\rho = 0.2$ - 0.6 , and a further increase of bulkhead flexibility has no significant effect on reduction of bending moments.
- (2) The total active pressure against a flexible wall is 25-30% smaller than that acting on a rigid wall.
- (3) The non-triangular shape of the passive pressure diagram contributes to a reduction of the effective span of the bulkhead and, thus, in reducing the bending moments and reaction forces.

2.2.2 Fixed Earth Support Method

The fixed earth support method was derived from the work of Blum (1955) and is mostly used in Europe. The sheet piling is considered flexible but driven to a sufficient depth that it may be considered fixed at its toe. Following the work of Rowe (1952) and Terzaghi (1954), most geotechnical engineers in the UK now use a form of the free earth support method modified to take account of the wall flexibility. This has occurred because repeated studies have shown that the fixed earth support method requires excessive depths of penetration.

The pressure and moment diagram used in the fixed earth support method is shown in Figure 2.3. Point C, is a point of contraflexure, at this point the pile is assumed to act as a hinge (zero bending moment). Hence, the portion of the piling above point C can be treated as a beam that resists the net earth pressures via the force T and the shear R_c , as indicated in the figure.

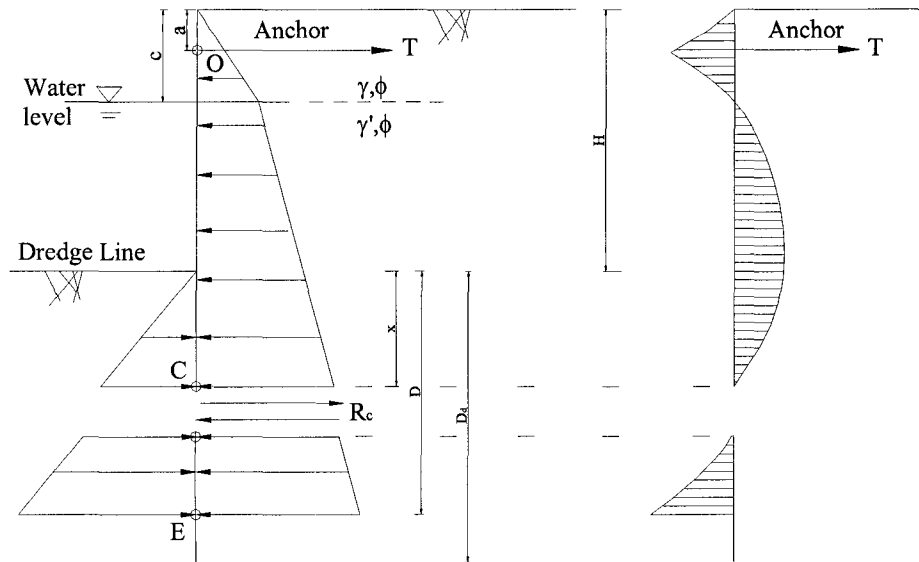


Figure 2.3: Fixed earth support method loading and bending moment diagram

Blum established a theoretical relationship between the angle of internal friction and the distance from the point of contraflexure to the dredge line, x .

For a given angle of internal friction ϕ the value for x can be calculated as a function of H . Hence, by summing the moments about O (anchor level), the shear R_c is determined. With R_c known, the summation of moments about point E yields a relationship where the only unknown is D . Given the penetration depth, D , one may proceed to determine the maximum moment.

2.2.3 Computational Pressure Diagram Method (CPD)

This is a simplified version of the free earth support method, proposed by Nataraj and Hoadley (1984). The procedure developed was based upon the experimental observations of Tschebotarioff (1949), and Rowe (1952). According to the CPD method, the net pressure diagram above and below the dredge line is replaced by rectangular pressure diagrams. This is shown in Figure 2.4 below, in which W_a is the intensity of the active pressure diagram above the dredge line, and W_p is the intensity of the net passive pressure diagram below the dredge line.

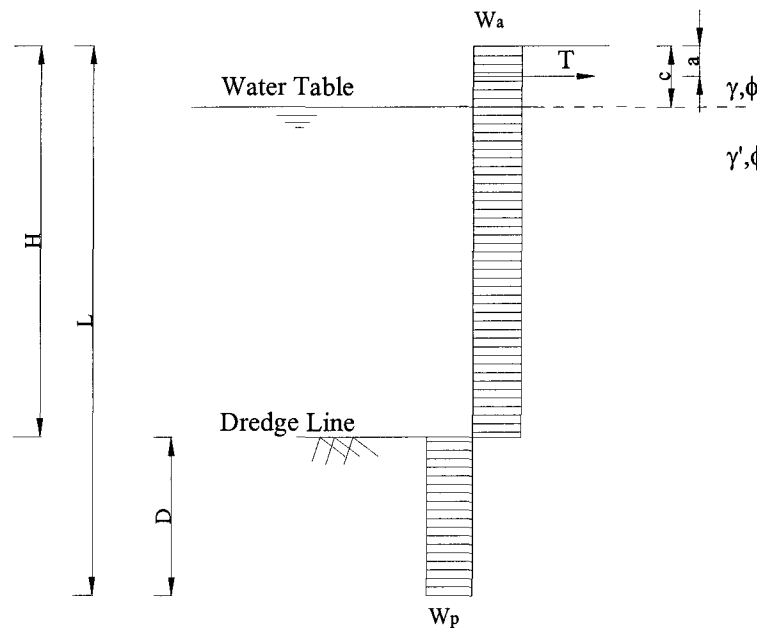


Figure 2.4: CPD Loading diagram, simplified active and passive loading.

The CPD procedure produced maximum moments 60-70% of those computed by the free earth support method; however, the anchor forces computed by CPD were larger, ranging from 1.2-1.6 times those calculated by the free earth support method. The depth of penetration computed by the CPD method is 1.25-1.5 times that calculated by the free earth support method. This is in agreement with the tradition of increasing the embedment depth determined by the free earth support method by about 20-40% to

satisfy safety requirements. The method yields a safe penetration depth, a reduced maximum moment, and a larger anchor force. The design procedure may not be a substitute for more comprehensive analysis, but it will help in many preliminary design phases.

2.2.4 Finite Element Method

The finite element method (FEM) is considered an efficient and rational method for design of sheet pile walls. It directly gives the lateral displacement profile (valid for that set of soil parameters and pile stiffness) as well as nodal pressures in the passive zone in front of the wall, bending moments at nodes and force(s) in the anchor rod(s). Multiple anchor levels can be as readily accommodated as a single anchor; and parametric studies for optimum anchor location can be made easily. The FEM analysis finds the center of pressure to sustain the wall in a soil pile interaction mode rather than making arbitrary assumptions about passive pressure as in the classical methods. Some restrictions apply though, like any FEM problem, the profile has to be broken down into elements connected by nodes, several trials have to be attempted in order to find the most efficient element length. In addition, the method is still carried out by trial and error; increasing the depth by a specific increment until an optimal solution is reached. Several software have been developed to assist in the solving of geotechnical design problems, for example Z-Soil and PLAXIS. Given that a computer is available, having enough FEM background, the method has some drawbacks.

2.3 Design Criterion

In the past, the Allowable Stress Design (ASD) procedure has provided a simple and convenient approach to the design of many structural applications. ASD utilizes a single factor of safety to account for the variability of both load effects and material properties, as well as long term performance.

Thus, the strength of the material is reduced to an allowable stress to compensate for the potential of an increase in load above the design value. On the other hand, the Load Resistance Factor Design (LRFD), was developed as a refined design procedure that would better estimate the effects of loads applied to a structure and the strength offered by the structure [Chambers 1997].

In addition to the strength and safety issues addressed by the design for strength limit states, the design rules need to address limit states that affect the serviceability or functionality of the structure. Serviceability limit states are those states in which the behavior of the structure under normal operating conditions is unsatisfactory, and these included excessive deflection, excessive vibration, and excessive permanent deformation. Deflection is the major serviceability limit state that would be applicable with regards to the sheet pile wall. In order to control the deflection, a deflection limit is set to define the maximum allowable deflection which is represented as a fraction of the span. For example, a beam with a span of 1000 mm and a limit of $L/60$, the beam can deflect to a maximum of 16.67 mm.

Setting a deflection limit is not a simple task, often limits are set arbitrarily by either eye inspection (shelf sag, $L/240$) or by comfort performance (bridge deflection limit varies from $L/360$ - $L/500$). Having no test standard to be performed or unified deflection standard makes selecting a deflection limit a hard job. Table 2.1 lists several deflection limits for different applications and materials. The highest limit is associated with the brick veneer application, $L/360$. Deflection calculations for masonry walls are approximate, this is due to the uncertainty of the modulus of

elasticity of the material and to the distribution and depth of the cracks throughout the section. Other reasons for this high limit are: design for air barrier, tensile strength of the masonry, and limit of crack widths to about 0.5 mm to 1.0 mm which by geometry entails a deflection limit of L/360.

Table 2.1: Deflection limit for various materials and applications.

Application	Limit (L/x)	Source (Dates checked)
Brick veneer (masonry walls)	L/360	http://www.masonryinstitute.com (22-5-01)
Aluminum Secondary members of structures	L/200-250	http://www.alu-info.dk/Html (22-5-01)
Plywood and Oriented Strand Board	L/240	http://www.cofra.com (20-5-01)
Beams (laterally unsupported)	L/100-240	http://www.strongwell.com (20-5-01)
Particleboard and MDF for shelving	L/240	www.pbmdf.com (20-5-01)
Aluminum cladding (walls and roofs)	L/90-100	http://www.alu-info.dk/Html (22-5-01)
Plates	L/100	http://www.strongwell.com (20-5-01)
Siding (COMPOSOLITE)	L/60-180	http://www.strongwell.com (20-5-01)
Aluminum association (diaphragms and roofs)	L/60	http://aec.org/extrusion_apps.html (22-5-01)

Aluminum has a relatively small value of young's modulus of elasticity together with high value of strength. The deformation of aluminum alloy structure is for this reason of a critical requirement. Since its deformation is significant, when used in visible applications, or when its performance will effect surrounding components, higher deflection limits are required, L/360. However, when their use is associated with less visible and shorter free spans such as cladding or roofing, their deflection limits are less conservative, L/90 - L/100.

Similarly, composites can have significant deflection in the waterfront application owing to the low modulus and the thin-walled structure. The current wall heights serving as spans are about 1.5 to 3.5 m which are relatively short. It is usually anchored at top surface. The deflection will not be visible compared to a wooden shelf (L/240). In addition, there are no secondary members, or surrounding components that are attached. The sheet pile wall can be looked at more of a siding (L/60). Therefore, the deflection-based design of composite sheet pile wall studied in this project will employ two deflection limits, the conservative L/100 limit, and less conservative L/60 limit.

2.4 Flexural and Shear Rigidity of Composite Sheet Piling

To implement the deflection based design of composite sheet pile wall, it is essential to properly characterize the flexural rigidity (EI) and shear rigidity (KAG) of the composite sheet pile section. Presently, there is no standard test method to obtain the flexural and shear rigidity of composite sheet piling. ASTM D790 suggested a span to depth ratio of 16:1 or larger to minimize the effect of shear force on the elastic modulus of composite laminated beam. In the Construction Productivity Advancement Research (CPAR) program, a span of 2.7 m was employed to test and compare the flexural rigidity of different sheet pile products [Lampo, et al, 1998]. Method to simultaneously determine the elastic modulus and shear modulus of a laminated composite beam was proposed by Fischer et al (1981) using a single beam specimen in three-point bending tested at two span-to-depth ratios. An experimental procedure based on Timoshenko's beam theory was developed by Bank (1989) in order to simultaneously determine both section flexural modulus and section shear modulus of pultruded composite I-beams and wide-flange beams. The Bank's method was later employed on I-sections and H-sections in a composite beam buckling analysis [Brooks 1995]. Efforts were also made to directly determine the flexural and shear rigidities of a pultruded I-beam using combined tensile strain and deflection measurements [Najaraj and GangaRao 1997].

An extensive study was carried out recently to determine the flexural and shear rigidity of the composite sheet pile panels [Giroux 2000]. Three and four point bending tests were conducted with varying spans. Using Timoshenko's beam theory and Bank's modified procedure, EI and KAG were calculated. For each test, the result for both the EI and the KAG from the mid point and quarter point were compared. Table 2.2 summarizes the results. The flexural rigidity results from the four independent tests agreed well with each other. The shear rigidity agreed well when based on the midpoint deflection results, however, there was a rather large difference when based on quarter-point deflection results. This was possibly due to the limited

amount of data for the quarter-point deflections and because of the sensitivity of the method to the data points in the determination of the shear rigidity.

Table 2.2: Flexural rigidity (EI) and shear rigidity (KAG) of composite sheet piling [Giroux, 2000]

	Midpoint Deflection	Quarter point Deflection	<i>Difference</i> (%)
3-Point bending EI (Nm ²)	212035	216017	1.8%
4-Point bending EI (Nm ²)	200597	200196	0.2%
<i>Difference (%)</i>	5.4%	7.3%	
3-Point bending KAG (N)	755869	529378	30%
4-Point bending KAG (N)	872081	996919	12.5%
<i>Difference (%)</i>	13.3%	46.9%	

Chapter 3.

Objectives

In order to efficiently design and use pultruded Glass Fiber Reinforced Polymer (GFRP) sections in the anchored sheet pile wall applications, the objectives of this research are: (1) to experimentally determine the flexural and shear rigidities of the GFRP sheet pile panels using four point bending test setup; (2) to demonstrate the necessity of having a deflection based design for composite sheet pile wall; 3) to derive the deflection equations for the convenient use in design procedure. 16 case studies with wall height ranging from 1.5 m to 4.5 m will be investigate alongside the equation derivation for verification.

3.1 Experimental Investigation

Giroux (2000), used three and four point bending tests to find the flexural and shear rigidities. Since the latter gave better results, a modified four point bending setup will be used to determine sheet pile rigidity with flexible steel strapping to provide lateral restraint and eliminate local crushing.

Timoshenko's beam theory will be used to define the flexural rigidity EI , and the shear rigidity KAG , for the sheet pile panels. Timoshenko's equation is to be rearranged to allow a linear plot with $1/EI$ being proportional to the curve slope, and $1/KAG$ to the y-axis intercept. Eleven different spans are to be tested, ranging from 6.7 m to 1.5 m. The consistency of the results are to be discussed.

A failure test will be performed under the four point bending testing setup. For comparison reasons with Giroux (2000), 4.6 m panel span is to be tested. This will enable the investigation of the failure mechanism, and the observation of the deflection extent.

3.2 Development of Deflection-Based Design Method

The current bilinear loading, whether originating from free or fixed earth support methods is rather complex when deflection is concerned. Thus a simplified model will be proposed. Verification of the simplified model will be carried out to prove its applicability. Free earth support method together with Rowe's moment reduction will be employed as start point of design for deflection.

Accordingly, equations of bending deflection and shear deflection will be derived based on simplified linear earth pressure. The relationship between maximum bending moment and maximum bending deflection, and relationship between maximum shear force and maximum shear deflection will be established to serve as basic equations in deflection-based design. 16 cases of wall design with different wall heights and water levels will be implemented using both deflection limits of $L/100$ and $L/60$. If the deflection criterion is not satisfied, method of increasing the penetration depth of the wall will be used to decrease the deflection and reduce the maximum bending moment.

Chapter 4

Experimental Investigation of Deformation of Composite Sheet Piles in Flexure

4.1 Introduction

The purpose of the experimental investigation is two folds, first to experimentally determine the flexural and shear rigidity through a four point bending test setup, and secondly, to study the failure mechanism of sheet pile tested at 4.6 m (15 Ft) span.

A modified Bank's (1989) approach was used to simultaneously determine the flexural and shear rigidities of the composite sections. Two sections side by side were linked together through the pin-eye connection, and the deflection values were measured from the span's midpoint and quarter points of both sections. The comparison of the rigidities calculated from both midpoint and quarter point deflections would allow the verification of the approach. Strain gauges were also used at midpoint along tension side of both sections to monitor the tensile strain.

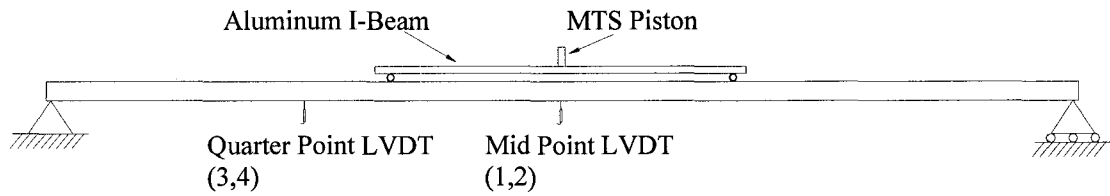
Failure test was performed on a 4.6 m (15Ft) span using strain gauges and LVDTs to examine the failure mode.

4.2 Experimental Setup and Procedure

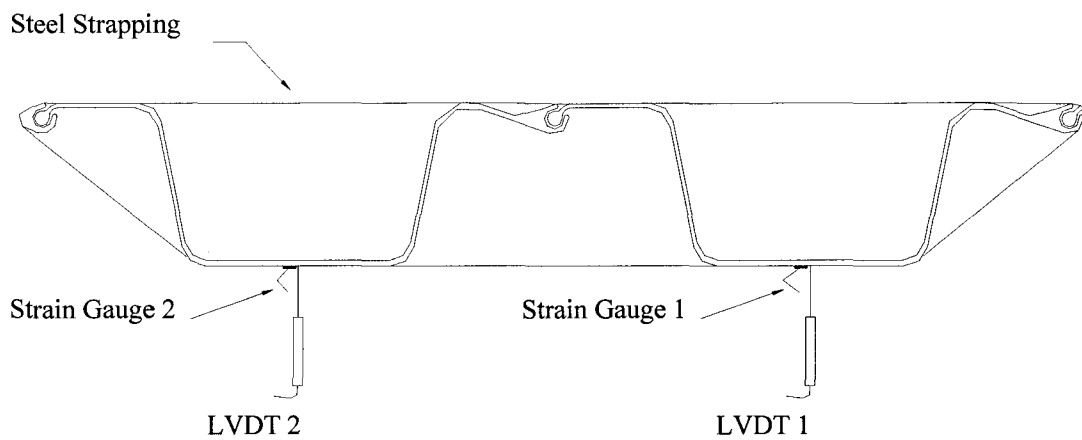
To determine the rigidities of the connected sheet piles, tests were performed using the four point bending setup at equal space with eleven spans; 1.5, 1.8, 2.1, 2.4, 3.1, 3.7, 4.3, 4.9, 5.5, 6.1, and 6.7 meters (5, 6, 7, 8, 10, 12, 14, 16, 18, 20, and 21.8 Ft), within the linear proportional limit. Each span test was repeated a minimum of three times. Following the linear tests, a failure test was performed on the 4.6 m (15 Ft) span.

The tests were carried out at the McGill University's Civil Engineering laboratory. The connected sheet pile panels were loaded using an MTS testing machine with a capacity of 1000 KN (220 Kips) and a stroke range of 30 cm. The load was measured using an external load cell with a capacity of 2.2 KN (5000 lb). Another load cell with a higher capacity of 45 KN (100 Kips) was used for the failure test. The loading rate was uniform for all the tests, with an average of 0.03mm/s.

An elevation view of the experimental setup for the four point bending tests is shown in Figure 4.1a below. A pin and an eye were inserted in both ends of the panels to complete the cross section as shown. Steel straps of size 2.5 cm (1 inch) wide were used to tie around the cross section, in order to confine the panels and to limit the lateral displacement. Giroux (2000) used 2.5 cm × 2.5 cm stiff steel frames at load points as a restrain mechanism. The use of flexible steel strapping at a uniform spacing of 61 cm (2 feet) was to provide a uniform restrain and prevent the panels from local crushing and buckling in failure tests.



a)



b)

Figure 4.1: Experimental setup for four point bending at one third spacing. a) side view of experimental setup. b) Cross section view of experimental setup.

To measure deflection, four linear variable differential traducers (LVDTs) were used. Two were positioned at the spans' midpoints, one for each section to monitor the deflections and the possible twisting. The other two were positioned at the spans' quarter points, again one LVDT for each section to obtain independent load-deflection curves to compare the experimentally determined rigidities from different locations.

To measure the tensile strain, two strain gauges were mounted on the bottom surfaces (main flange) of the panels at the span's midpoint, one for each section. The strain gauges used had a gauge length of 5 mm, gauge factor of $2.13 \pm 1\%$ and a resistance of $120 \pm 0.3 \Omega$.

The data were recorded using a Measurement Group System 5000 data acquisition system and the Strain Smart software V2.2. Data points were recorded at a rate of one scan per second. Each scan recorded the load, the four LVDT displacements and the two strain gages' readings simultaneously.

An apparatus for supporting the beams was designed and constructed such that both ends were free to rotate and one of the two was free to translate in the horizontal axis to simulate a simply supported condition. Figure 4.2 shows the roller support on the right hand side of a beam. The roller mechanism involved a hollow steel cylinder which was free to roll in the horizontal axis. Four sheet pile sections of different length were used for tests at different spans, they were 1.8, 2.4, 3.4, and 6.7m (6, 8, 11, and 22 Ft) long for each. The length of panel was selected to minimize the overhanging, thus to eliminate any resulting negative moments.

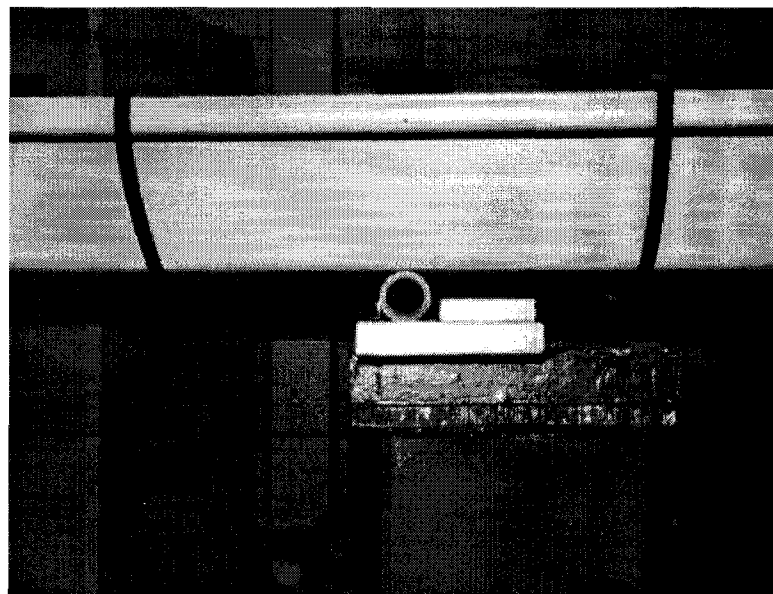


Figure 4.2: Roller support in simply supported beam test

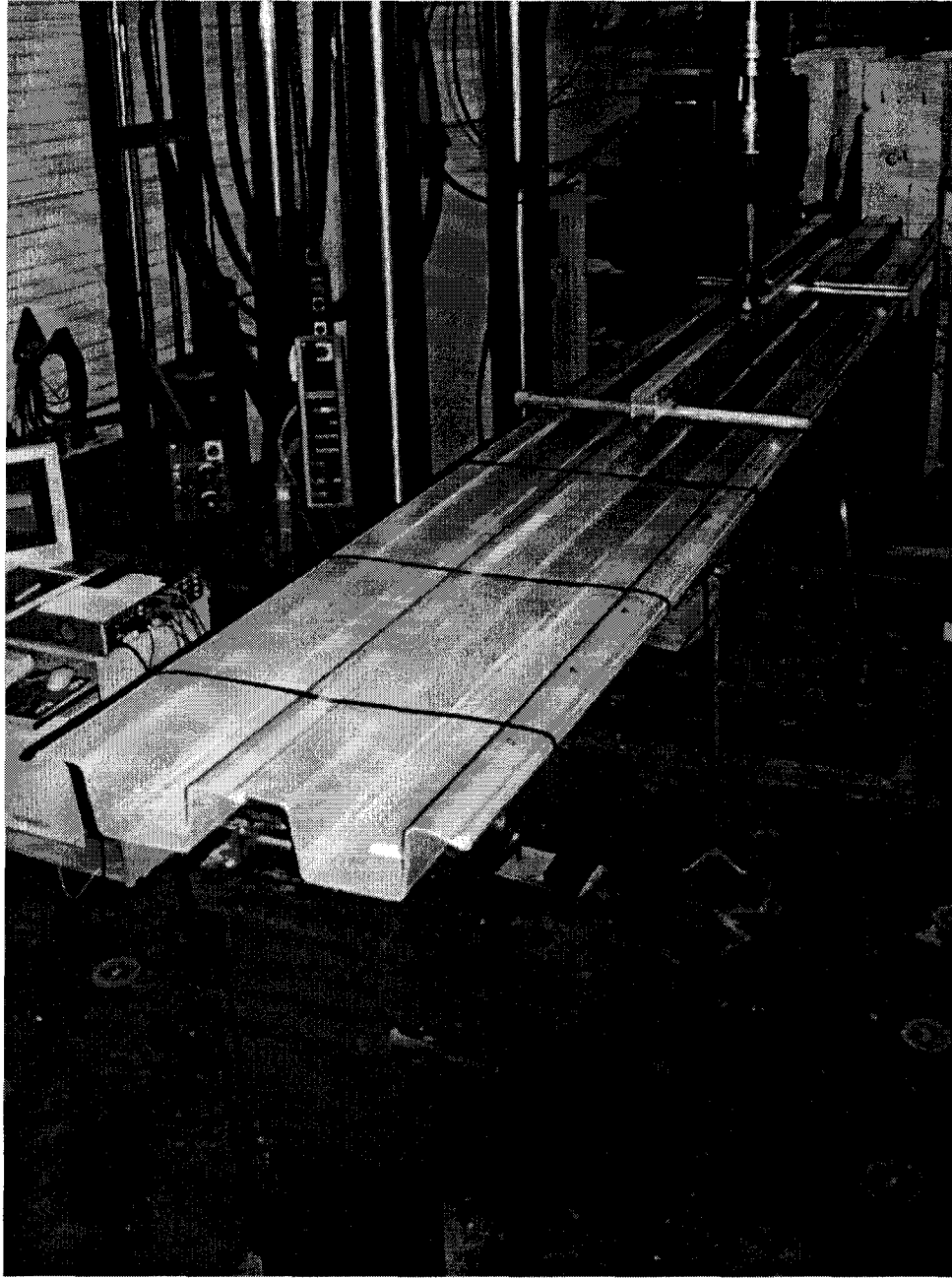


Figure 4.3: Typical setup for linear test at a span of 6.1m (20Ft)

The four point bending tests consisted of supporting the beam on both ends while applying loads at one third span by using an aluminum I beam to bridge the two loading points as shown in Figure 4.3.

4.3 Experimental Results

4.3.1 Linear Tests

The linear tests consisted of four point bending tests within the linear proportional limit. Four sheet pile panels with different length were used for varied span tests. The panel of 2.1 m (7 feet) was used for the 1.5 and 1.8 m (5 and 6 feet) tests, the second panel of 2.4 m (8 feet) was used for the 2.1m (7 feet) test, the third specimen of 3.4 m (11 feet) was used for the 2.4 and 3 m (8 and 10 feet) tests, a fourth specimen with a length of 6.7 m (22 feet) was used to test 3.7, 4.3, 4.9, 5.5, 6.1 and 6.7 m (12, 13, 16, 18, 20, 21.8 feet). Typical curves for the load versus deflection at different spans are given in Figure 4.4-4.7. Figure 4.4 and 4.5 were obtained from midpoint deflection and Figures 4.6 and 4.7 were from quarter point deflection. As expected the slope of the load versus deflection curve decreases with increasing span length, indicating that flexibility depends on the span. It agrees with Rowe's flexibility model discussed in chapter 2.

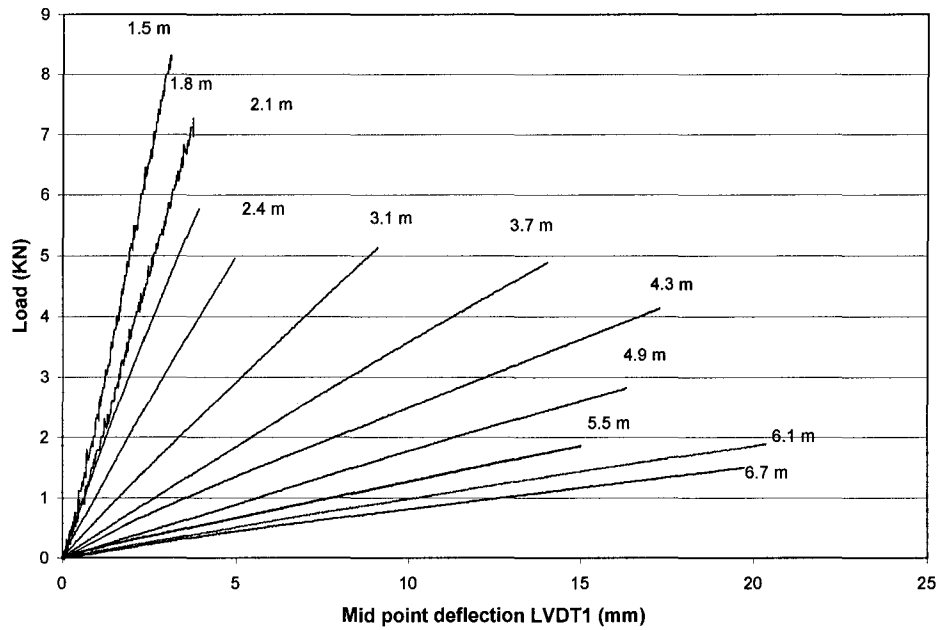


Figure 4.4: Typical load-deflection curves from midpoint (LVDT1)

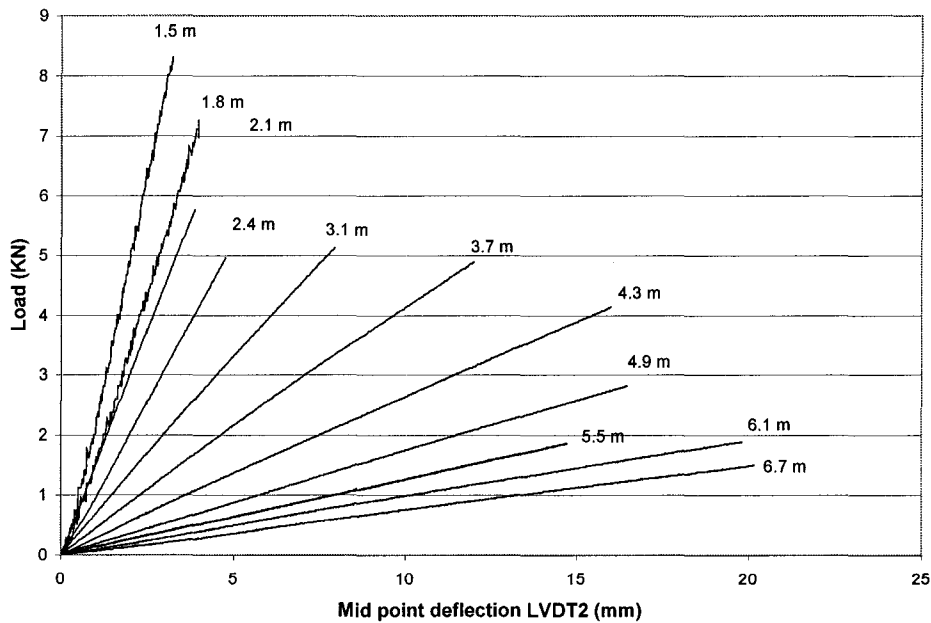


Figure 4.5: Typical load-deflection curves from midpoint (LVDT2)

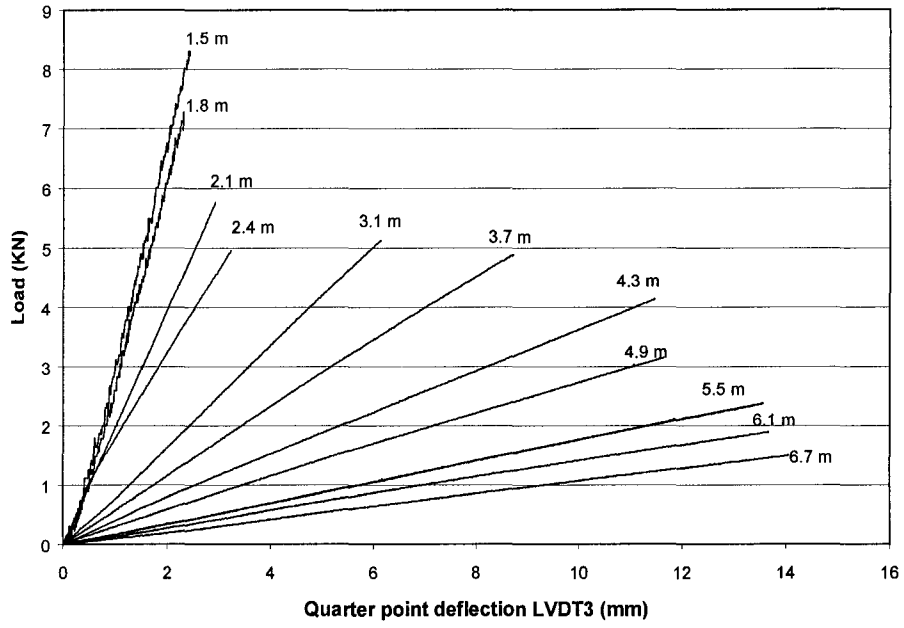


Figure 4.6: Typical load-deflection curves from quarter point (LVDT3)

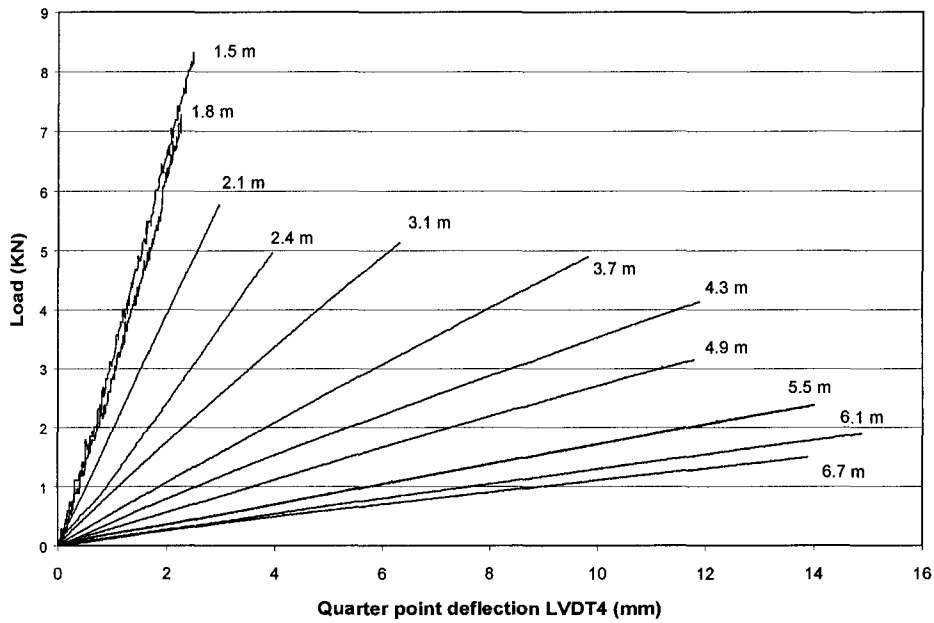


Figure 4.7: Typical load-deflection curves from quarter point (LVDT4)

4.3.2 Flexural and Shear Rigidity

Flexural rigidity is defined as the product of the section flexural modulus, E , and the second moment of area, I . Similarly, the shear rigidity is defined as the product of the factored area, KA , and the section shear modulus, G . The factor K , is the shear coefficient for composite beams in flexure. Timoshenko's equation is employed to relate the deflection to the load due to both bending and shear contributions. The Timoshenko's equation for the midpoint deflection in a four point bending setup with equal spacing is given by:

$$\delta_M = \frac{23}{1296} \frac{PL^3}{EI} + \frac{PL}{6KAG} \quad 4.1$$

At quarter point in the same setup, the deflection is given by:

$$\delta_Q = \frac{29}{2304} \frac{PL^3}{EI} + \frac{PL}{8KAG} \quad 4.2$$

Where δ is the deflection, P , the applied load, and L the span length,

Rearranging Equations 4.1 and 4.2 gives:

At midpoint equation:

$$\frac{\delta_M}{PL} = \frac{23}{1296} \frac{L^2}{EI} + \frac{1}{6KAG} \quad 4.3$$

At quarter point equation:

$$\frac{\delta_Q}{PL} = \frac{29}{2304} \frac{L^2}{EI} + \frac{1}{8KAG} \quad 4.4$$

Linear fits using the method of least squares were performed on the loading deflection curves in Figures 4.4-4.7. This provided values for the slope, P/δ (load/deflection), for each span L , which allowed $\delta/(PL)$ and L^2 to be plotted as straight line based on Equations 4.3 and 4.4. For each span, at least three independent tests were performed and thus three sets of data are available on the $\delta/(PL)$ versus L^2 plots, each set is an

average of the two cross sectional LVDTs. As seen in Figure 4.8, good repetition was achieved.

Linear fits were used to determine the equations of the two lines. The slopes and intercepts of these lines were used to determine the flexural and shear rigidity in each case. The values obtained from the quarter and midpoint positions are summarized in Table 4.1, which agree well. This self check is strongly supportive of the proposed experimental method. In Table 4.1, two sets of data are listed. One is the rigidities for two connected sheet pile panels and the other is the rigidity per width (per meter) of the panel. The latter is more commonly used in engineering design.

Table 4.1: Flexural modulus and shear rigidities comparison for connected panels.

	Midpoint Deflection	Quarter Point deflection	Difference %	Average EI or KAG
For Two Connect Panels				
EI (Nm ²)	401060.2	410528.6	2.3	405794
KAG (N)	1233654.1	1214771.6	1.5	1224213
Rigidity per meter				
EI (Nm ² /m)	489097.8	500644.6		494871
KAG (N/m)	1504456.2	1481428.8		1492943

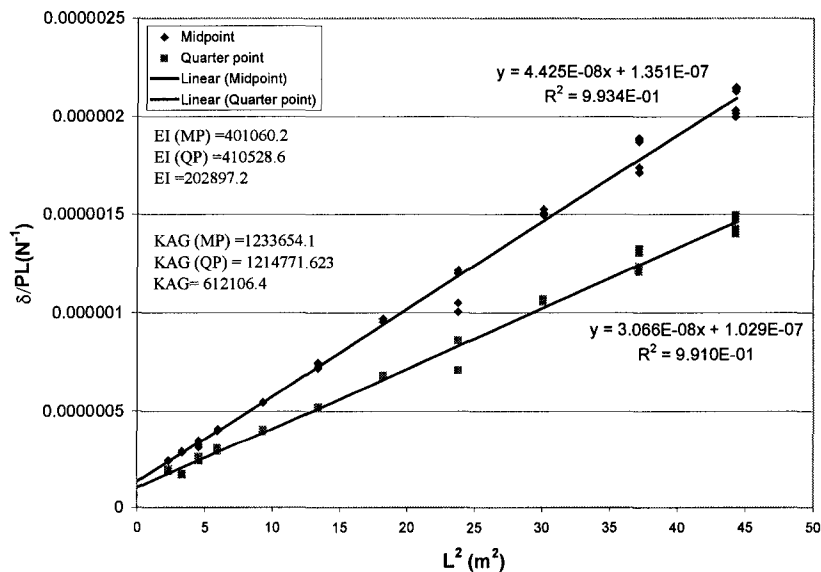


Figure 4.8: Linear plot to determine flexural and shear rigidities

4.3.3 Apparent Flexural Rigidity

The apparent flexural rigidity, EI , is defined as the resistance of a beam to deflect due to only bending, neglecting shear deflections. The slopes of the load-deflection curves in Figure 4.4 to 4.7 were used to determine the apparent flexural rigidity based on the first term of Timoshenko's equation. As expected, the apparent flexural rigidity varied with the span to depth ratio, indicating that indeed shear does have significant effect on flexural rigidity.

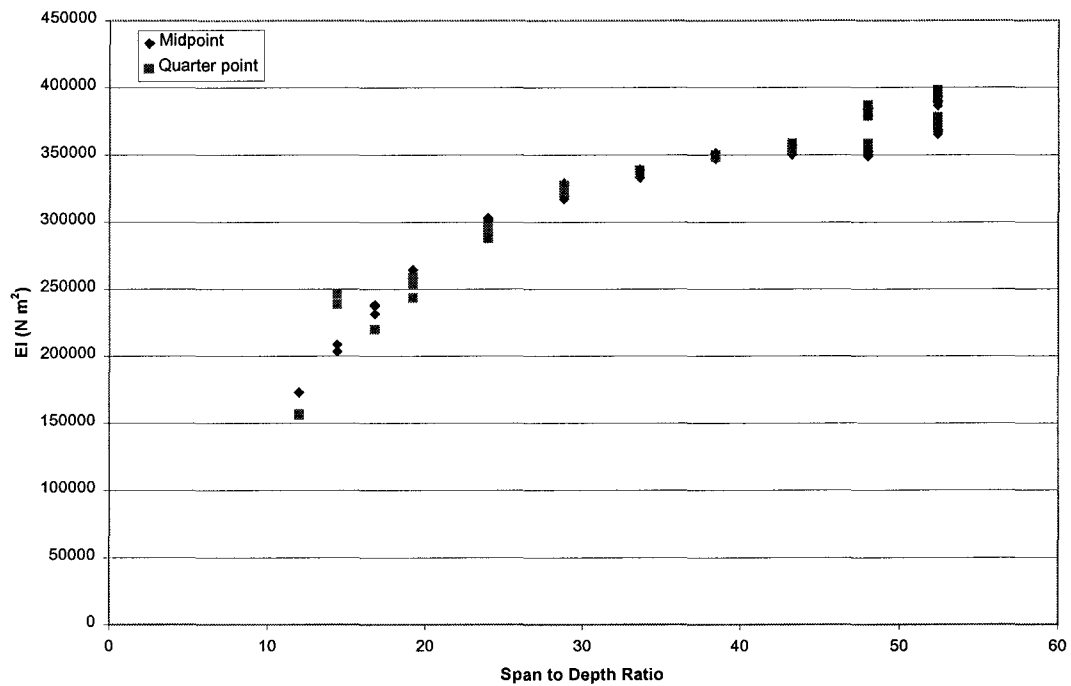


Figure 4.9: Variation of apparent flexural rigidity with span to depth ratio for two connected panels.

In both curves (mid and quarter point in Figure 4.7), the apparent flexural rigidity increases with increasing the span length, this suggests that a larger deflection contribution from the shear is present with shorter spans compared to longer ones.

Average cross sectional LVDT values (midpoint and quarter point) are used to form Figure 4.9, as can be seen the apparent flexural rigidity asymptotically approach 400 KNm^2 , the largest possible true flexural rigidity that can be determined by two-term Timoshenko's Equation. At a span to depth ratio of 55 the two values are very close. ASTM Test D 790 suggests a span to depth ratio of 16/1 or more to be used in beam tests to avoid shear effect. At this suggested ratio, the apparent flexural rigidity of the sheet pile panel accounts to only 44% of the true flexural rigidity. Thus the suggested ratio 16/1 cannot be applied to composites. A similar conclusion was drawn by Zweben(1979) and Bank (1989), who found that a ratio of at least 60 to 1 was necessary to attain the true flexural rigidity value. This is in agreement with the test results as shown in Figure 4.9.

4.3.4 Sensitivity Analysis

It was noticed during data processing that flexural rigidity (EI) was insensitive to the span and the number of data points. However, the value of the shear rigidity varied depending on how the data process was carried out. The flexural and shear rigidity determined in this thesis is the result of tests of 11 spans, from 1.5 m to 6.7 m, Table 4.2 and 4.3.

Table 4.2: Sensitivity of flexural and shear rigidity to data points.

Spans included in linear fit	Midpoint		Quarter point	
	EI (Nm ²)	KAG (N)	EI (Nm ²)	KAG (N)
1.5m, 1.8m, 2.1m, 2.4m, 3.1m, 3.7m, 4.3m, 4.9m, 5.5m, 6.1m, 6.7m (All spans)	401052	1233265	410479.1	1214253
1.8m, 2.1m, 2.4m, 3.1m, 3.7m, 4.3m, 4.9m, 5.5m, 6.1m, 6.7m	400970	1236456	409221.3	1250941
2.1m, 2.4m, 3.1m, 3.7m, 4.3m, 4.9m, 5.5m, 6.1m, 6.7m	400688	1245310	412433.1	1160041
2.4m, 3.1m, 3.7m, 4.3m, 4.9m, 5.5m, 6.1m, 6.7m	401811	1245310	411511.7	1185157
3.1m, 3.7m, 4.3m, 4.9m, 5.5m, 6.1m, 6.7m	401811	1207946	409786.4	1236525
3.7m, 4.3m, 4.9m, 5.5m, 6.1m, 6.7m	401620	1214236	407053.1	1332722
4.3m, 4.9m, 5.5m, 6.1m, 6.7m	399283	1306266	399455.3	1737523
4.9m, 5.5m, 6.1m, 6.7m	389819	1940103	383127.5	1737523
5.5m, 6.1m, 6.7m	444169	1984127	463885	1737523

Table 4.3: Sensitivity of flexural and shear rigidity to data points.

Spans included in linear fit	Midpoint		Quarter point	
	EI (Nm ²)	KAG (N)	EI (Nm ²)	KAG (N)
1.5m, 1.8m, 2.1m	447897	1110391	393472.9	1297873
1.5m, 1.8m, 2.1m, 2.4m	407341	1216093	364547.5	1421792
1.5m, 1.8m, 2.1m, 2.4m, 3.1m	402252	1235224	378782.9	1345333
1.5m, 1.8m, 2.1m, 2.4m, 3.1m, 3.7m	394773	1269932	401281.8	1235985
1.5m, 1.8m, 2.1m, 2.4m, 3.1m, 3.7m, 4.3m	389881	1301127	397772.8	1255141
1.5m, 1.8m, 2.1m, 2.4m, 3.1m, 3.7m, 4.3m, 4.9m	389881	1301127	441332.6	1235972
1.5m, 1.8m, 2.1m, 2.4m, 3.1m, 3.7m, 4.3m, 4.9m, 5.5m	401514	1236987	417676.5	1164972
1.5m, 1.8m, 2.1m, 2.4m, 3.1m, 3.7m, 4.3m, 4.9m, 5.5m, 6.1m	396818	1282219	406540.1	1253794
1.5m, 1.8m, 2.1m, 2.4m, 3.1m, 3.7m, 4.3m, 4.9m, 5.5m, 6.1m, 6.7m (All spans)	401051	1233262	410479	1214254

Figures 4.10 and 4.11 demonstrate the dependence of EI and KAG on the data points used in linear fit. Figure 4.10 presents EI and KAG as a function of smallest span included in linear fit for Timoshenko's equation. For instance, the first set of data had the smallest span of 1.5 m, meaning test data at spans of 1.5 m and longer will be used in linear fit. This was equivalent to all spans. EI and KAG determined at smallest span of 4.3 m had used test data at spans of 4.3 m and longer, i.e. 4.3, 4.9, 5.5, 6.1 and 6.7 m for linear fit. Obviously, EI was relatively stable and insensitive to data points, while KAG started to deviate significantly when test data of only large spans were used. Similar trend was observed in Figure 4.11, in which EI and KAG are plotted against largest span included in linear fit. For example the first set of data was computed from the tests at span of 2.1 m and smaller, meaning only 1.5, 1.8, and 2.1 m test data were used for linear fit. While EI was still close to a constant, KAG exhibited large discrepancy between the values calculated from midpoint deflection and from quarter point deflection, owing to insufficient data points. It is conclusive that, by using Timoshenko's equation, EI can be determined consistently even with only three small-span tests. However to obtain KAG with high confidence, tests of

different spans ranging from large to small are required. The small spans play important role to obtain the consistent *KAG*.

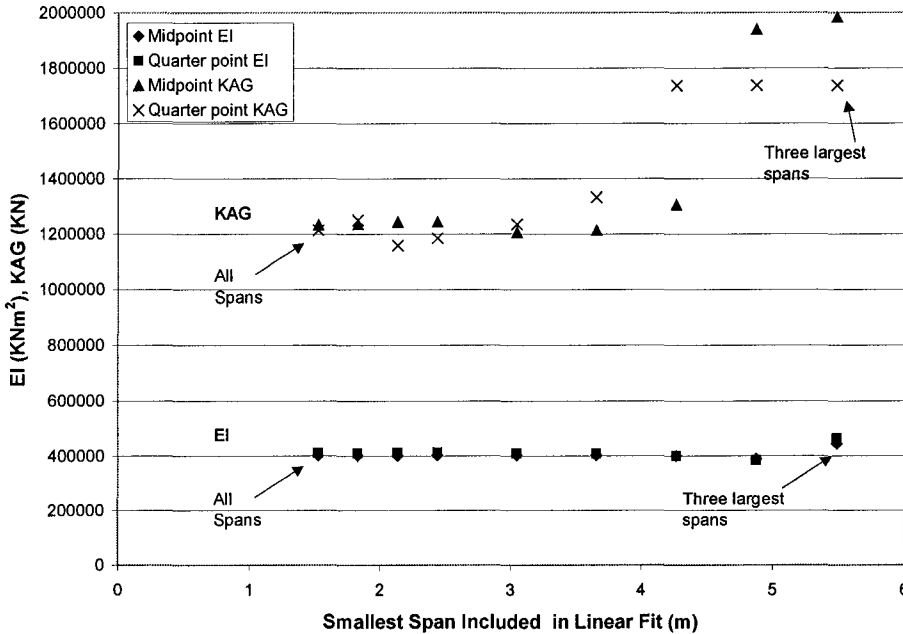


Figure 4.10: *EI* and *KAG* versus data points for linear fit (smallest span included)

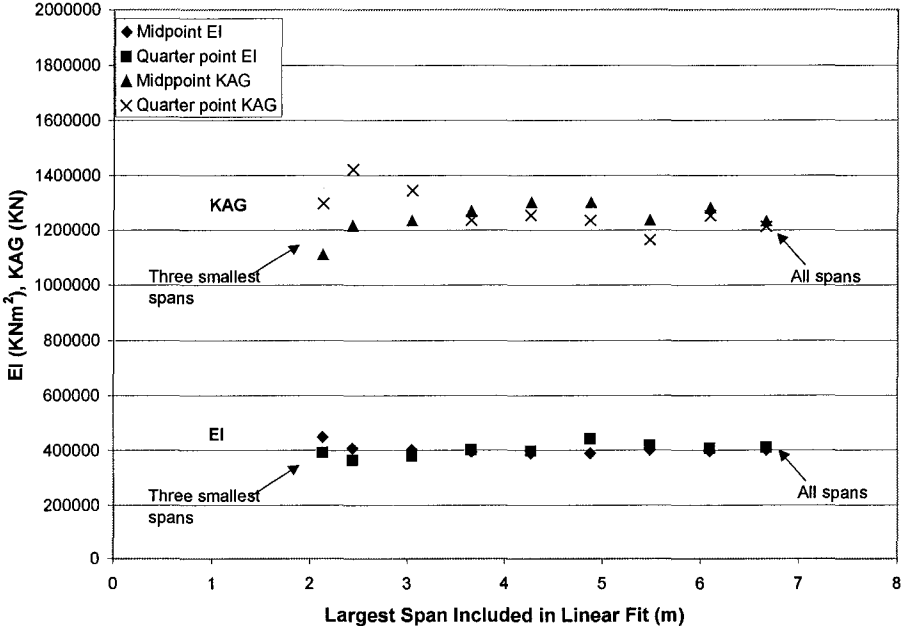


Figure 4.11: *EI* and *KAG* versus data points for linear fit (largest span included)

4.3.5 Flexural Rigidity from Strain Gauge Reading

From the classic beam theory, the flexural stress along the bottom fiber is given by Equation 4.5:

$$\sigma = \frac{Mz}{I} \quad 4.5$$

Where M = Bending moment, I = Moment of inertia of section, z = distance between neutral axis and bottom section fiber, for composite sheet pile section, $z = 0.065\text{m}$. Within the linear proportional limit, the tensile strain along the bottom fiber of the section (Figure 4.12) can be estimated by:

$$\varepsilon = \frac{Mz}{EI} \quad 4.6$$

Where E = Tensile elastic modulus of bottom fiber surface. Since the mid point in the 4 point bending setup (Figure 4.12) is subject to pure bending, the flexural rigidity EI can be determined from Equation 4.6 without shear effect. The tensile strain, ε , at the bottom surface of the section was measured by two strain gauges, one from each panel, and the bending moment, M , in the mid portion of the beam was computed by:

$$M = \frac{PL}{6} \quad 4.7$$

Typical curves of tensile strain versus applied load are shown in Figure 4.13 and 4.14 from two panels tested at 11 different spans. The tensile strain versus bending moment is plotted in Figure 4.15. When the span was larger than 2.1 m, all curves had the same slope, indicating that ε/M is a constant, thus EI can be determined by:

$$EI = \frac{z}{\text{Slope}} = \frac{0.0647}{171.33 \times 10^{-6}} = 377.8 \text{KNm}^2 \quad 4.8$$

Comparing this value to the true EI of 405.8KNm^2 (Table 4.1) gives an error of 6.8%.

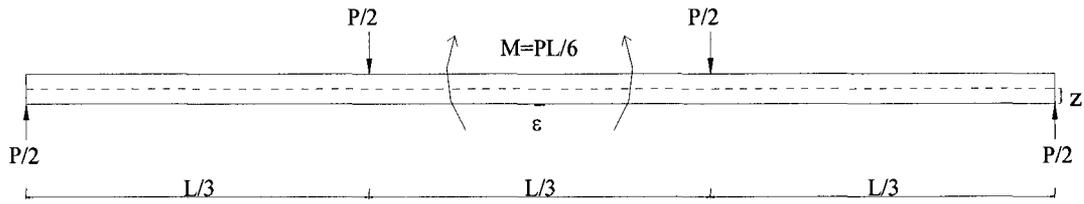


Figure 4.12: Pure bending of mid-span in 4 point bending setup

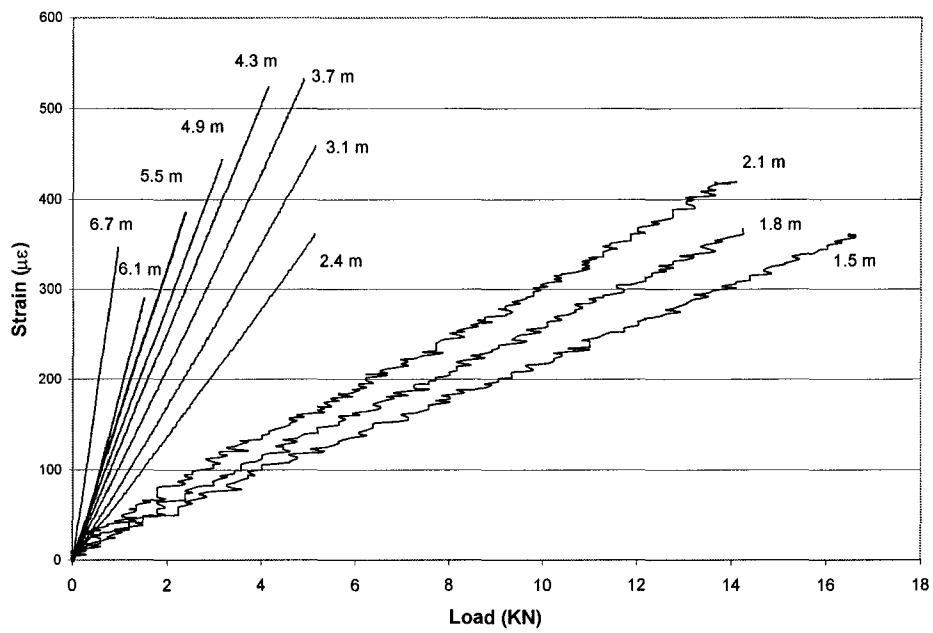


Figure 4.13: Tensile strain of bottom surface versus load
(from strain gauge 1)

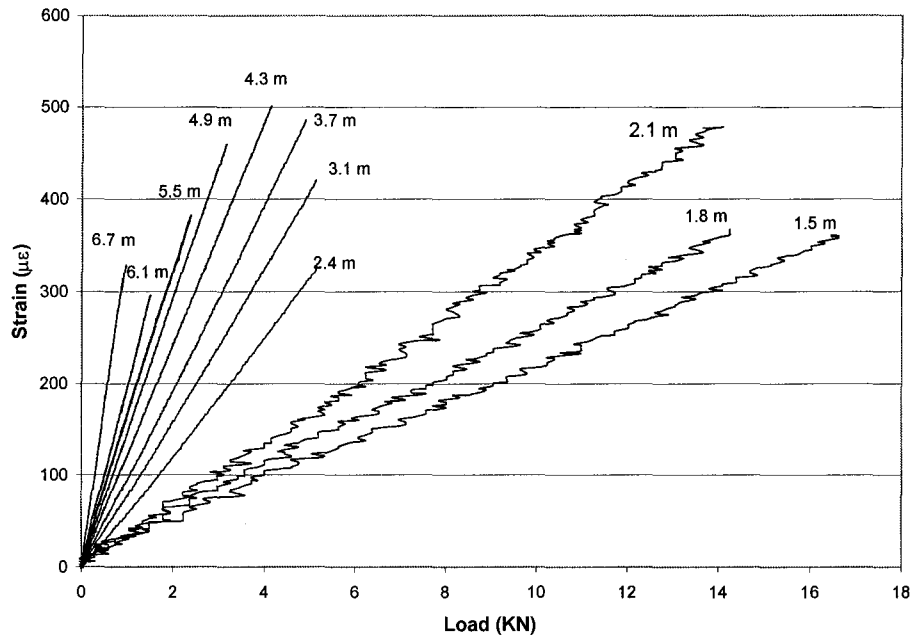


Figure 4.14: Tensile strain of bottom surface versus load
(from strain gauge 2)

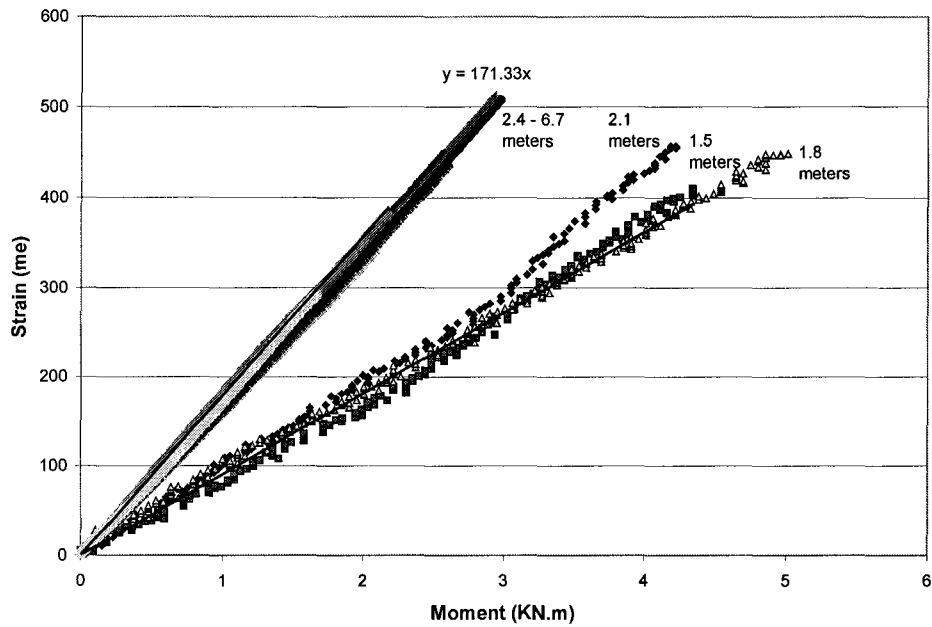


Figure 4.15: Tensile strains versus moment

4.3.6 Failure Test

Failure test was carried out to characterize the deformation and failure mode of connected panels. Four LVDTs were positioned across the mid-span cross section, LVDT 1 and 2 were positioned at the center, LVDT 3 at the extreme eye location, LVDT 4 at the extreme pin location (Figure 4.14). The purpose of such an arrangement was to monitor the possible twisting in the connected panels. Apart from the deflection readings, strain readings were also recorded throughout the test to enable the comparison with uni-axial coupon tests of bottom flange. The span tested was 4.6 meters (15 Ft) long, the selection of the span was to allow the comparison with pervious testes. The position of each sensor in the setup is shown in Figure 4.16.

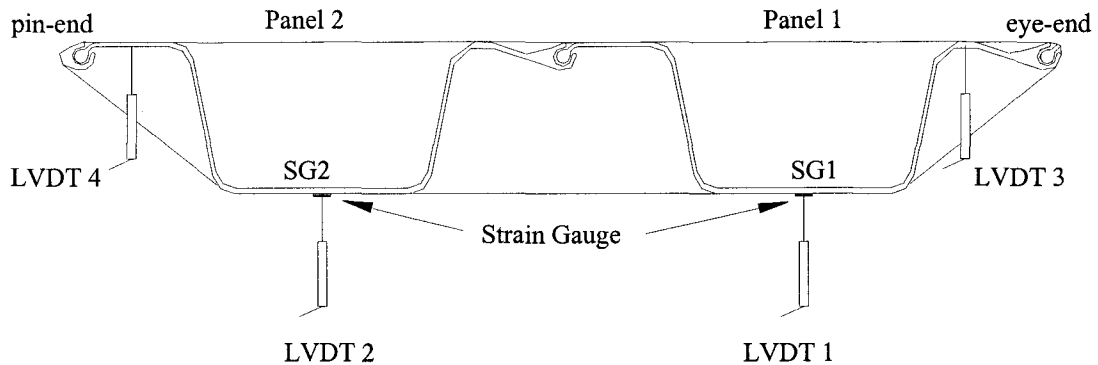


Figure 4.16: LVDT and strain gauge setup at midpoint in the failure test

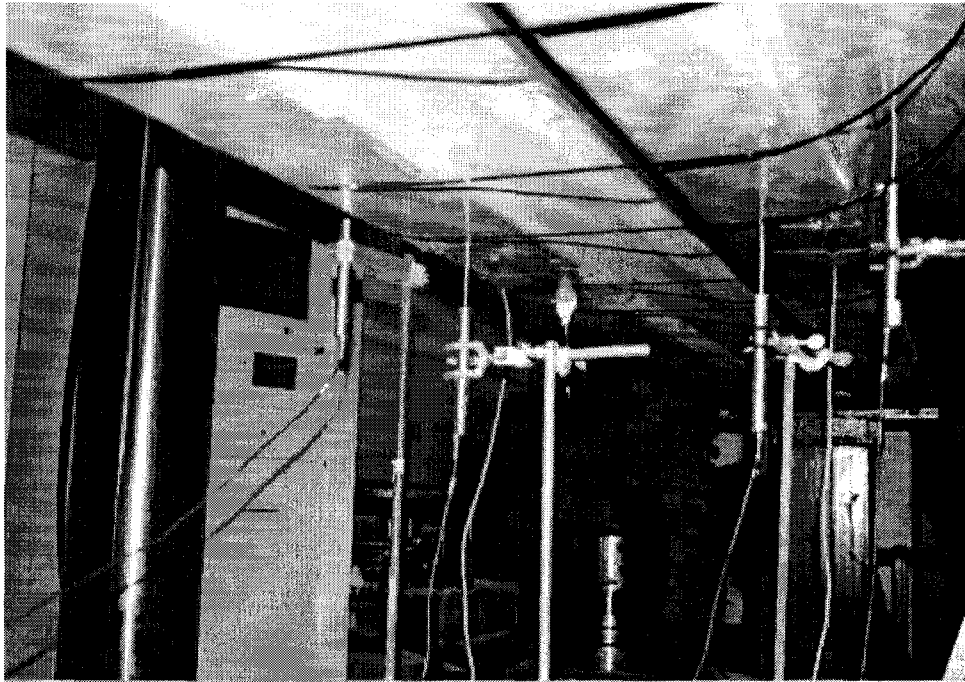


Figure 4.17: LVDT setup for the failure test

Figure 4.18 shows the typical four load deflection curves from the four LVDT readings. The deflection was not even, twisting started occurring after the deflection exceeded a value of approximately 28 mm. The relative deflection of pin-end to eye-end represented the twisting of the connected panel. The twisting can also be seen in Figure 4.19, panel 1 showed more twisting than panel 2. Giroux (2000) made a similar observation where the eye side of the panel deflected more than the pin side. Twisting became significant only after deflection reached 20 mm.

After the connected panels had deflected about 100mm, which corresponded to $L/46$ the test had to be stopped for safety reasons. Since the allowable deflection is not to exceed $L/60$ it was not necessary to continue the test. After unloading, a check was carried out to locate any cracks. The specimen was free from any visible cracks. The corresponding moment carried by the panels at the deflection of $L/46$ was about 13 KNm/m. This moment can be considered as load carrying capacity of the sheet pile panels at the given deflection, although no cracks were observed.

The load-deflection curves in Figure 4.18 exhibited non-linear response with a significant amount of deflection. Thus, failure of the panel is preceded by excessive deflection. This in turn creates the need for an additional criterion in the design, a deflection limit should be taken into consideration.

The use of the steel strapping simulated a more realistic testing procedure, the strapping prevented the sample from having local crushing, which was observed by Giroux (2000). No buckling waves were observed on the flanges between loading points. The strapping uniformly restrained the spans from lateral deflection.

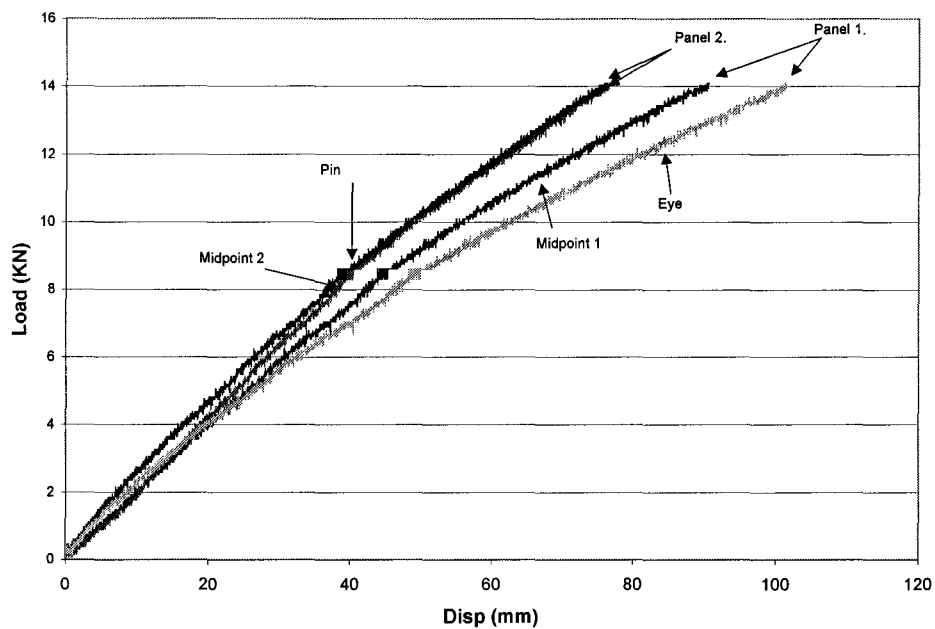


Figure 4.18: Typical load vs. deflection curves of failure test (4.6 m /15 Ft).

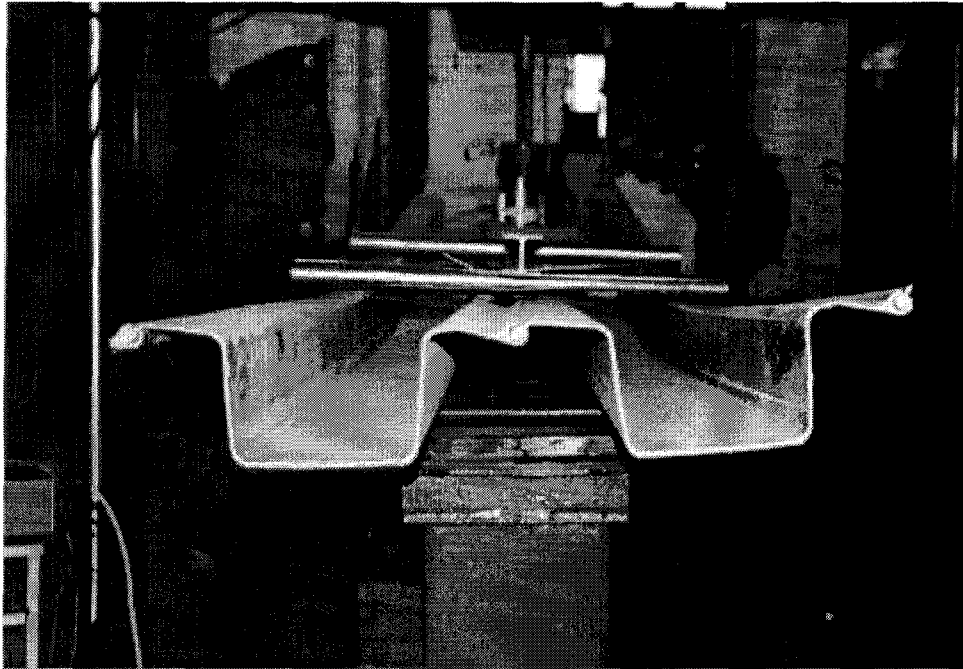


Figure 4.19: Twisting of the connected panels about the center

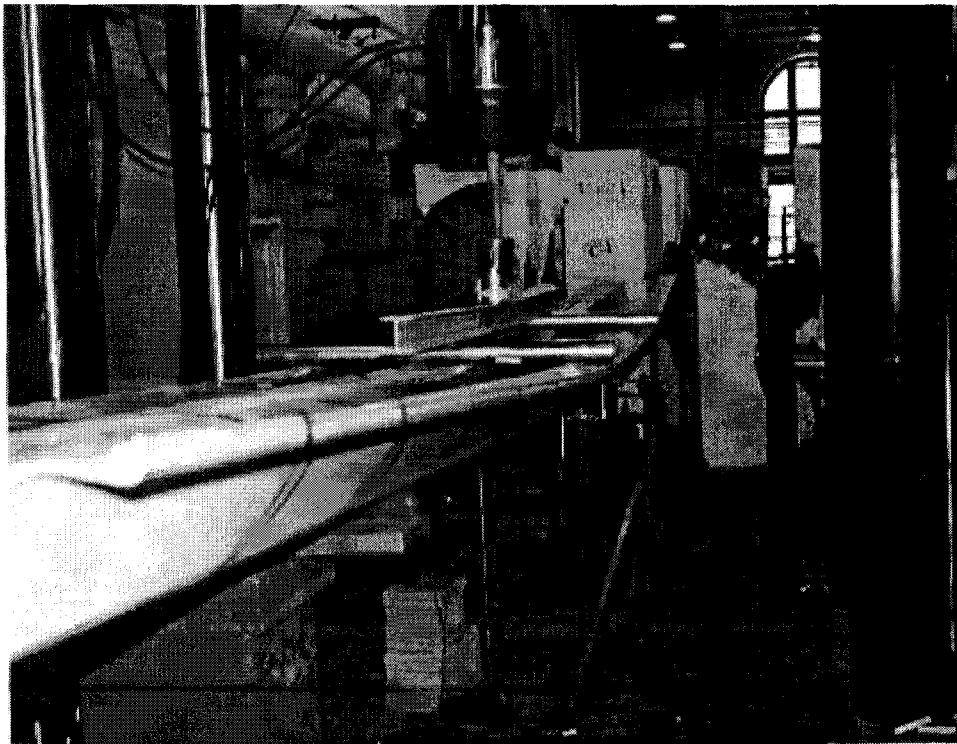


Figure 4.20: Excessive beam deflecting of connected panels in flexion

Figure 4.21 shows the complete load versus tensile strain curves up until the deflection reached to $L/46$. Panel 1 exhibited higher tensile strain due to the twisting. The maximum tensile strain developed in connected panels at a deflection of $L/46$ was about $2000\mu\epsilon$.

Composite coupons tests were performed to compare the tensile strain measured from uni-axial tension tests with that from the 4-point bending of full section tests. The tensile coupons were cut from the bottom flange, the same location on the section where the two strain gauges were fixed in full section tests. The tensile specimens were cut in the longitudinal direction of the sheet pile and the dog-bone shape was machined according to ASTM D 638 standard.

The tests were performed using an MTS machine, with a loading rate of 1.75 mm/min. An extensometer with a gauge length of 25.4 mm was used to measure the elongation and strain. Figure 4.22 shows typical tensile stress-strain curves of coupon tests. For a tensile strain of $2000\mu\epsilon$ developed in the sheet pile panel that corresponded to a deflection of $L/46$, it constituted only 14% of the tensile strain at failure of flange. It is unlikely that the composite sheet pile wall would fail by tensile fracture of the flange, a deflection-based design seems necessary.

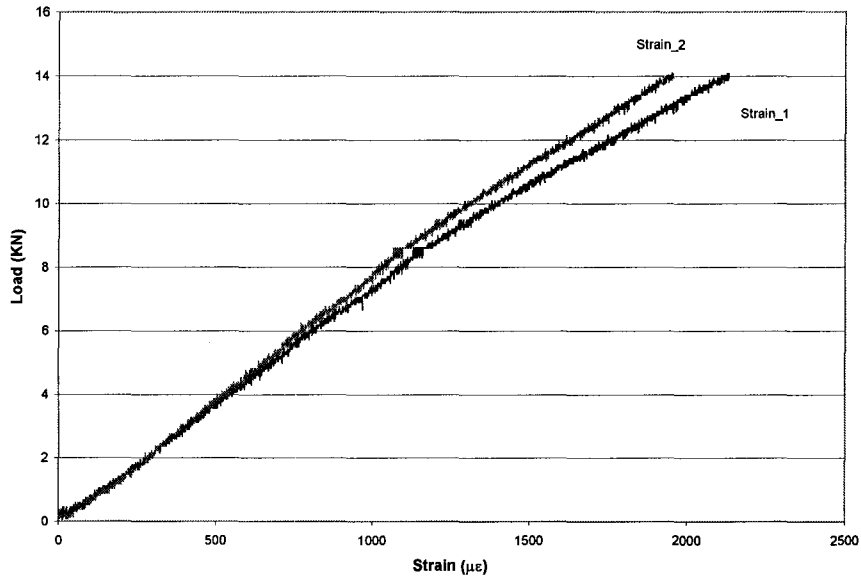


Figure 4.21: Load versus tensile strain curves up to a deflection of $L/46$ (span 4.6 m /15Ft)

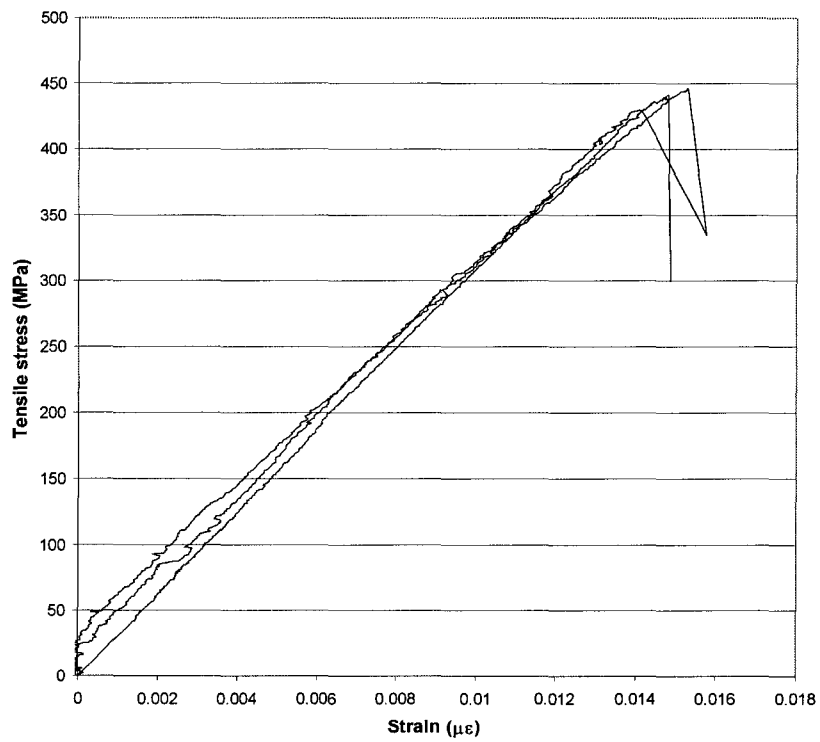


Figure 4.22: Uni-axial tensile stress strain curves of the flange coupon tests

Chapter 5

Development of Deflection-Based Design for Composite Sheet Pile Walls

5.1 Introduction

Deflection based design of composite sheet pile walls in sandy soil is to be developed in this chapter. Traditional free earth support method will be modified to allow the use of deflection limit set by design engineer. To find the relationship between maximum bending moment and maximum bending deflection and the relationship between maximum shear force and maximum shear deflection, earth pressure diagram will be simplified to a single triangular load with water level corrected by a factor. The contribution of the shear deflection to the total deflection will be represented by a shear factor. 16 cases of sheet pile walls with different wall height ranging from 1.5m to 4.5 m and with different water levels will be studied.

5.2 Traditional Free Earth Support Method

For a given anchored sheet pile wall design problem (Figure 5.1), the input design parameters are:

a = The anchor position from the ground surface level,

c = Distance from the ground surface level to the water level,

H = Height of the sheet pile wall,

H_w = Height of water,

γ = Unit weight of soil above the water table,

γ_{sat} = Unit weight of soil below the water table,

γ' = Effective unit weight of soil, $\gamma_{sat} - \gamma = \gamma_{sat} - 9.81 \text{ KN/m}^3$,

ϕ = Internal friction angle of sandy soil.

Composite sheet pile walls are relatively new. For a conservative design, the height of the wall currently used is limited to a range from 1.5 m to 4.5 m and the wall is always tied near the top to anchor plates. The anchor depth ' a ' is therefore equal to zero.

The computational output parameters are:

D = Penetration depth,

M_{max} = Maximum bending moment to be resisted by the sheet pile,

T = Anchor pull force.

Coarse-grain materials such as sands, gravel, and non-plastic silts are sufficiently pervious such that excess pore pressures do not develop when stress conditions are changed. Their shear strength is characterized by the angle of internal friction, ϕ determined from consolidated, drained tests. Table 5.1 shows the approximate relationship between the relative density, angle of internal friction, and the unit weight of granular soils.

Table 5.1: Granular soil properties [Design of Sheet Pile Walls 1996]

Compactness	Relative Density (%)	Angle of internal friction ϕ (degrees)	Unit Weight	
			Moist (KN/m ³) γ	Effective (KN/m ³) γ'
Very loose	0-15	<28	<15.71	<9
Loose	16-35	28-30	15-20	9-10
Medium	36-65	31-36	17-20	9-11
Dense	66-85	37-41	17-22	10-13
Very dense	86-100	>41	>20	>12

The lateral earth pressure will be developed with active pressures approximated behind the wall from the backfill and passive pressures in front of the wall below the dredge line.

The intensity of the active pressure at a depth, c , is

$$p_1 = \gamma c K_a \quad 5.1$$

Where K_a = Lateral active earth pressure coefficient.

The active pressure at the bottom of the wall (toe of wall) is:

$$p_2 = p_1 + \gamma'(H_w + D)K_a = (\gamma c + \gamma' H_w + \gamma' D)K_a \quad 5.2$$

The passive pressure at the bottom of the wall is:

$$p_3 = \gamma' DK_p \quad 5.3$$

Where K_p = Lateral passive earth pressure coefficient.

Either the Rankine or Coulomb earth pressure coefficients may be used for the earth pressure calculations. Although Coulomb values are generally preferred, they require the knowledge of angle of wall friction between composites and soil which is not currently available. Since Rankine coefficients used for K_a and K_p are slightly more conservative, this research will employ Rankine coefficients to calculate the earth pressure based on angle of internal friction ϕ of the sandy soil:

$$K_a = \frac{1 - \sin \phi}{1 + \sin \phi} \quad 5.4$$

$$K_p = \frac{1 + \sin \phi}{1 - \sin \phi} \quad 5.5$$

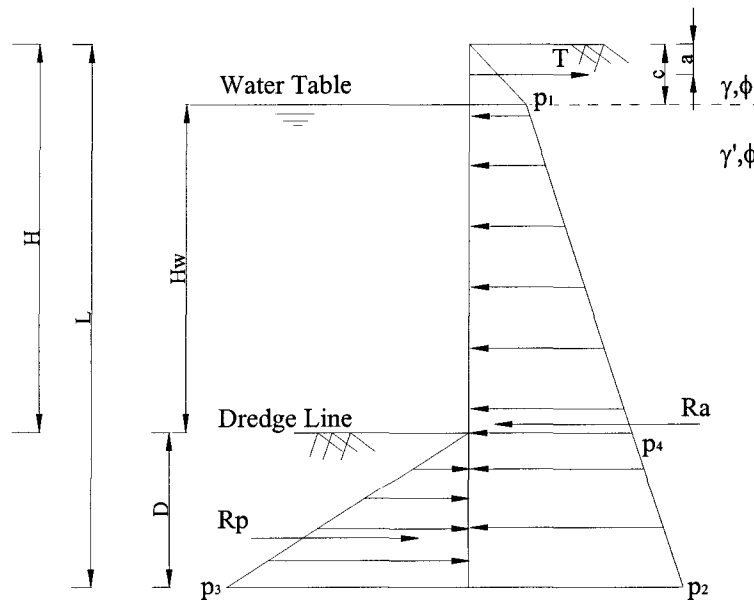


Figure 5.1: Load diagram for free earth support method

The following is an example of the free earth design method which will be used as control to compare the other modified method. The soil used in this investigation was taken as loose sand ($\phi=30^\circ$, $\gamma=19.62$ KN/m³, $\gamma_{sat}=19.49$ KN/m³, and $\gamma'=9.68$ KN/m³), where the wall height $H=4.5$ m, the water level $c=0.45$ m, ($c/H=0.1$), anchor position $a=0$ m, $H_w=4.05$ m.

(1) Depth of penetration (D):

From Equations 5.4 and 5.5,

$$K_a = 0.33, K_p = 3.0 \quad 5.6$$

Summing the moment about the anchor position and setting the sum to zero the equation to solve for the depth of penetration, D :

$$\sum M_{anchor} = 0 \quad 5.7$$

$$\begin{aligned} \sum M_{anchor} &= \frac{\gamma K_a c^2}{2} \left(\frac{2}{3} c - a \right) \\ &+ \gamma K_a c (H_w + D) \left(\frac{H_w + D}{2} + c - a \right) \\ &+ \gamma' \frac{K_a}{2} (H_w + D)^2 \left(\frac{2}{3} (H_w + D) + c - a \right) \\ &- \gamma' K_p \frac{D^2}{2} \left(\frac{2}{3} D + H_w + c - a \right) = 0 \end{aligned} \quad 5.8$$

Substituting the given values in Equation 5.8 gives:

$$\begin{aligned} M_{anchor} &= \frac{19.62 \times 0.333}{2} (0.45^2) \left(\frac{2}{3} 0.45 - 0 \right) \\ &+ 19.62 \times 0.333 \times 0.45 (4.05 + D) \left(\frac{4.05 + D}{2} + 0.45 \right) \\ &+ 9.68 \times \frac{0.333}{2} (4.05 + D)^2 \left(\frac{2}{3} (4.05 + D) + 0.45 - 0 \right) \\ &- 9.68 \times 3.0 \times \frac{D^2}{2} \left(\frac{2}{3} D + 4.05 + 0.45 - 0 \right) = 0 \end{aligned} \quad 5.9$$

By trial and error, we obtain $D=1.95$ m

(2) Anchor Pull force (T):

From equilibrium, equating the sum of the horizontal forces to zero, hence finding the anchor pull force, T :

$$\sum F_{Horizontal} = 0 \quad 5.10$$

Hence;

$$T = R_a - R_p \quad 5.11$$

The active resultant force can be evaluated by:

$$R_a = \frac{\gamma K_a}{2} (c)^2 + \gamma K_a (c)(H_w + D) + \frac{\gamma' K_a}{2} (H_w + D)^2 \quad 5.12$$

$$R_a = \frac{19.62 \times 0.33}{2} (0.45)^2 + 19.62 \times 0.33 (0.45)(4.05 + D) + \frac{9.68 \times 0.33}{2} (4.05 + D)^2$$

$$R_a = 0.662 + 2.943 \times (4.05 + D) + 0.150 \times (4.05 + D)^2$$
$$= 76.334 \text{ KN / m}$$

As for the passive pressure

$$R_p = \frac{\gamma'}{2} K_p D^2 \quad 5.14$$

$$R_p = 0.5 \times 9.68 \times 3.0 \times D^2 = 14.25 D^2 \quad 5.15$$
$$= 55.044 \text{ KN / m}$$

Thus $T = R_a - R_p = 21.29 \text{ KN/m}$

(3) Maximum Moment (M_{max}):

The location of the Maximum moment is at a depth ' x ' where the shear force is zero (Figure 5.2).

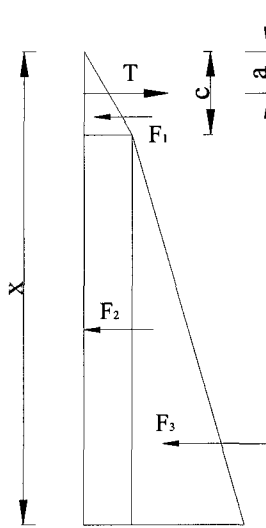


Figure 5.2: Sum of horizontal forces at a depth x .

Given $x > c$

$$\text{Find } x \text{ at which } \sum F_H = 0 = F_1 + F_2 + F_3 - T \quad 5.16$$

In other words, by trial and error find x (Figure 5.2),

$$c^2 \gamma K_a + c \gamma K_a (x - c) + \frac{(x - c)^2}{2} \gamma' K_a - T = 0 \quad 5.17$$

$x = 2.78\text{m}$ from the ground level ($x > c$)

Computing the moment about x given the maximum bending moment M_{max} :

$$M_{max} = F_1 \left(\frac{c}{3} + x - c \right) + F_2 \frac{(x - c)}{2} + F_3 \frac{(x - c)}{3} - T(x - a) \quad 5.18$$

The maximum moment to be resisted is:

$$M_{max} = 43.89 \text{ KNm/m}$$

As for the embedment depth, the value calculated has a factor of safety equal to unity.

To increase the margin of safety, a factor equal to the square root of two is multiplied by the depth to get the design depth (D_d). This method was suggested by Tschebotarioff (1973), and the USS Steel Sheet Piling Design Manual (1996).

$$D_d = \sqrt{2}D \quad 5.19$$

5.3 The Simplified Pressure Diagram

In order to develop a deflection based design method an analytical expression is needed to estimate the maximum deflection. The bilinear pressure diagram in (Figure 5.1) is not convenient to calculate deflection. It is therefore necessary to simplify the load diagram. This simplification is mainly the correction of the water level.

The proposed loading diagram is a conversion from a bilinear pressure distribution to a linear one, in other words combining the saturated and the dry soil unit weights into one that acts as a representative of the two (Figure 5.3).

The boundary conditions of the wall comprise of two pin supports, one is at the anchor force (A) and one at the toe of the wall (B), Figure 5.3. There is no force at point 'B' the wall can have an angle of rotation but cannot translate and thus a hinge is assumed. The boundary conditions for the wall was suggested by the US Army Corps of Engineers for Sheet Pile Walls design (1996). q_1 and q_2 are the active and the passive horizontal soil pressures per meter at the bottom of the loading diagram receptively. Two models were proposed to find the representative soil unit weight in a linear pressure diagram:

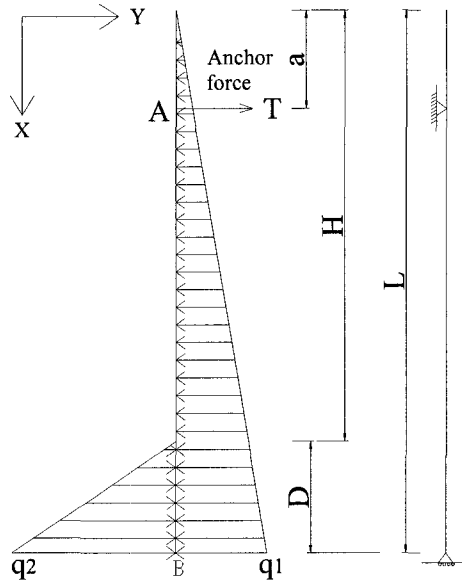


Figure 5.3: Simplified load diagram

(1) Average unit weight method

When Nataraj and Hoadley (1984) proposed the computational pressure diagram (CPD) (chapter 2), their main objective was to substitute the conventional bilinear triangle load diagram with a rectangular diagram

In their method, the average soil unit weight γ_{av} , was computed by equating linear pressure to bilinear pressure at the same dredge line level.

For the bilinear pressure load, the earth pressure at the dredge line p_4 (Figure 5.1) is given by:

$$p_4 = c\gamma K_a + H_w \gamma' K_a \quad 5.20$$

For the linear load, the pressure developed is:

$$p_4 = \gamma_{av} H K_a \quad 5.21$$

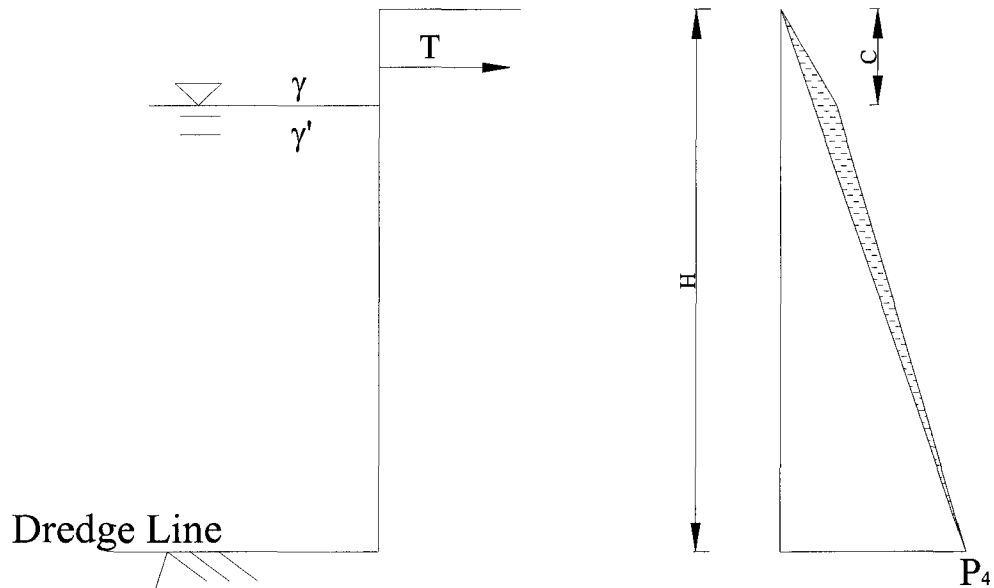


Figure 5.4: Average Soil Unit Weight

Equating the two horizontal earth pressures gives:

$$c\gamma K_a + H_w\gamma' K_a = \gamma_{av}HK_a \quad 5.22$$

Thus the average soil unit weight in the simplified linear pressure diagram is:

$$\gamma_{av} = \frac{c\gamma + H_w\gamma'}{H} \quad 5.23$$

As shown in Figure 5.4, there exists a difference that in related to water level.

(2) Equivalent force method.

An equivalent unit weight was found by equating the bilinear resultant force to the linear resultant force. Similarly, only the forces above the dredge line were considered.

This approach was used by Hagerty and Nofal (1992).

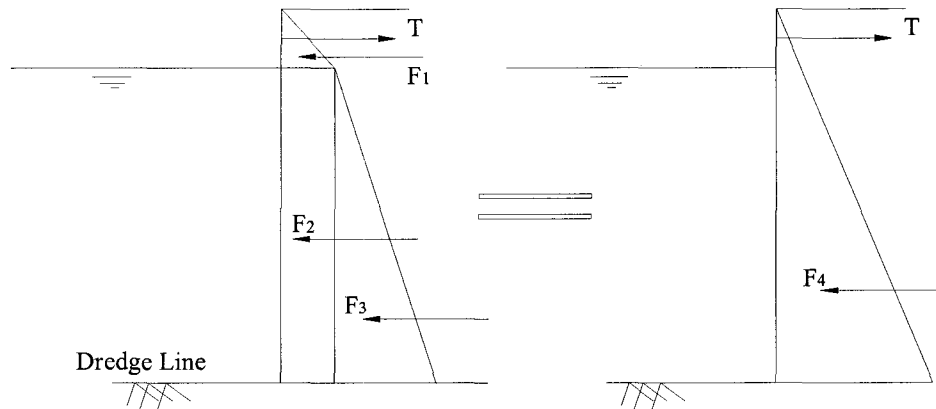


Figure 5.5: Equivalent force method ($F_1 + F_2 + F_3 = F_4$).

The equivalent soil unit weight is:

$$\gamma_E = \frac{c^2 \gamma + 2cH_w \gamma + \gamma' H_w^2}{H^2} \quad 5.24$$

In order to examine the effect of the two methods on the maximum moments, a comparison is made using the same parameters in section 5.1 case study. The linear load diagram in Figure 5.3, is assumed. γ_{av} (Equation 5.23) and γ_E (Equation 5.24) are used as the only unit weight of soil in calculation.

Thus the active resultant force is:

$$R_a = \frac{1}{2}(q_1 L) \quad 5.26$$

Where

$$q_1 = K_a L \gamma_{av} \quad \text{or} \quad 5.25$$

$$q_1 = K_a L \gamma_E$$

Similarly the passive resultant force:

$$R_p = q_2 \frac{D}{2} \quad 5.27$$

Where

$$q_2 = K_p D \gamma' \quad 5.28$$

Summing the horizontal forces, the anchor Force is:

$$T = R_a - R_p \quad 5.29$$

To find the position of M_{max} , the sum of the horizontal forces is equated to zero at a depth x ,

$$\sum F_H = T - \frac{q_1 x^2}{2L} = 0 \quad 5.30$$

Rearranging the terms, making x the subject of the formula:

$$x = \sqrt{\frac{2TL}{q_1}} \quad 5.31$$

The M_{max} is thus given by:

$$M_{max} = T(x - a) - \frac{q_1 x^3}{6L} \quad 5.32$$

Table 5.2: Comparison of simplified linear load pressure with bilinear load pressure.

Parameters	Bilinear load pressure (Figure 5.1)	Linear load pressure (Figure 5.3)			
	Free Earth Support Method	Average unit weight method (Eq. 5.23)	Difference	Equivalent force method (Eq. 5.24)	Difference
γ (KN/m ³)	$\gamma = 9.68$ $\gamma = 19.62$	$\gamma_{av} = 10.67$		$\gamma_E = 11.57$	
D (m)	1.95	1.94	-0.32 %	2.06	6.02 %
q_1 (KN/m ²)	22.29	22.92	2.79 %	25.31	13.55 %
T KN/m	21.29	19.11	-10.26 %	21.21	-0.38 %
M_{max} KNm/m	43.90	41.74	-4.9 %	46.89	6.82 %

As is seen from Table 5.2, finding the representative unit weight through the average method is a better approximation compared to that of the equivalent force method. The latter has an error of 6.82 % compared to 4.9 % with the former in regards to the maximum moment. However the equivalent force approximation gives a better anchor pull force estimation, since the goal is to introduce an equivalent maximum moment,

then the averaging method will be used. From another perspective, the deflection is more dependent on the moment rather than on the anchor force.

16 cases were studied to compare the effect of the simplified pressure diagram. The design parameters for each case are listed in Table 5.3. Since the currently installed composite wall heights ranged from 1.5-4.5m (3 to 15 Ft), these walls were relatively short, thus the anchors were usually placed at the top ($a=0$). The ratio of the water level to the height was varied from 0.1 to 0.4 (c/H). First, the 16 cases were solved using the free earth method with the bilinear pressure diagram as shown in Figure 5.1 as control for comparison, the results are summarized in Table 5.4. The maximum moment presented in Table 5.4 is not reduced. The depth of penetration, D , has a unit safety factor, thus this is not the design depth.

Table 5.3: The input parameters of the 16 case studies

Case	H (m)	c (m)	H_w (m)	a	c/H
1	4.5	0.45	4.05	0	0.1
2	4.5	0.9	3.6	0	0.2
3	4.5	1.35	3.15	0	0.3
4	4.5	1.8	2.7	0	0.4
5	3.5	0.35	3.15	0	0.1
6	3.5	0.7	2.8	0	0.2
7	3.5	1.05	2.45	0	0.3
8	3.5	1.4	2.1	0	0.4
9	2.5	0.25	2.25	0	0.1
10	2.5	0.5	2	0	0.2
11	2.5	0.75	1.75	0	0.3
12	2.5	1	1.5	0	0.4
13	1.5	0.15	1.35	0	0.1
14	1.5	0.3	1.2	0	0.2
15	1.5	0.45	1.05	0	0.3
16	1.5	0.6	0.9	0	0.4

Using the same penetration depth calculated by the bilinear load (Table 5.3) and the linear pressure diagram (Figure 5.3) with γ_{av} as unit weight of soils the maximum moment and the anchor pull force were computed for each case. The results are also shown in Table 5.4. Since the two calculations used same penetration depth, the differences in M_{max} and T were generated by the simplification of load diagram. The

error ranged from 6 to 10% in regard to the maximum moment, and 11-16 % in the anchor pull force. Therefore a correction factor should be introduced.

Table 5.4: Comparison of M_{max} and T calculated from bilinear and linear pressure diagrams.

Case	Bilinear Pressure Diagram			Linear Pressure Diagram			Difference (%)	
	D (m)	M_{max} (KNm/m)	T (KN/m)	D (m)	M_{max} (KNm/m)	T (KN/m)	% M_{max}	% T
1	1.957	43.899	21.290	1.957	41.064	18.898	-6.46%	-11.23%
2	2.083	51.633	25.195	2.083	46.880	21.265	-9.21%	-15.60%
3	2.213	59.377	28.617	2.213	53.976	24.006	-9.10%	-16.12%
4	2.335	66.955	31.594	2.335	62.535	27.156	-6.60%	-14.05%
5	1.514	20.655	12.879	1.514	19.321	11.432	-6.46%	-11.23%
6	1.620	24.294	15.241	1.620	22.057	12.864	-9.21%	-15.60%
7	1.721	27.937	17.312	1.721	25.396	14.522	-9.10%	-16.12%
8	1.816	31.503	19.112	1.816	29.423	16.428	-6.60%	-14.05%
9	1.082	7.527	6.571	1.082	7.0411	5.833	-6.46%	-11.23%
10	1.157	8.853	7.776	1.157	8.038	6.563	-9.21%	-15.60%
11	1.229	10.181	8.833	1.229	9.255	7.409	-9.10%	-16.12%
12	1.297	11.481	9.751	1.297	10.723	8.382	-6.60%	-14.05%
13	0.649	1.626	2.366	0.649	1.521	2.100	-6.46%	-11.23%
14	0.694	1.912	2.799	0.694	1.736	2.363	-9.21%	-15.60%
15	0.738	2.199	3.180	0.738	1.999	2.668	-9.10%	-16.12%
16	0.778	2.480	3.510	0.778	2.316	3.017	-6.60%	-14.05%

5.4 Correction of the Linear Pressure Diagram

The negative sign in the percentage difference in Table 5.4 indicates that the simplified linear diagram generated smaller maximum moment (M_{max}) and smaller anchor pull force (T). The reason is illustrated by Figure 5.6. The effect of the lost area on the maximum moment is not only dependent on the area size (force), but also on how far the force is away from the M_{max} position.

The objective of the correction is to find an equivalent active linear load in conjunction with the passive load to produce an identical M_{max} to that obtained by the bilinear pressure diagram. In this way, the percentage difference in maximum

moments can be reduced to near zero. This is accomplished by multiplying the q_1 by a correction factor, β , which is in turn determined by setting maximum moments from linear load and from bilinear load equal.

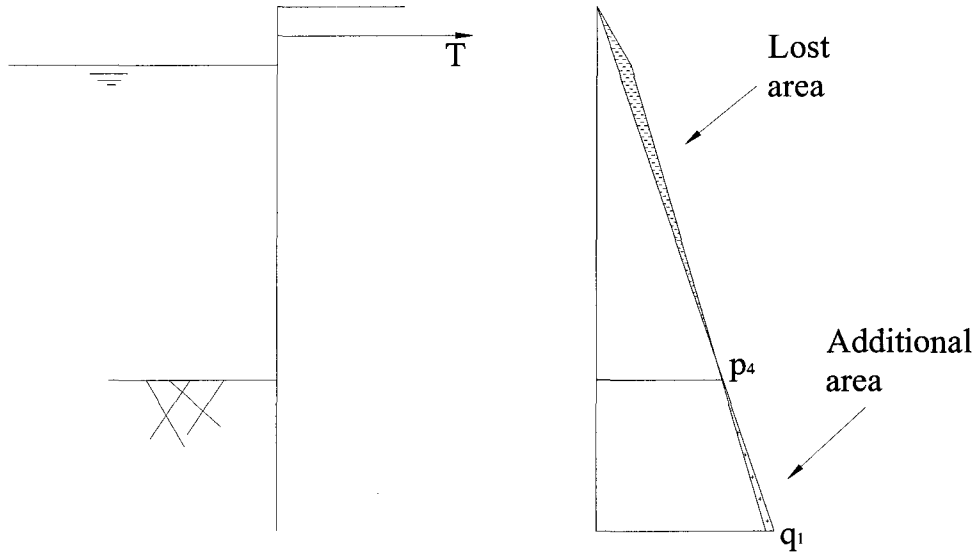


Figure 5.6: Active side area loss before correction

From Equation 5.25 and 5.23:

$$q_1^* = q_1 \beta = \gamma_{av} \beta L K_a = \left(\frac{c\gamma + H_w \gamma'}{H} \right) \beta L K_a = \left[\frac{c}{H} \gamma + \left(1 - \frac{c}{H} \right) \gamma' \right] \beta L K_a \quad 5.33$$

Where $L=H+D$

The β value for each case was found numerically using Microsoft Excel solver where β is adjusted until M_{max} from simplified linear diagram is equal to the M_{max} from the bilinear diagram. The results are presented in Table 5.5, it is noted that the β is not constant. Instead, it's case dependent.

Table 5.5: Correction factor β (for $\gamma=19.62$ KN/m³, and $\gamma=9.68$ KN/m³)

Case	Forced β	Ratio c/H
1	1.012765	0.1
2	1.018422	0.2
3	1.018193	0.3
4	1.013054	0.4
5	1.012765	0.1
6	1.018422	0.2
7	1.018193	0.3
8	1.013054	0.4
9	1.012765	0.1
10	1.018422	0.2
11	1.018193	0.3
12	1.013054	0.4
13	1.012765	0.1
14	1.018422	0.2
15	1.018193	0.3
16	1.013054	0.4

The correction factor, β , has a repetitive trend. For the same c/H ratio β is constant. The trend can be explained by Equation 5.33. Since β is used to correct γ_{av} , and γ_{av} is dependant on the ratio c/H . For a given c/H ratio, γ_{av} is constant. Therefore, the correction factor β should also be a variable. The correction factor β in Table 5.5 is only valid for the given soil condition.

In order to use the correction factor β for all c/H ratios, curve fitting was performed to obtain an equation to relate β to c/H (Equation 5.34). when $\beta=1$, water level is all the way up to the ground level ($c=0$). The load diagram is true linear distribution.

$$\beta = -0.1831\left(\frac{c}{H}\right)^2 + 0.0866\left(\frac{c}{H}\right) + 1 \quad 5.34$$

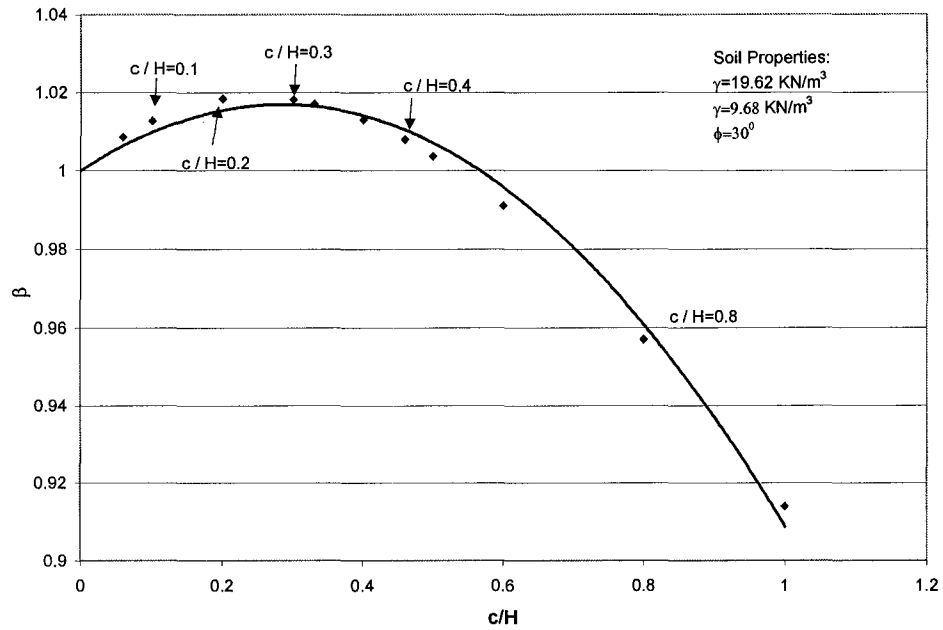


Figure 5.7: Correction factor β

With the correction factor β given by equation 5.34, the maximum moment and the anchor pull force from linear pressure diagram are calculated again, the results are compared with control in Table 5.6. The last two columns in Table 5.6 give the percentage difference. As is seen, the correction has nearly eliminated the moment difference and reduced the anchor force by nearly two folds.

Table 5.6: Result of the 16 cases after correction of linear pressure diagram.

Case	Bilinear pressure distribution			Linear pressure distribution			Difference	
	D (m)	M_{max} (KNm/m)	T (KN/m)	β (Eq. 5.34)	M_{max} (KNm/m)	T (KN/m)	% M_{max}	% T
1	1.957	43.899	21.290	1.013357	44.032	19.886	0.30	-6.59
2	2.083	51.633	25.195	1.016579	51.153	22.662	-0.93	-10.05
3	2.213	59.377	28.617	1.016175	58.772	25.544	-1.02	-10.74
4	2.335	66.955	31.594	1.012145	66.645	28.448	-0.46	-9.96
5	1.514	20.655	12.879	1.013357	20.717	12.030	0.30	-6.59
6	1.620	24.294	15.241	1.016579	24.068	13.709	-0.93	-10.05
7	1.721	27.937	17.312	1.016175	27.653	15.452	-1.02	-10.74
8	1.816	31.503	19.112	1.012145	31.357	17.209	-0.46	-9.96
9	1.082	7.527	6.571	1.013357	7.550	6.138	0.30	-6.59
10	1.157	8.853	7.776	1.016579	8.771	6.995	-0.93	-10.05
11	1.229	10.181	8.833	1.016175	10.078	7.884	-1.02	-10.74
12	1.297	11.481	9.751	1.012145	11.427	8.780	-0.46	-9.96
13	0.649	1.626	2.366	1.013357	1.631	2.210	0.30	-6.59
14	0.694	1.912	2.799	1.016579	1.895	2.518	-0.93	-10.05
15	0.738	2.199	3.180	1.016175	2.177	2.838	-1.02	-10.74
16	0.778	2.480	3.510	1.012145	2.468	3.161	-0.46	-9.96

5.5 Deflection Equations

In chapter 4, it was shown that a deflection criterion needs to be introduced in the wall design to take the problem of large deformation but small flexural stress/strain. Deflection equations are not readily available for the load shown in Figure 5.3. To derive the deflection equations the composite sheet piles are assumed to have linear elastic behavior. The boundary conditions are similar to that used by free earth support method:

- (1) No moment at point B.
- (2) No resultant force at point B.
- (3) No displacement at point B.
- (4) Pin support at point B.

The rigidities used in deflection calculations are given in Table 4.1,

$$EI = 494.871 \text{ KNm}^2/\text{m}$$

$$KAG = 1492.743 \text{ KN/m}$$

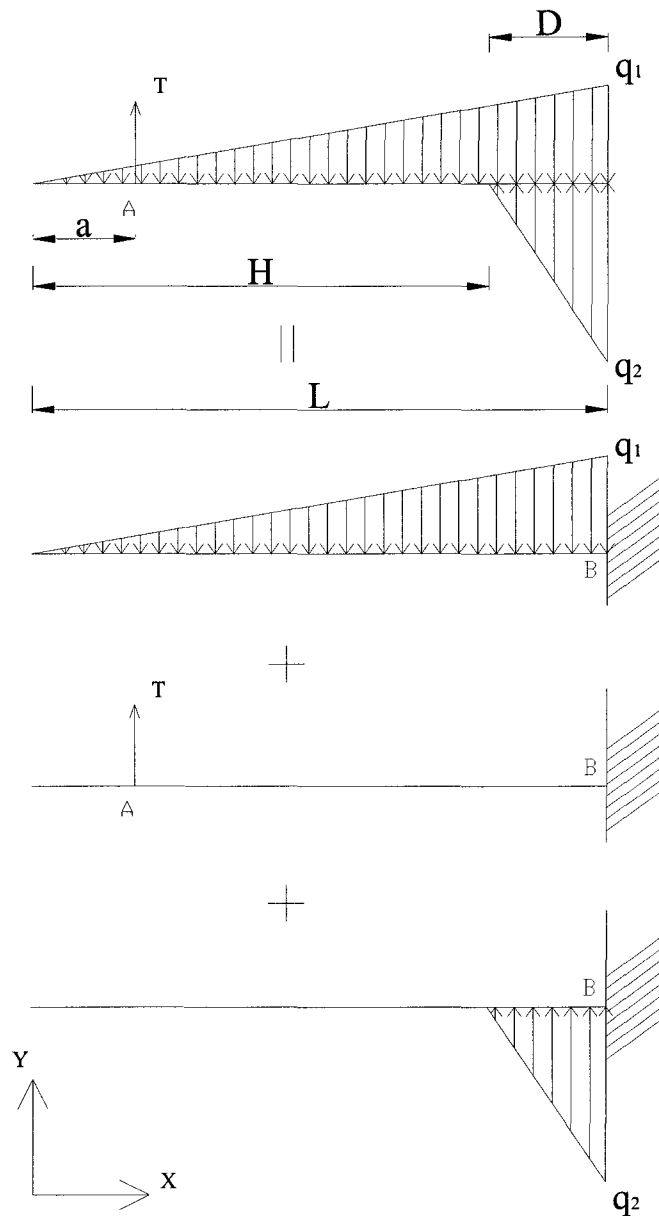


Figure 5.8: Loading diagram broken up

Moment area method with diagram by parts were used in derivation. The deflection due to bending (Y_b) is given by:

$$Y_b = \frac{-1}{12EI}(x-a) \left[\frac{q_1 a^3}{L}(L-a) + \frac{q_1}{10} \left(L^2 - \frac{a^3}{L} \right) (L-a) - (L-a)^2 (q_1 L - q_2 D) - \frac{q_2 D^4}{10(L-a)} \right]$$

$$\left. -(x-a)\frac{q_1 a^3}{L} - \frac{q_1}{10L}(x^3 - a^3)(x-a) + (q_1 L - q_2 D)(x-a)^2 \right] \quad 5.35$$

, a ≤ x ≤ H

Where

$$q_1 = K_a L \gamma_{av}$$

$$q_2 = K_p D \gamma'$$

A detailed derivation of the deflection equations is included in Appendix A.

$$\frac{dy}{dx} = \frac{V(x)}{KAG} \quad 5.36$$

Shear induced deflection is derived based on Timoshenko's equation. Integrating both sides of Equation 5.36 gives:

$$\int_0^{Y_s(x)} dy = \int_a^x \frac{V(x)}{KAG} dx \quad 5.37$$

And knowing $V(x)$, the shear deflection is given:

$$Y_s = \frac{1}{2KAG} \left[\frac{q_1}{3L}(x^3 - a^3) - (x-a)(q_1 L - q_2 D) \right] \quad 5.38$$

, a ≤ x ≤ H

Since composite sheet pile walls are usually anchored at top, $a=0$, the deflection equations can be simplified to:

$$Y_b = \frac{-1}{12EI} x \left[\frac{q_1}{10} L^3 - L^2(q_1 L - q_2 D) - \frac{q_2 D^4}{10L} - \frac{q_1}{10L} x^4 + (q_1 L - q_2 D)x^2 \right] \quad 5.39$$

, a ≤ x ≤ H

$$Y_s = \frac{1}{2KAG} \left[\frac{q_1}{3L} x^3 - x(q_1 L - q_2 D) \right] \quad 5.40$$

, a ≤ x ≤ H

Equation 5.35 and 5.38 were derived based on the simplified pressure diagram. With correction factor β , the effect of the simplified pressure diagram on the maximum

moment was minimized. However its effect on deflection was still not clear. In order to compare the deflections (Equation 5.39 and 5.40) generated by the simplified pressure diagram with that by the bilinear pressure diagram, the equilibrium method was used to calculate the moment distribution $M(x)$ in the wall by bilinear load.

Having the anchor at the top, the bilinear pressure profile was divided into 3 different sections:

- (1) $0 \leq x \leq c$ (increment depths of $(c-a)/5$ were used)
- (2) $c \leq x \leq H$ (increment depths of $H_w/30$ were used)
- (3) $H \leq x \leq L$ (increment depths of $D/30$ were used)

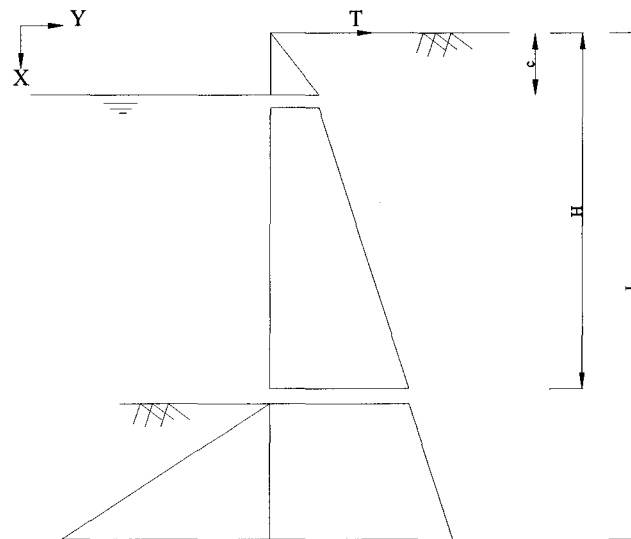


Figure 5.9: Three sections in bilinear load diagram.

Each section was divided into several elements. Section 1 was cut into 5 elements, section 2 into 30 elements, and section 3 into 30 elements. Two typical top elements are shown in Figure 5.10. For n^{th} element, at a distance Δ_i from the top, bending moment M_i and shear force V_i were calculated by equilibrium. Having the values of the depth and its corresponding bending moment, using the MathPad Curve fitter software, the equation of the moment profile $M(x)$ was found.

The moment induced deflection due to bilinear loads as shown in Figure 5.9 was thus determined by:

$$Y_b = \iint \frac{M}{EI} dx + c_1 x + c_2 \quad 5.41$$

With the boundary conditions:

$$Y_b|_{x=0} = 0$$

$$Y_b|_{x=L} = 0$$

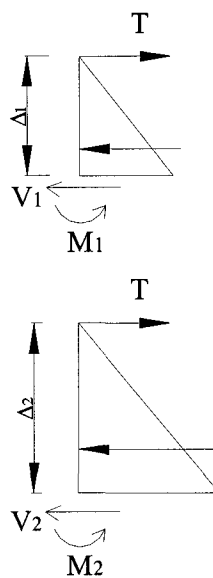


Figure 5.10: A blow up of element calculations

Case 1 was used as an example again to illustrate the method. The parameters in case 1 were: $a=0$, $c=0.45\text{m}$, $H=4.5\text{m}$, and $H_w=4.05\text{m}$. Using the MathPad Curve fitter software, the bending moment profile was fitted with a polynomial of degree 7. Figure 5.11 gives the entire moment diagram of the wall, with points from the finite difference analysis, and a solid line from curve fitting. The expression for $M(x)$ is given by:

$$M = -0.0457 - 19.581x - 5.041x^2 + 6.47x^3 - 2.825x^4 + 0.667x^5 - 0.075x^6 + 0.003x^7 \quad 5.42$$

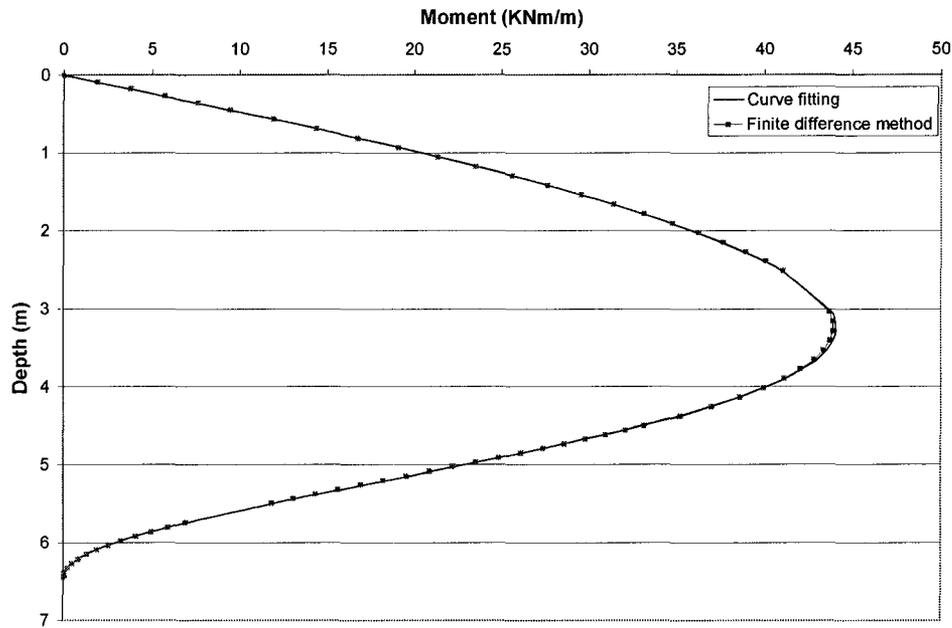


Figure 5.11: Bending moment distribution due to bilinear load (Case 1).

Integrating Equation 5.42 twice, and applying the boundary conditions gave the final bending expression in Equation 5.43 with $c_2=0$, and $c_1=87.6$.

$$Y_b EI = 87.582x - 0.023x^2 - 3.264x^3 - 0.420x^4 + 0.324x^5 - 0.0942x^6 + 0.0159x^7 - 1.340 \times 10^{-3}x^8 + 4.167 \times 10^{-5}x^9 \quad 5.43$$

The complete deflection profile is plotted in figure 5.12. The method to find the deflection profile is rather laborious and time intensive, in addition, the surface generation is case dependent, meaning there is no general equation that can be utilized for a random case.

Since the analytical deflection equations (Equation 5.39-5.40) are applicable only within the wall height ($0 \leq x \leq H$), three deflection profiles are compared in Figure 5.13 within the same range. The two profiles, one from the integration method and the other from the analytical equation (Equation 5.39 with $\beta = 1.0128$) are very close (1.51% difference). Deflection under the linear pressure diagram without correction ($\beta=1.0$) exhibits large deviation. Table 5.7 summarizes the results for Case 1, the total

height of sheet pile wall ($L = D + H$) was 6.4 m and the maximum deflection occurred was 0.36 m, the corresponding deflection limit was $L/18$ by using traditional free earth support method. Differentiating the moment Equation 5.42 gives the shear function $V(x)$. Figure 5.14 shows the shear force distribution along depth.

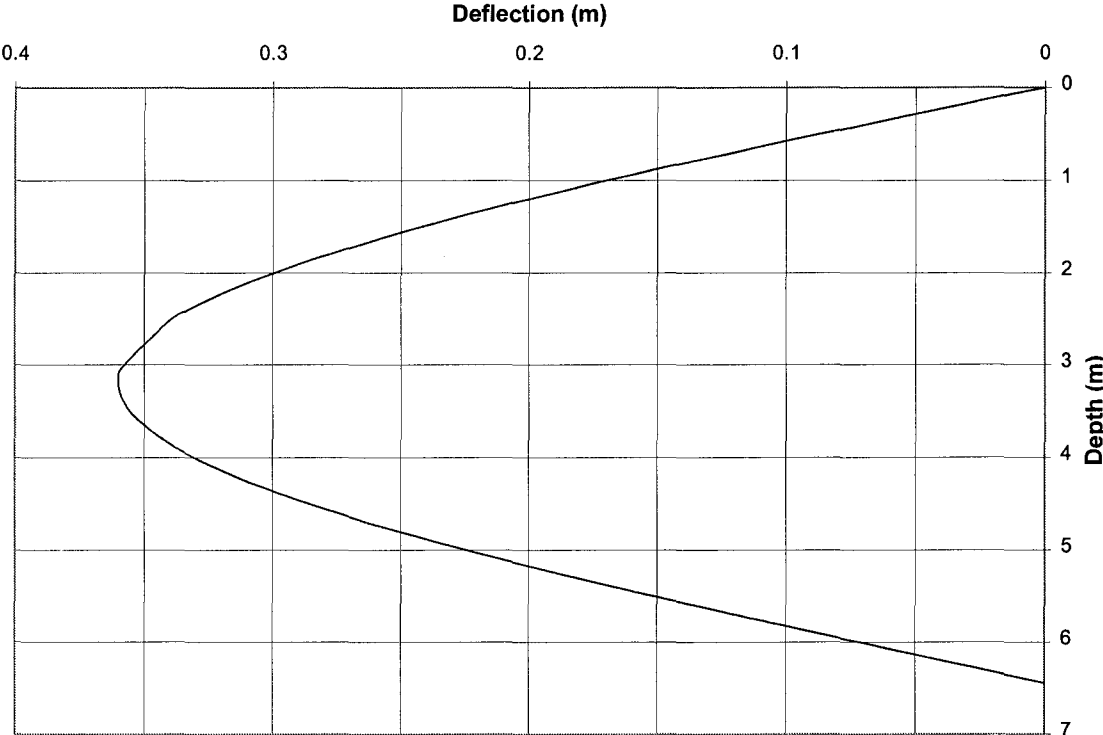


Figure 5.12: Bending deflection profile due to bilinear pressure diagram (Case 1).

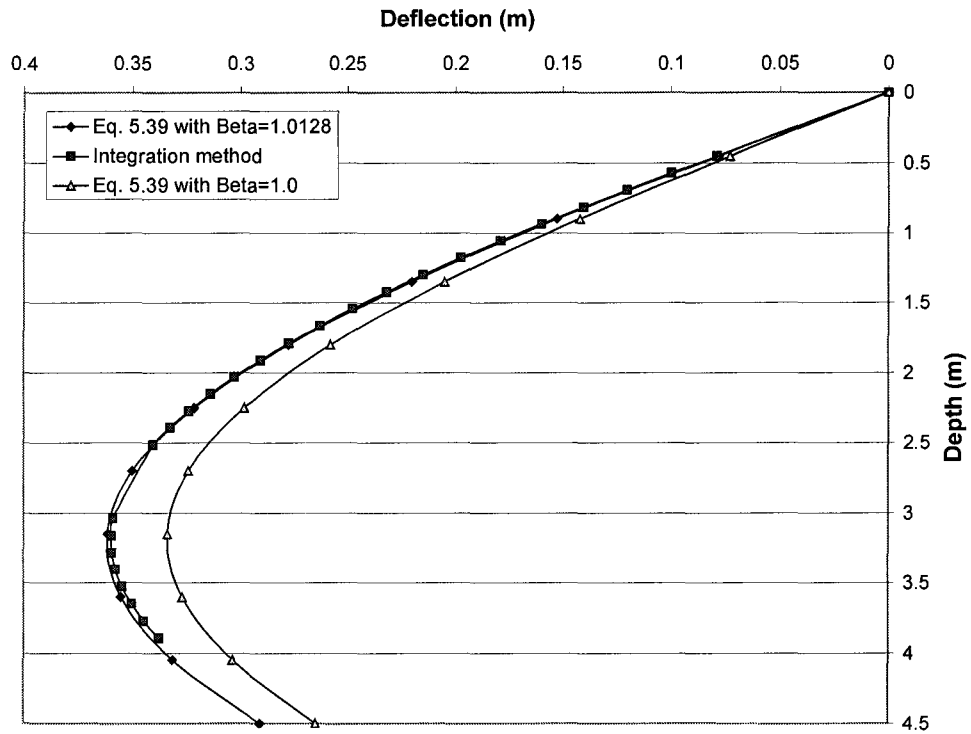


Figure 5.13: Bending deflection comparison (Case 1).

Table 5.7: Deflection position and value comparison.

Method	Integration Method, With bilinear pressure diagram	Eq. 5.39 with linear pressure Diagram $\beta=1.0$	Eq. 5.39 with linear pressure Diagram $\beta=1.0128$	% Difference	
				Uncorrected $\beta=1.0$	Corrected $\beta=1.0128$
Position of maximum deflection	3.184m	3.189m	3.218m	0.13%	1.05%
Value of Deflection	0.3597m	0.3337m	0.3616m	-7.254%	1.33%

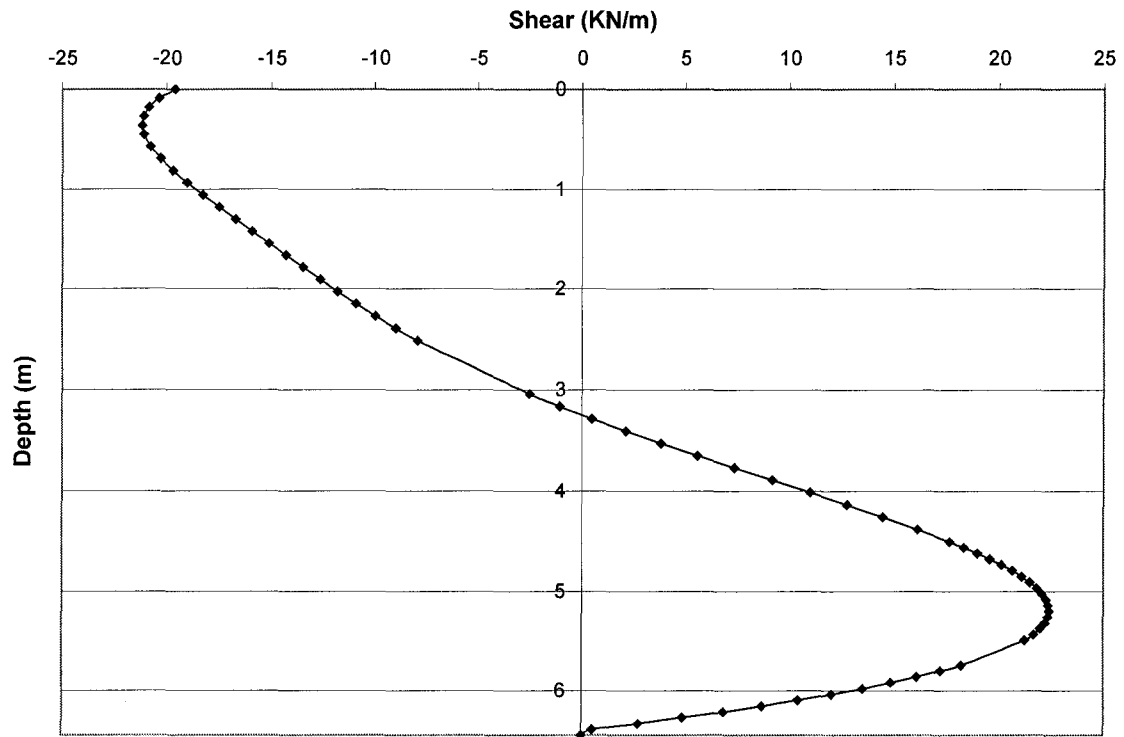


Figure 5.14: Shear force distribution due to bilinear load (Case 1.).

Maximum bending deflection and maximum shear deflection of 16 cases were computed based on Equation 5.39 and 5.40, and on the correction factors, β , (Equation 5.34) within the height of sheet pile walls ($0 \leq x \leq H$). Microsoft Excel's solver was used to find the maximum of both deflections. The results are summarized in Table 5.8.

Table 5.8: $(Y_b)_{max}$ and maximum shear deflection, $(Y_s)_{max}$.

Case	$(Y_b)_{max}$ (m)	$(Y_s)_{max}$ (m)
1	0.362863	0.029493
2	0.44029	0.034263
3	0.52733	0.039367
4	0.621712	0.04464
5	0.103281	0.013877
6	0.125319	0.016121
7	0.150093	0.018522
8	0.176957	0.021004
9	0.019203	0.005057
10	0.023301	0.005875
11	0.027907	0.00675
12	0.032902	0.007654
13	0.001493	0.001092
14	0.001812	0.001269
15	0.001857	0.001458
16	0.002558	0.001653

5.6 Relationship between M_{max} and $(Y_b)_{max}$.

It would be useful if a relationship between M_{max} and $(Y_b)_{max}$ could be established. The target equation is likely to be:

$$(Y_b)_{max} = \frac{M_{max} L^2}{\alpha EI} \quad 5.44$$

For a simply supported beam subjected to triangular distributed load (Figure 5.15), the maximum moment is given by equation 5.45.

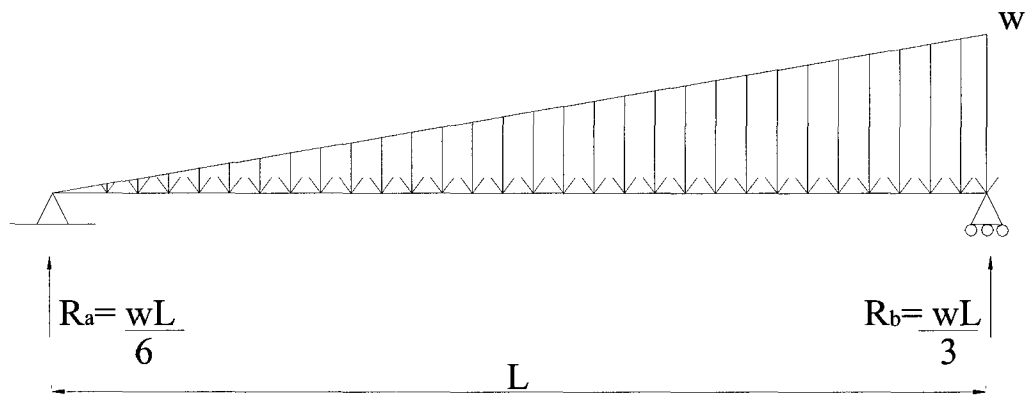


Figure 5.15: Simple triangular loading

$$M_{max} = \frac{wL^2}{9\sqrt{3}} \quad 5.45$$

The corresponding maximum deflection is given by:

$$(Y_b)_{max} = 0.00652 \frac{wL^2}{EI} \quad 5.46$$

Substituting M_{max} and $(Y_b)_{max}$ into Equation 5.44 solves the constant, α , for the given load shown in Figure 5.15:

$$\alpha = \frac{M_{\max} L^2}{(Y_b)_{\max} EI} = 9.843 \quad 5.47$$

The same principle was applied to the 16 case studies with the load diagram given in Figure 5.3. In each case using the linear pressure diagram, M_{\max} (Table 5.6) and $(Y_b)_{\max}$ (Table 5.8) were calculated. The target Equation 5.44 was assumed again and plotting $(Y_b)_{\max}/L^2$ versus M_{\max} gave a perfect straight line with slope = $0.0002=1/(\alpha EI)$. This is shown in Figure 5.16.

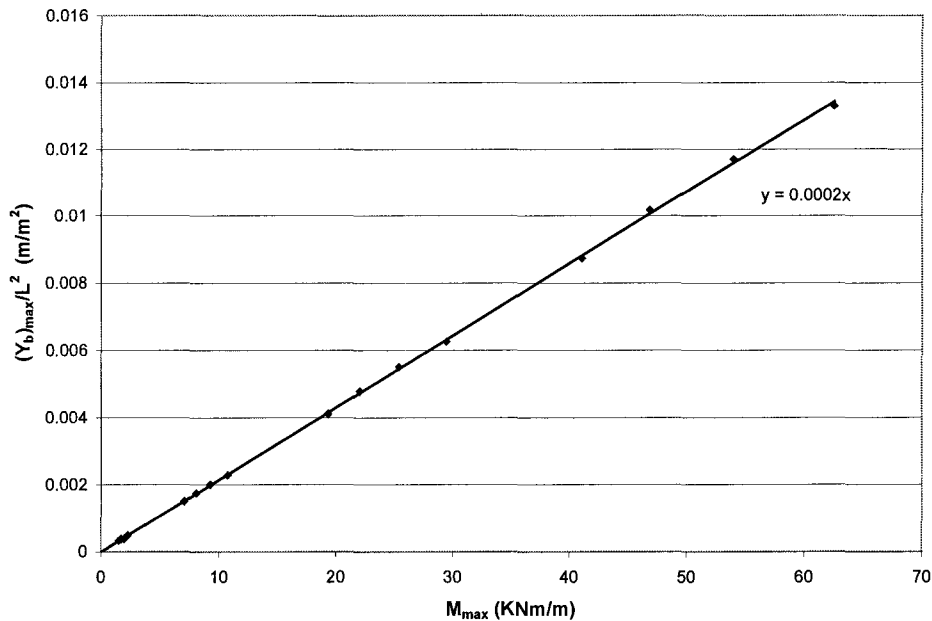


Figure 5.16: Relationship between $(Y_b)_{\max}$ and M_{\max}

For the composite section with $EI = 494.871 \text{ KNm}^2/\text{m}$ (Table 4.1), $\alpha = 10.1$, which was very close to the value of 9.843 calculated from the single triangle loading (Equation. 5.47), although the load conditions were different. Direct relationship between M_{\max} and $(Y_b)_{\max}$ was thus established:

$$(Y_b)_{\max} = \frac{M_{\max} L^2}{10.1EI} \quad 5.48$$

Instead of using Equation 5.39 to compute the $(Y_b)_{\max}$, it is now possible to use M_{\max} to do the same calculation. Since M_{\max} is always needed in design, use of Equation 5.48 is more convenient and less time consuming. It is interesting to notice that $\alpha=10.1$ is

independent from EI , since $(Y_b)_{max}$ is also proportional to $1/EI$ in Equation 5.39, therefore, Equation 5.48 is valid for sheet pile walls made of any material.

5.7 Relationship between V_{max} and $(Y_s)_{max}$.

Similarly, there probably exists a relationship that links the maximum shear force with maximum shear deflection. It is important for composite structure to take shear-induced deflection into consideration, since the shear modulus is only about one tenth of Young's modulus. The target equation is likely to have the form:

$$(Y_s)_{max} = \frac{V_{max} L}{\alpha' KAG} \quad 5.49$$

Where α' is a constant, KAG the shear rigidity, L the sheet pile length and V_{max} the maximum shear force. For the single triangle loading shown in figure 5.15 the shear force equation is:

$$V(x) = \frac{wL}{6} - \frac{wx^2}{2L} \quad 5.50$$

From Timoshenko's beam equation, the deflection is computed by:

$$Y_s = \int_0^x \frac{V(x)}{KAG} = \frac{1}{KAG} \left(\frac{wLx}{6} - \frac{wx^3}{6L} \right) \quad 5.51$$

Differentiating equation 5.51 gives the x value at maximum shear deflection $(Y_s)_{max}$,

$V(x)=0$:

$$x = L\sqrt{\frac{1}{3}} \quad 5.52$$

Substituting the x in the Equation 5.51 by Equation 5.52 gives the maximum shear deflection:

$$(Y_s)_{\max} = \frac{wL^2}{KAG} \left(\frac{1}{6} \sqrt{\frac{1}{3}} - \frac{1}{6} \left(\frac{1}{3} \right)^{\frac{3}{2}} \right) = 0.064 \frac{wL^2}{KAG} \quad 5.53$$

V_{\max} occurs when $x=L$, from Eq. 5.50:

$$V_{\max} = \frac{WL}{3} \quad 5.54$$

Substituting Equations 5.53 and 5.54 in target Equation 5.49, the value of the shear constant α' is found to be 5.2.

Data of $(Y_s)_{\max}/L$ Vs. V_{\max} are plotted in Figure 5.17 for the 16 cases V_{\max} given in Table 5.10 and $(Y_s)_{\max}$ in Table 5.8. Data points corresponding to the same c/H ratio lie on the same straight line. Thus for a given c/H ratio, a linear relationship exists between the shear force V_{\max} and the $(Y_s)_{\max}/L$. The slopes of the 4 straight lines range from 0.0024 for $c/H=0.1$ to 0.0029 for $c/H=0.4$ (Table 5.9). For $KAG = 1492.743$ KN/m, α' is computed by:

$$\alpha' = \frac{V_{\max}}{(Y_s)_{\max} KAG} = \frac{1}{(\text{slope})KAG} \quad 5.55$$

Table 5.9: α' for corresponding c/H ratios.

c/H ratio	Slope (m/KN)	α'
0.1	0.00024	2.791
0.2	0.00025	2.679
0.3	0.00027	2.481
0.4	0.00029	2.310

Writing the constant α' in terms of c/H gives:

$$\alpha' = -1.641 \frac{c}{H} + 2.9755 \quad 5.56$$

Thus the general relationship becomes:

$$Y_s = \frac{V_{\max} L}{\left[-1.641 \frac{c}{H} + 2.9755 \right] KAG} \quad 5.57$$

It is noticed that, the α' calculated from single triangular load, $\alpha'=5.2$ (Figure 5.15) and from two triangular-load, $\alpha'=2.31-2.79$ (Figure 5.3) are quite different. The passive side earth pressure probably has more effect on shear force than on bending moment.

It should be pointed out that the two deflection maximums induced by the moment and shear do not lie at the same depth, however they are very close. Figure 5.18 illustrates this difference by using Case 1 as an example.

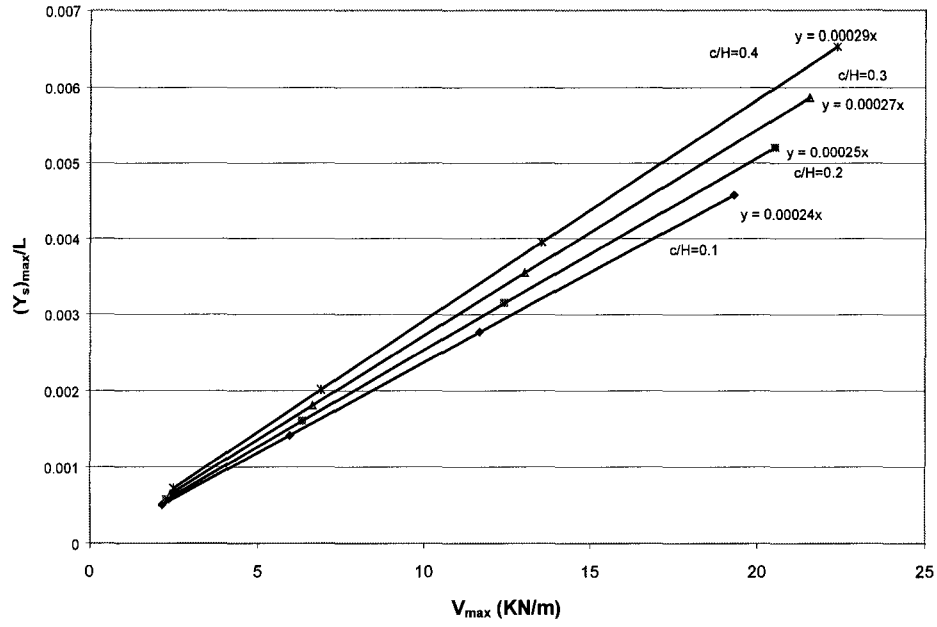


Figure 5.17: Relationship between $(Y_s)_{max}$ and V_{max} .

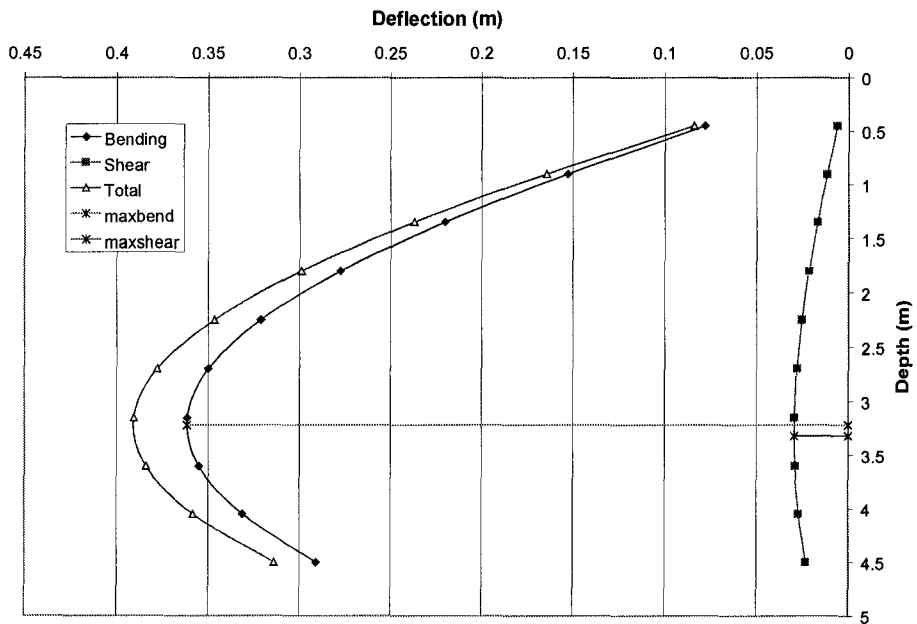


Figure 5.18: Locations of maximum bending and shear deflection (Case 1).

5.8 Rowe's Moment Reduction:

Field experience showed that, for anchored sheet pile walls, designs based on the classical earth pressures were over conservative in terms of the thickness of the material section required to support the soil (Rowe 1952). It is now accepted that bending moment in the sheets are affected by the deflected shape of the pile, and that this is a function of the flexibility of the wall relative to the soil. The deflected shape of the wall is a function of the stiffness of the sheets relative to the stiffness of the soil. As the wall becomes more flexible relative to the soil, the position of the resultant passive force R_p , moves up, progressively reducing the applied maximum bending moments. Since the bending moment varies as the cube of the span, a large decrease in bending moment occurs with a small rise in the point of the resultant passive pressure.

As mentioned in chapter 2, Rowe (1952) developed a technique for reducing the maximum bending moment computed according to free earth support analysis, based on the flexibility number ρ of the sheet pile.

$$\rho = \frac{L^4}{EI} \quad 2.3$$

Where L is the total height of the sheet pile in meters, and EI is the flexural rigidity per meter of the sheet pile, EI is a constant through out this research, and its value is 494.871 KNm²/m. After computing the flexibility coefficient ρ , the reduction factor is read from Rowe's graph given in Figure 5.19. Figure 5.19 is for H/L ranging from 0.62-0.64, since the 16 cases fall in that range.

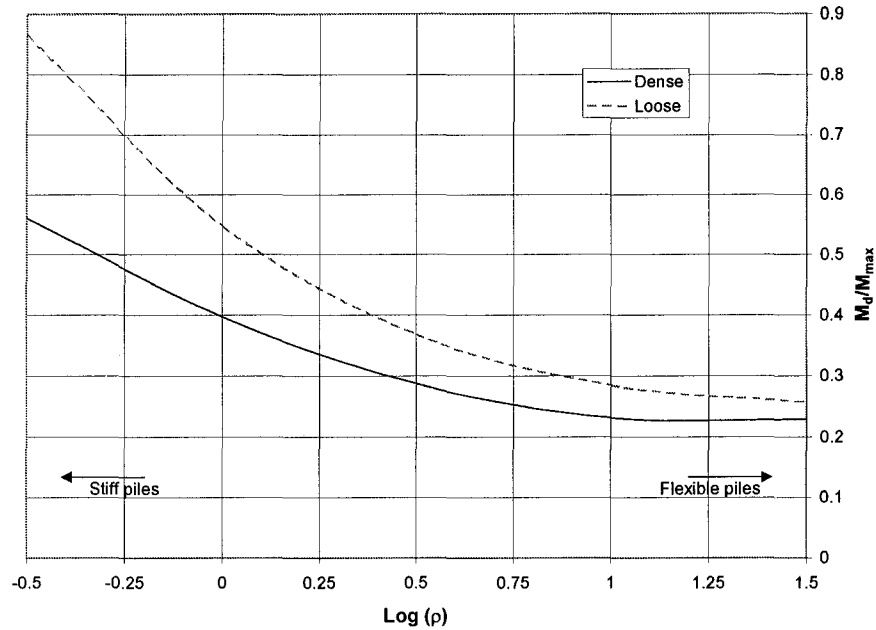


Figure 5.19: Rowe Reduction curves

M_d/M_{max} , for dense sand is:

$$\frac{M_d}{M_{max}} = -4.518 \times 10^{-4} \rho^3 + 0.108 \rho^2 - 0.2729 \rho + 0.397 \quad 5.58$$

Similarly, M_d/M_{max} for loose sand is:

$$\frac{M_d}{M_{max}} = -0.0546 \rho^3 + 0.274 \rho^2 - 0.483 \rho + 0.5479 \quad 5.59$$

The above two equations have restrictions, the flexibility coefficient, ρ , should not exceed the graph boundaries, ($0 < M_d/M_{max} < 1.0$). Referring to Table 5.1, the soil type used in the 16 cases is loose sand. Table 5.10 gives the corresponding reduction factors and the design reduced moments for the 16 cases. If the strength based design criterion is considered, these reduced maximum moments would be the actual design moments.

Table 5.10: Rowe's reduction corresponding to the 16 cases ($EI=494.871 \text{ KNm}^2/\text{m}$)

Case	Length (m)	$\rho=L^4/EI$ ($\text{m}^4/\text{KNm}^2/\text{m}$)	Log ρ	M_{max} (KNm/m)	V_{max} (KN/m)	Loose Sand	Design Moment (M_d)
						$R_M=M_d/M_{max}$	KNm/m
1	7.254	5.594	0.748	44.032	19.297	0.318	13.984
2	7.446	6.212	0.793	51.153	20.532	0.310	15.880
3	7.629	6.846	0.835	58.772	21.546	0.304	17.888
4	7.802	7.489	0.874	66.645	22.377	0.299	19.938
5	5.642	2.047	0.311	20.717	11.673	0.423	8.756
6	5.791	2.273	0.357	24.068	12.421	0.408	9.824
7	5.934	2.505	0.399	27.653	13.034	0.396	10.939
8	6.066	2.741	0.438	31.357	13.536	0.385	12.059
9	4.030	0.533	-0.273	7.550	5.956	0.702	5.297
10	4.137	0.592	-0.228	8.771	6.337	0.673	5.901
11	4.238	0.652	-0.186	10.076	6.650	0.647	6.524
12	4.335	0.713	-0.147	11.427	6.906	0.625	7.140
13	2.418	0.069	-1.161	1.631	2.144	1	1.631
14	2.482	0.077	-1.115	1.895	2.281	1	1.895
15	2.543	0.085	-1.073	2.177	2.394	1	2.177
16	2.601	0.092	-1.034	2.468	2.486	1	2.468

The reduced moment M_d will be used as design moment in calculating the maximum bending deflection. To compute the shear-induced deflection, the maximum shear force V_{max} should also be correspondingly reduced. Since the shear force has never been used in any design criteria, no work has been done for its reduction. It is assumed that the reduced V_{max} , $(V_{max})_R$, and the reduced M_{max} , $(M_{max})_R$ follow the same relationship of V_{max} and M_{max} before reduction. However, the relationship is not a nonlinear one.

Figure 5.20 shows the relationship between the unreduced maximum moment against the maximum shear force for the 16 cases. As is seen, each c/H ratio has its own curve. For convenience, one equation is obtained by curve fitting of all data points to approximate the relationship between V_{max} and M_{max} .

Hence for the reduced moment values, a corresponding reduced shear value can be determined by the same equation Equation 5.60

The equation of the fitted curve in Figure 5.21 is:

$$V_{\max} = 1.1859 + 0.5470 M_{\max} - 0.0034 (M_{\max})^2 \quad 5.60$$

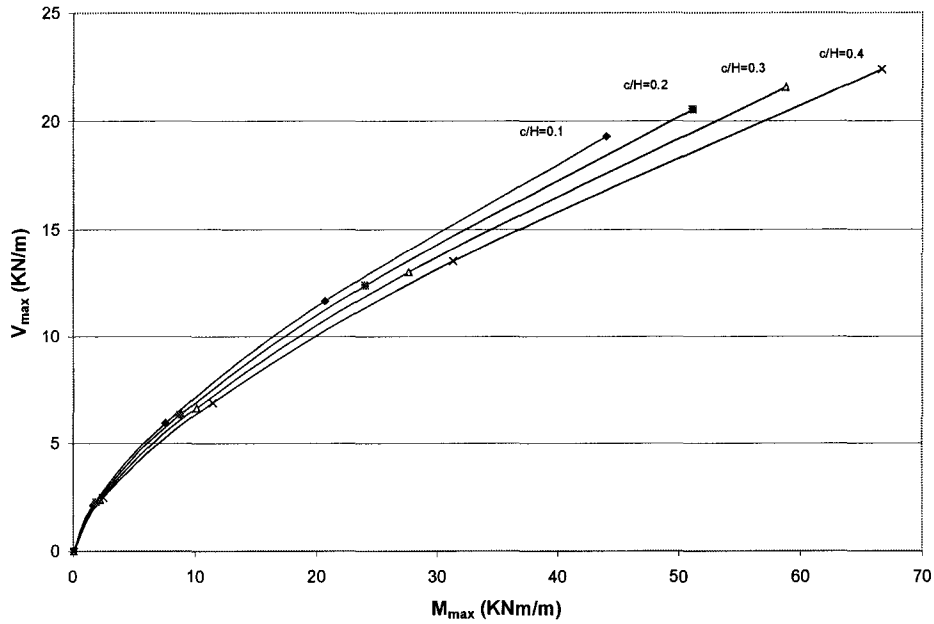


Figure 5.20: Maximum moment versus maximum shear for each c/H ratio

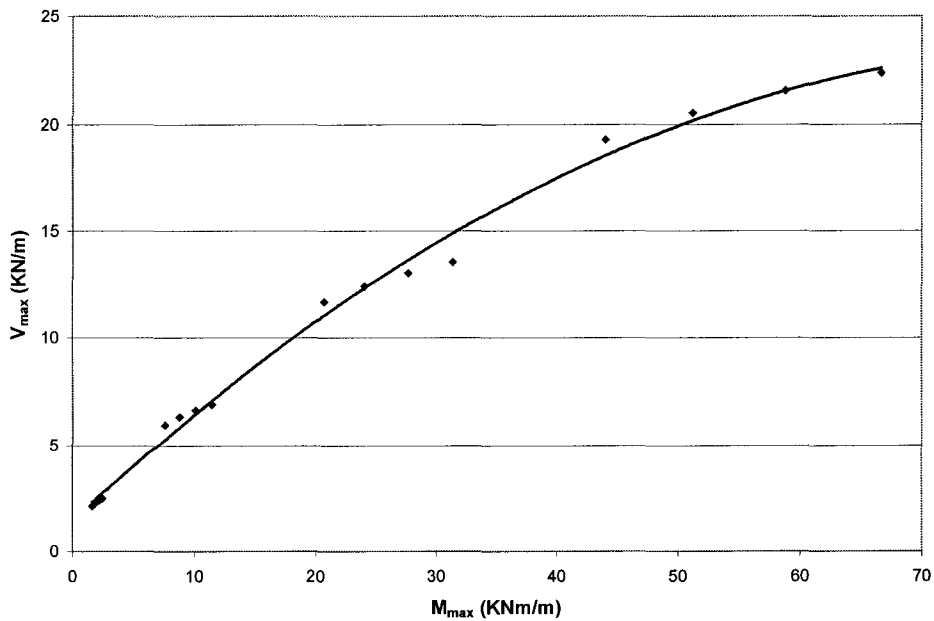


Figure 5.21: Maximum moment and shear relationship

5.9 Total Deflection of Sheet Pile Wall due Bending Moment and Shear Force

The total maximum deflection $(Y_{max})_{Total}$ can be written as the sum of $(Y_b)_{max}$ and $(Y_s)_{max}$ by equation 5.61. As is discussed in section 5.7 $(Y_b)_{max}$ and $(Y_s)_{max}$ do not lie at exactly the same depth, but very close. Thus summing the two deflection maximums gives a conservative estimate.

$$(Y_{max})_{Total} = (Y_b)_{max} + (Y_s)_{max} \quad 5.61$$

With Equations 5.48 and 5.57:

$$(Y_{max})_{Total} = \frac{(M_{max})_R L^2}{10.1EI} + \frac{(V_{max})_R L}{\alpha' KAG} \quad 5.62$$

Where

$(M_{max})_R$ is the reduced moment, and $(V_{max})_R$, is the reduced shear force from Equation 5.60, and α' is given by Equation 5.56.

Rearranging Equation 5.62 gives the deflection equation:

$$(Y_{max})_{Total} = \frac{(M_{max})_R L^2}{10.1EI} \left(1 + \frac{(V_{max})_R EI}{(M_{max})_R (KAG)L} \left(\frac{10.1}{\alpha'} \right) \right) \quad 5.63$$

Let

$$\xi = \frac{(V_{max})_R EI}{(M_{max})_R (KAG)L} \left(\frac{10.1}{\alpha'} \right) \quad 5.64$$

Then

$$(Y_{max})_{Total} = \frac{(M_{max})_R L^2}{10.1EI} (1 + \xi) \quad 5.65$$

The parameter, ξ , is proportional to the ratios of $(V_{max})_R/(M_{max})_R$, and $(EI)/(KAG)$, and is inversely proportional to the total wall length L , and reflects the shear contribution to the total deflection. Therefore, ξ can be considered as a shear factor, which is influenced by the shear force, the section rigidity and the wall height.

Since the values of $(V_{max})_R$ and $(M_{max})_R$ are load induced and are irrelevant of the sheet pile material used, the combination of the EI/KAG ratio and the total sheet pile height are the determining factors in reflecting the shear contribution to the deflection. By using Equation 5.64 the difference between a steel section and a composite section can be compared with respect to the effect of shear deflection. A steel section with the closest moment of inertia to the composite sheet pile was chosen.

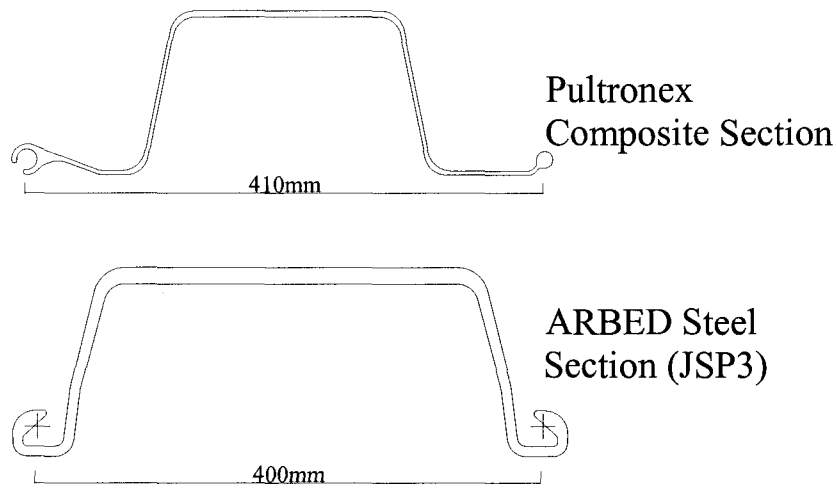


Figure 5.22: Composite and steel sections

For the composite section, $EI=494.871 \text{ KNm}^2/\text{m}$, $KAG =1492.924 \text{ KN/m}$ and thus Equation 5.64 became:

$$\xi_{composite} = \frac{(V_{max})_R}{(M_{max})_R} \frac{3.348}{L \alpha'} \quad 5.66$$

A steel section with similar moment of inertia was chosen:

$E=200\text{GPa}$, $G=77\text{GPa}$, assume $K=1$. Using AutoCAD 2000, the moment of inertia of the composite sheet pile was found $1840 \text{ cm}^4/\text{m}$. Thus, steel section JSP3 from

TRADE ARBED Canada Inc., with $A=191\text{cm}^2/\text{m}$, $I=16800\text{cm}^4/\text{m}$ (composite section $I=18410\text{cm}^4/\text{m}$) was chosen, (ξ) for steel became:

$$\xi_{steel} = \frac{(V_{max})_R}{(M_{max})_R L} \left(\frac{0.231}{\alpha'} \right) \quad 5.67$$

Since Rowe's reduction is material dependent, the values of $(V_{max})_R$ and $(M_{max})_R$ used in the steel sheet pile wall, are different from those used in the FRP composite wall. The moment reduction (M_d/M_{max}) has to be re-calculated for the 16 steel piling using equation 5.59. Accordingly, the corresponding reduced maximum shear is also calculated using Equation 5.62, Table 5.11 gives ρ , the moment reduction factors and the corresponding reduced moment and shear. For the wall height from 1.5 m to 4.5 m, steel sheet pile wall is relatively rigid, Thus Rowe's moment reduction is not applicable. Therefore, the reduction factors are all equal to one. A plot of shear factor ξ , for both steel and composite section versus the design length of sheet pile is shown in Figure 5.23. Obviously, shear effect on deflection is more significant in composite sheet pile wall.

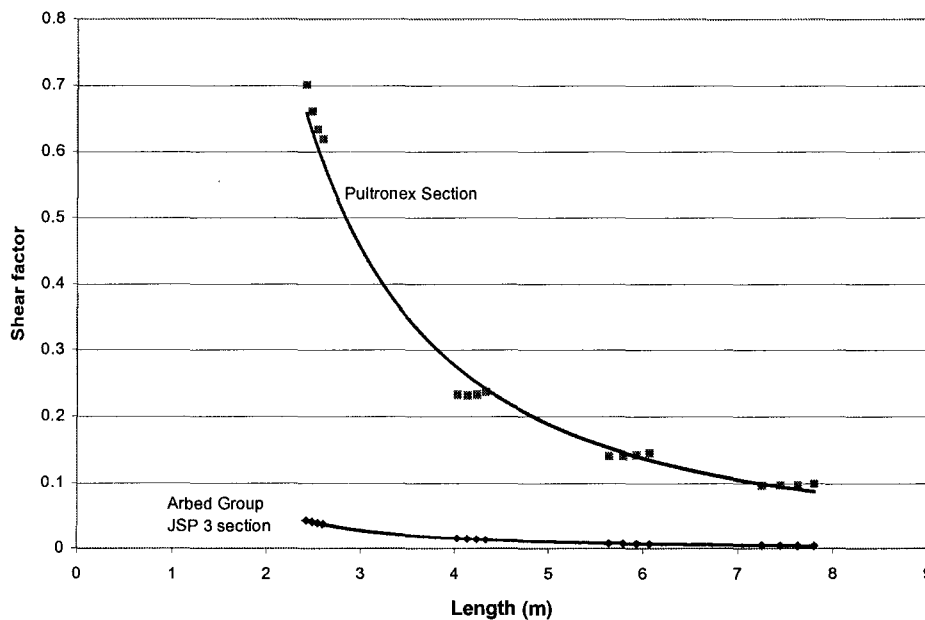


Figure 5.23: Comparison between a steel section (JSP 3) and a composite section on hand

Table 5.11: Steel section Maximum moment and shear reduction for steel section JSP3

Case	$\rho=L^4/EI$ (m^4/KNm^2 /m)	Log ρ	M_d/M_{max}	M_{max} (KNm/m)	M_d (KNm/m)	V_{max} (KN/m)
1	0.083	-1.083	1	44.032	44.032	19.297
2	0.092	-1.037	1	51.153	51.153	20.532
3	0.101	-0.995	1	58.772	58.772	21.546
4	0.111	-0.956	1	66.645	66.645	22.377
5	0.030	-1.519	1	20.717	20.717	11.673
6	0.034	-1.474	1	24.068	24.068	12.421
7	0.037	-1.432	1	27.653	27.653	13.034
8	0.040	-1.393	1	31.357	31.357	13.536
9	0.008	-2.104	1	7.550	7.550	5.956
10	0.009	-2.058	1	8.771	8.771	6.337
11	0.010	-2.016	1	10.078	10.078	6.650
12	0.011	-1.977	1	11.427	11.427	6.906
13	0.001	-2.992	1	1.631	1.631	2.144
14	0.001	-2.946	1	1.895	1.895	2.281
15	0.001	-2.904	1	2.177	2.177	2.394
16	0.001	-2.865	1	2.468	2.468	2.486

Chapter 6

The Design of Composite Sheet Pile Walls

6.1 Introduction

This chapter will apply Equation 5.65 to the design of composite sheet pile walls based on two deflection limits, $L/60$ and $L/100$. For the given sandy soil properties, ($\phi=32^\circ$, $\gamma'=9.68\text{KN/m}^3$, $\gamma=19.62\text{ KN/m}^3$), and the water level, (c/H ratio), 16 cases will be studied. With the correction of the active pressure, q_1 , the penetration depth, D , the maximum moment, M_{max} , and the anchor force T are first computed. Knowing M_{max} and the total length of the sheet pile ($L=H+D_d$), the design moment, $(M_{max})_R$, is found according to Rowe's reduction curve, and the maximum deflection $(Y_{max})_{Total}=(Y_b)_{max}(1+\xi)$ is calculated. The total deflection is then compared to the deflection limit given by the designer (e.g. $L/100$). If the deflection requirement is not satisfied then by trial and error, the penetration depth is increased until the deflection limit is satisfied. In Figure 6.1, a deflection-based design flow chart is presented in comparison with the traditional strength-based method.

6.2 Case Studies

The 16 design cases as listed in Table 5.3 will be used to demonstrate the proposed design method. The detailed procedure for Case 1 is given as an example. Case 1 has a wall height, H , of 4.5 m, a water depth, H_w , of 4.05 m, and the distance between the water level and the ground surface, c , was 0.45 m. Since the sheet pile is relatively short, the anchor is positioned at the top ($a=0$). The moist soil unit weight $\gamma=19.62\text{ KN/m}^3$, the effective soil unit weight $\gamma'=9.68\text{ KN/m}^3$, and the soil internal angle of friction $\phi=30^\circ$ (Figure 6.2). The deflection limit is set by $L/100$. Again for composite sheet piles manufactured by Pultronex Corporation, $EI=494.871\text{ KNm}^2/\text{m}$, and $KAG=1492.743\text{ KN/m}$

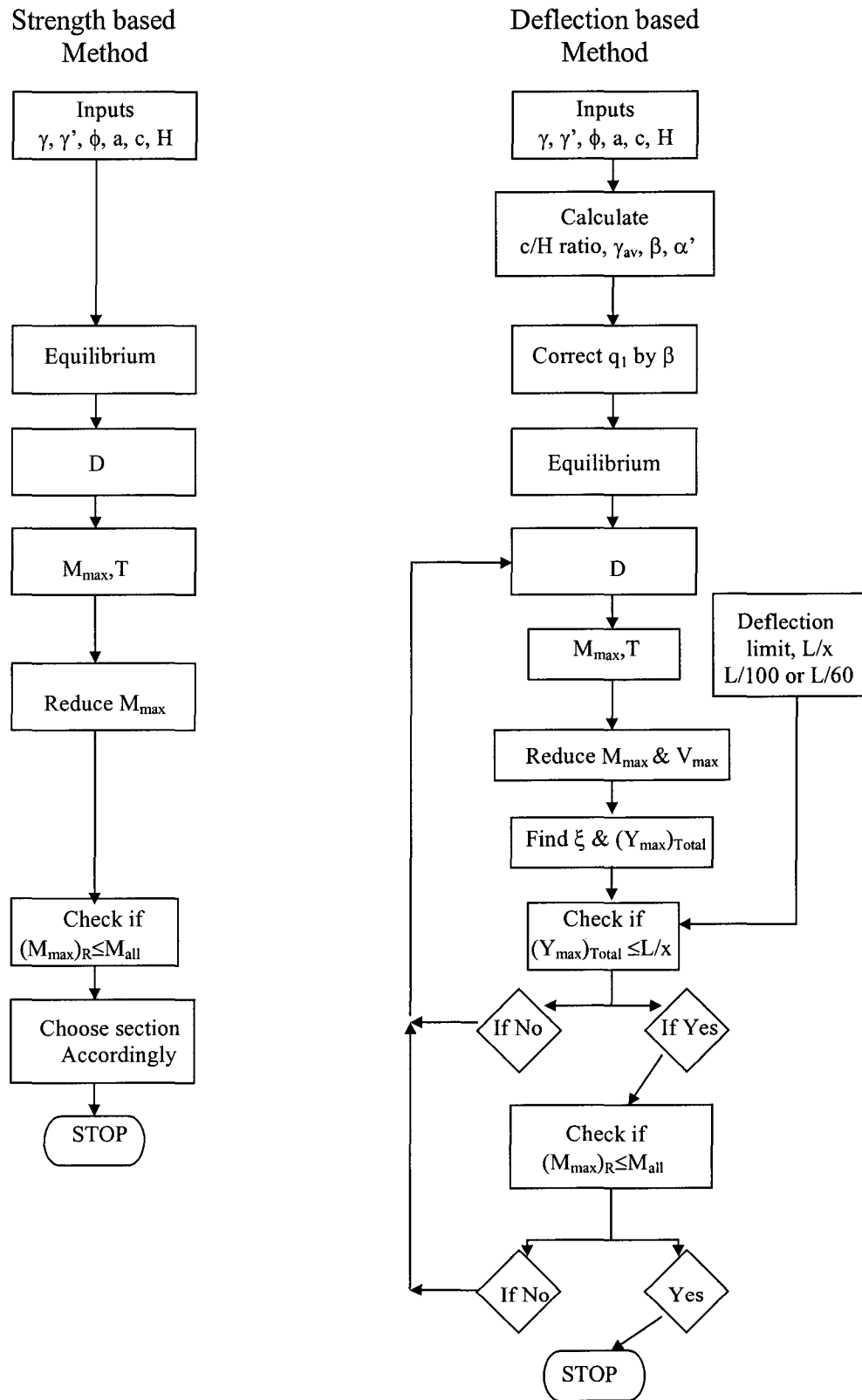


Figure 6.1: Comparison of deflection-based design with strength-based design

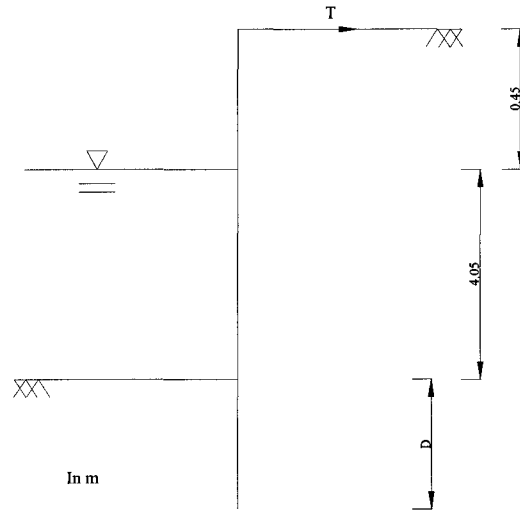


Figure 6.2: Design example (Case 1)

Knowing the internal friction angle, and using Equation 5.2:

$$K_a = \frac{1 - \sin 30}{1 + \sin 30} = 0.333, K_p = 3.0 \quad 6.1$$

Equation 5.23 is used to calculate the average unit weight:

$$\gamma_{av} = \frac{c\gamma + H_w\gamma'}{H} = \frac{0.45 \times 19.62 + 4.05 \times 9.68}{4.5} = 10.674 \text{ KN} / \text{m}^3 \quad 6.2$$

In order to find the correction factor β , the c/H has to be calculated;

$$\frac{c}{H} = \frac{1.2 \times 15.9}{3 \times 9.52} = 0.111 \quad 6.3$$

Thus, the correction factor β can be computed using Equation 5.30:

$$\beta = -0.1831 \left(\frac{c}{H} \right)^2 + 0.0866 \left(\frac{c}{H} \right) + 1 = 1.01336 \quad 6.4$$

With the β and the γ_{av} known, Equation 5.33 calculates the corrected, q_1^* :

$$q_1^* = q_1 \beta = 10.674 \times 0.333(4.5 + D) \times 1.013357 = 3.6055(3 + D) \quad 6.5$$

Similarly for q_2 :

$$q_2 = \gamma' \times K_p \times D = 9.68 \times 3 \times D = 29.04D \quad 6.6$$

The penetration depth, D , is found by trial and error, using Equation 5.7:

$$\sum M_{anchor} = \frac{q_1^*}{2} \times (H + D) \left(\frac{2}{3}(H + D) \right) - q_2 \frac{D}{2} \left(\left(\frac{2D}{3} \right) + H \right) = 0 \quad 6.7$$

Using Microsoft Excel solver, $D = 1.96$ meters

With the penetration depth, D , the anchor pull force can be computed from Equation 5.11:

$$T = R_a - R_p = q_1^* \frac{(H + D)}{2} - q_2 \frac{D}{2} = 19.436 \text{ KN} / \text{m} \quad 6.8$$

In order to find the maximum moment, the depth at which the shear is equal zero has to be found. Equation 5.31 is used, where x is the depth from the surface level.

$$x = \sqrt{\frac{(q_1(H + D) - q_2 D)(H + D)}{q_1^*}} = 3.2834 \text{ m} \quad 6.9$$

Knowing x , the maximum moment can be computed using Equation 5.32:

$$M_{max} = (q_1^*(H + D) - q_2 D)(x - a) - q_2 \frac{(x^3)}{6(H + D)} = 42.5453 \text{ KNm} / \text{m} \quad 6.10$$

The soil used in this example is loose sand, thus to obtain the reduced design moment M_d , Rowe's flexibility coefficient $\log \rho$ is computed:

$$\log \rho = \log \left(\frac{L^4}{EI} \right) = \left(\frac{7.27^4}{494.871} \right) = 0.7523 \quad 6.12$$

The reduction factor from Equation 5.59 is:

$$\frac{M_d}{M_{\max}} = -0.0546(\text{Log}\rho)^3 + 0.274(\log\rho)^2 - 0.483(\log\rho) + 0.5479 = 0.3169 \quad 6.13$$

In other words the maximum moment value has to be reduced by about 68.3% due the sheet pile flexibility. Using Equation 5.60 the corresponding reduced shear force is found. Thus the shear factor ξ is given by Equation 5.64:

$$\xi = \frac{(V_{\max})_R EI}{(M_{\max})_R (KAG)L} \left(\frac{10.1}{\alpha'} \right) = 0.0851 \quad 6.14$$

Given the deflection limit, $(L/100)$, the total deflection can be checked whether it satisfies the deflection criteria.

$$(Y_{\max})_{\text{Total}} = \frac{(M_{\max})_R L^2}{10.1EI} (1 + \xi) \leq \frac{L}{100} \quad 6.15$$

If Equation 6.15 is not satisfied the penetration depth, D , has to be increased by an increment until the criterion is satisfied. Increasing D will change the loading diagram, which in turn changes all the calculated values. Thus a loop is entered. The loop will be repeated until equation 6.15 is satisfied. For Case 1, $L= 7.27$ m, $(M_{\max})_R=13.48$ KNm/m.

$$(Y_{\max})_{\text{Total}} = 0.1545 \not\leq 0.07273 \quad 6.16$$

Therefore, Equation 6.15 is not satisfied, the penetration depth has to be increased. Using Microsoft Excel solver, the loop is performed until the criterion is satisfied. The final result gives $D=2.1747$ meters, $(D_d=D\sqrt{2}=3.0754$ m), and thus the total design length of the sheet pile L is 7.59 meters. The final step is to check that the maximum moment to be resisted is less than the allowable maximum moment. The maximum moment reached during the failure test, (which corresponds to $L/46$) was 13 KNm/m of wall. Thus the reduced maximum moment is less than the maximum allowable moment.

This procedure is repeated for all 16 cases, first with a deflection limit of L/100, and then with a less conservative limit of L/60. An over turning safety factor greater than 1 indicates that the deflection-based design dominated, and the loop calculation has been implemented. The penetration depths listed in Table 6.1 and 6.2 are not the design depths (i.e. not been multiplied by $\sqrt{2}$).

Table 6.1: Design of composite sheet pile wall using a deflection limit of L/100

Case	H (m)	D (m)	$(M_{max})_R$ (KNm/m)	T (KN/m)	$(Y_{max})_{Total}$ (m)	Over Turning Factor of safety
1	4.5	2.175	6.041	11.648	0.077	1.143
2	4.5	2.366	5.818	11.925	0.079	1.158
3	4.5	2.551	5.612	12.145	0.082	1.169
4	4.5	2.728	5.422	12.313	0.084	1.177
5	3.5	1.543	7.869	11.275	0.058	1.016
6	3.5	1.693	7.562	11.692	0.060	1.044
7	3.5	1.838	7.279	12.052	0.061	1.066
8	3.5	1.977	7.018	12.356	0.063	1.084
9	2.5	1.089	5.097	5.999	0.022	1.000
10	2.5	1.169	5.575	6.763	0.025	1.000
11	2.5	1.247	6.035	7.531	0.028	1.000
12	2.5	1.321	6.472	8.291	0.031	1.000
13	1.5	0.653	1.576	2.160	0.004	1.000
14	1.5	0.702	1.801	2.435	0.004	1.000
15	1.5	0.748	2.032	2.711	0.005	1.000
16	1.5	0.793	2.265	2.985	0.006	1.000

Table 6.2: Design of composite sheet pile wall using a deflection limit of L/60

Case	H (m)	D (m)	$(M_{max})_R$ (KNm/m)	T (KN/m)	$(Y_{max})_{Total}$ (m)	Over Turning Factor of safety
1	4.5	2.046	10.366	16.471	0.126	1.057
2	4.5	2.242	9.968	16.882	0.072	1.083
3	4.5	2.431	9.604	17.211	0.134	1.103
4	4.5	2.612	9.271	17.464	0.138	1.119
5	3.5	1.525	8.431	11.758	0.062	1.000
6	3.5	1.637	9.291	13.256	0.072	1.000
7	3.5	1.746	10.138	14.762	0.082	1.000
8	3.5	1.850	10.961	16.251	0.093	1.000
9	2.5	1.089	5.097	5.999	0.022	1.000
10	2.5	1.169	5.575	6.763	0.025	1.000
11	2.5	1.247	6.035	7.531	0.028	1.000
12	2.5	1.321	6.472	8.291	0.031	1.000
13	1.5	0.653	1.576	2.160	0.004	1.000
14	1.5	0.702	1.801	2.435	0.004	1.000
15	1.5	0.748	2.032	2.711	0.005	1.000
16	1.5	0.793	2.265	2.985	0.006	1.000

Based on Table 6.1 and 6.2, several design charts are developed for design engineers to conveniently adopt the deflection-based design method. Figure 6.3 and 6.4 show the design charts for penetration depth of composite wall versus the wall height H . The factor of safety, $\sqrt{2}$, has been used in both charts. For example, if a designer is to design a wall 3.0 meter high with a c/H ratio of 0.2 (i.e. water depth of 0.6m), and with the same soil properties used in the tables, the design depth, D_d , will be 2 m, for a deflection limit of L/100 (Figure 6.3), or 1.9 m for a limit of L/60 (Figure 6.4).

Figures 6.5 and 6.6 show design charts for the design maximum moment versus wall height. For a given wall height, H , and c/H ratio, using the charts, the designer can find the bending moment that will be carried by the wall.

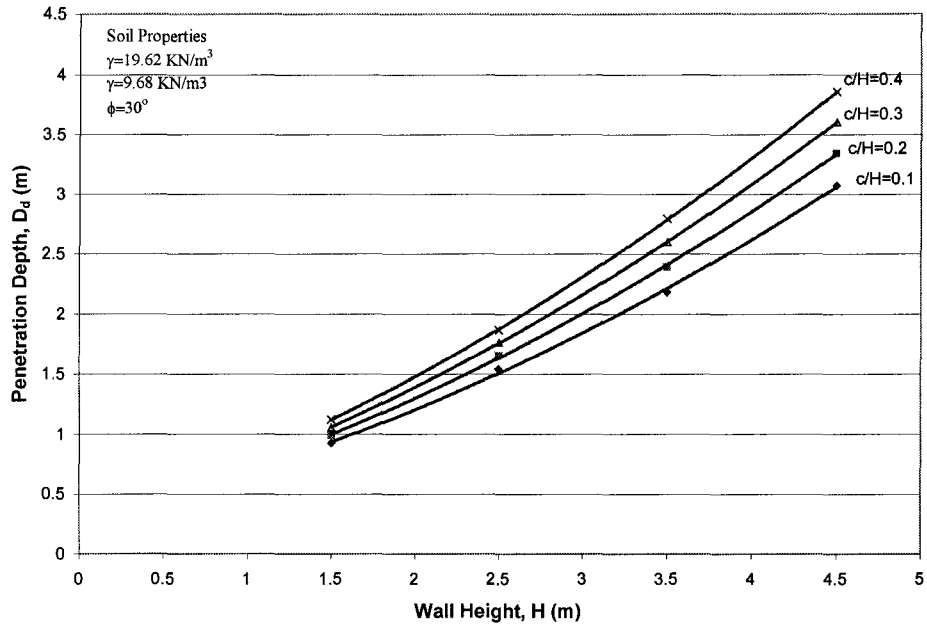


Figure 6.3: L/100 design chart for penetration depth

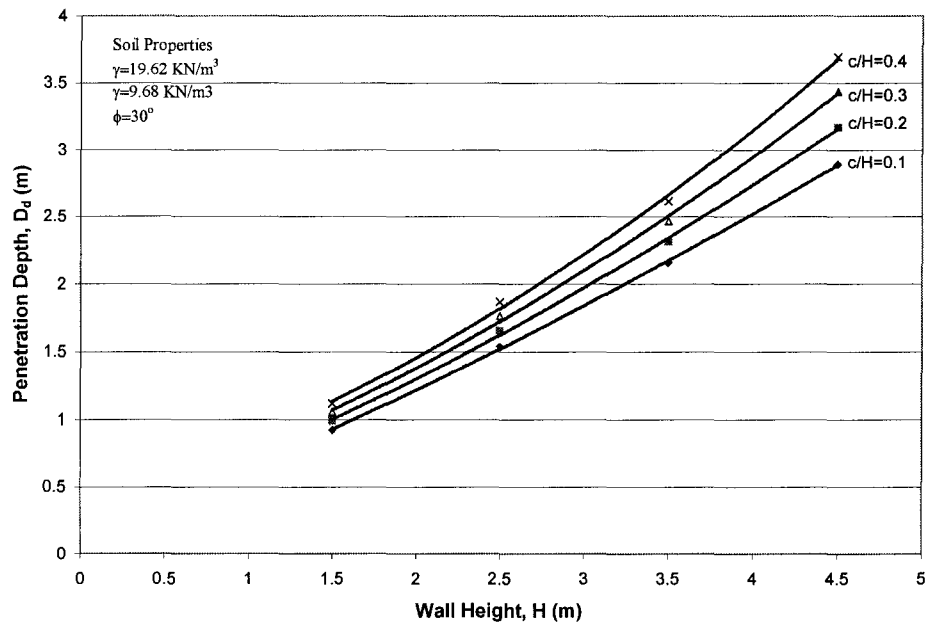


Figure 6.4: L/60 design chart for penetration depth

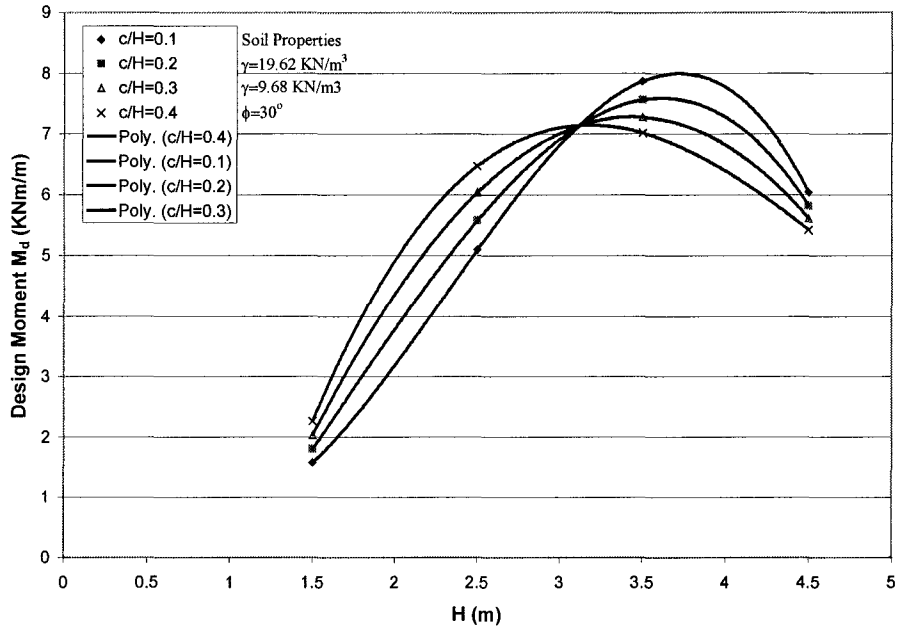


Figure 6.5: L/100 design chart for design moment

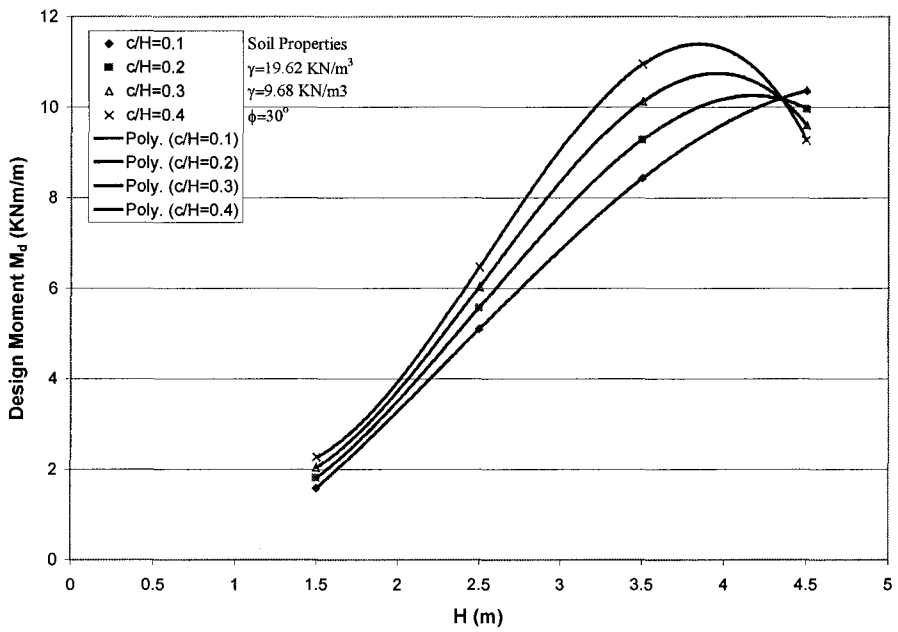


Figure 6.6: L/60 design chart for design moment

Increasing the wall height, H , will generally increase M_{max} . However a decrease in M_{max} is observed in the wall higher than 3m when using L/100 design limit, (Figure 6.5), and in the walls higher than 3.5 m when using L/60 design limit (Figure 6.6). This happens after the deflection-based design loop is implemented, which corresponds to the cases when overturning factors are larger than one. Since the criterion is not satisfied, increasing the penetration depth generates a reduction in M_{max} .

In the traditional free earth method, when solving for the penetration depth, D , the moment about the wall toe is set equal to zero, thus giving an overturning ratio of 1.0. Increasing the depth (deflection-based criterion) raises the factor of safety. In other words, the ratio between the resisting moment to the mobilizing moment is greater than unity.

Using Equation 5.65, the total maximum deflection for each case is calculated under both deflection criteria, L/100 and L/60. Figure 6.7, and 6.8 show the charts of maximum deflection versus wall height.

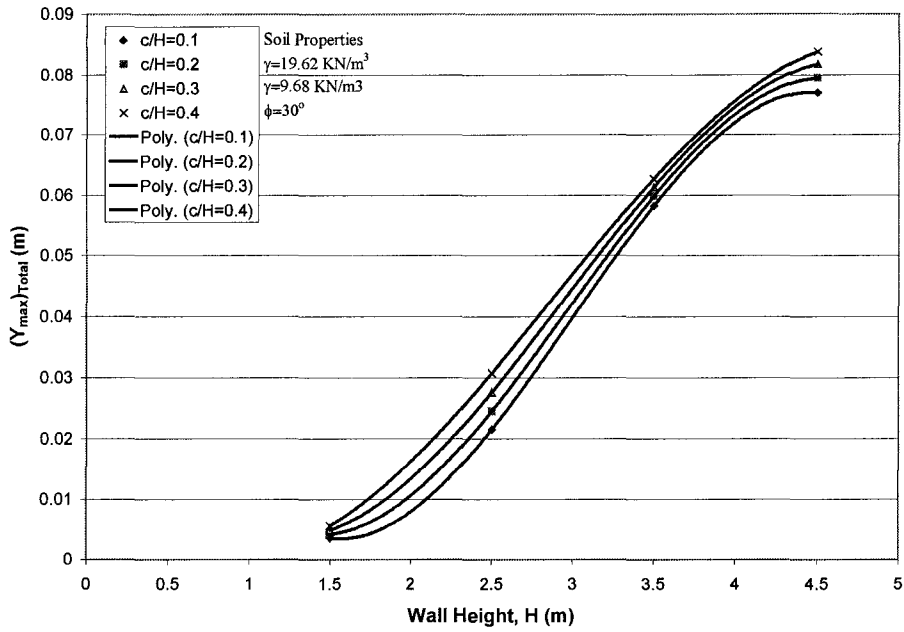


Figure 6.7: Total maximum deflection versus wall height (L/100)

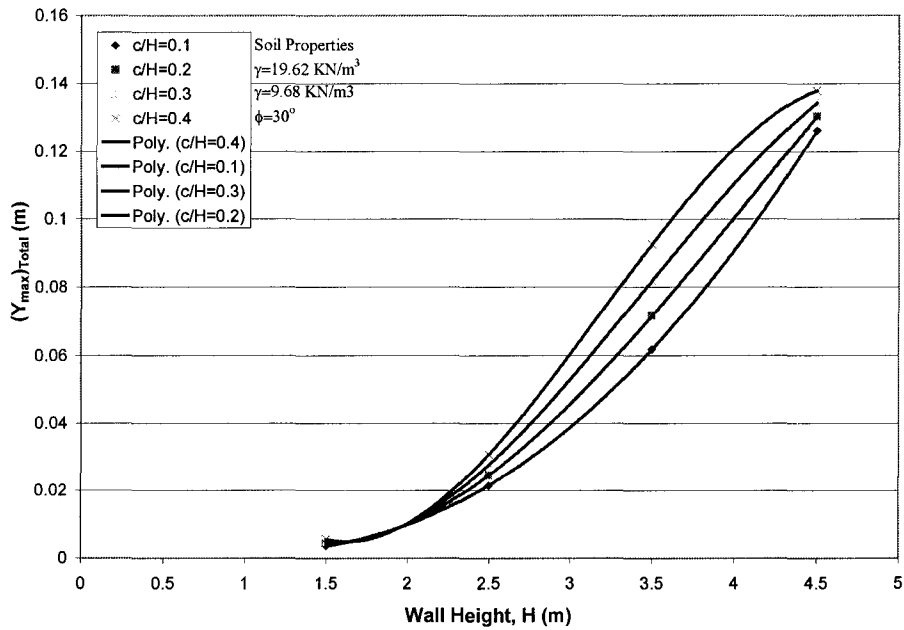


Figure 6.8: Total maximum deflection versus wall height (L/60)

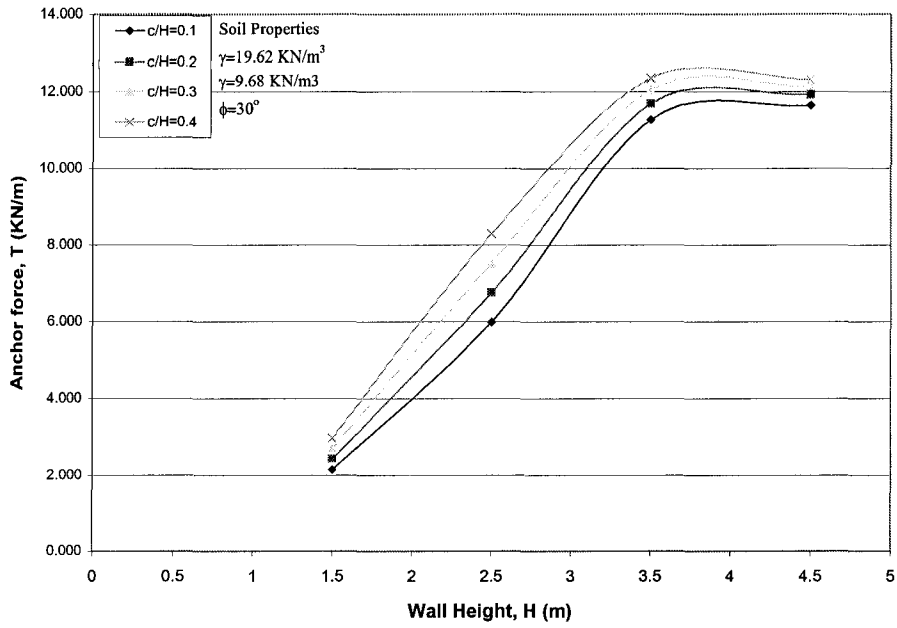


Figure 3.9: Anchor force versus wall height (L/100)

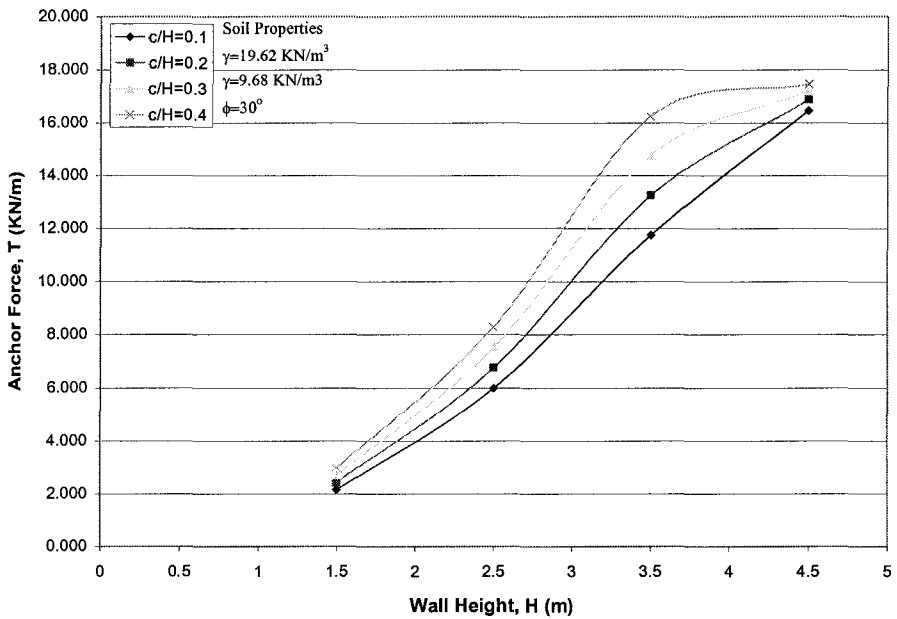


Figure 6.10: Anchor force versus wall height (L/60)

6.3 Comparison to Fixed earth support method

When the deflection limit was not satisfied, the loop calculation was carried out using a larger depth. This process positioned the deflection-based design between the two traditional methods: the free earth support method and the fixed earth support method. In the fixed earth support method, the sheet piling is considered flexible but driven to a sufficient depth that it may be considered fixed at its toe, and thus its resulting penetration depth is always greater than that obtained using the free earth support method. Reentering the loop means that the penetration depth will be larger than that by the free earth support method. Is this depth larger than that resulting from the fixed earth support method?

In order to make such a comparison, the 16 cases were re-calculated using the fixed earth support method. Table 6.3 gives the final result of the 16 cases using the fixed earth support method, also included in the table is the depth required using the proposed method for comparison. It is clear that the deflection-based design requires a depth of penetration smaller than that of the fixed earth method. The maximum moment computed using the fixed earth support method is higher than the design moment used by the free earth support method.

Table 6.3: Comparison with fixed earth support method

Case	Fixed earth support method			Proposed Method
	D (m)	M_{max} (KNm/m)	T (KN/m)	Deflection limit $L/100$ D (m)
1	3.137	32.786	17.672	2.175
2	3.528	37.563	20.595	2.366
3	3.922	42.080	22.964	2.551
4	4.316	46.192	24.837	2.728
5	2.321	16.731	11.259	1.543
6	2.617	19.160	13.113	1.693
7	2.916	21.465	14.630	1.838
8	3.216	23.579	15.842	1.977
9	1.491	6.831	6.176	1.089
10	1.691	7.843	7.201	1.169
11	1.896	8.808	8.052	1.247
12	2.102	9.701	8.745	1.321
13	0.612	1.623	2.363	0.653
14	0.680	1.912	2.799	0.702
15	0.820	2.189	3.170	0.748
16	0.932	2.450	3.483	0.793

Chapter 7

Discussion and Conclusion

A modified experimental procedure was used to simultaneously determine the flexural and shear rigidities of the fiber glass composite sheet piles. Some improvements were made to the previous testing setup [Giroux 2000]. Two connected panels were tested with eye end and pin end filled to simulate a connected sheet pile wall. Steel strapping was used to confine the panels, thus eliminating lateral deflection. The steel strapping uniformly distributed the stress, hence, local buckling or crushing was prevented.

The method involved testing varying span lengths (11 different spans) under 4-point bending loads at third span while recording the load-deflection data and the load-strain data. Linear load-deflection curves were plotted for the 11 spans. It was clear that flexibility is a function of the span for the same material. For a given load, a longer span would exhibit more deflection than a shorter one. These curves provided the information necessary to plot the δ/PL versus L^2 graph of which the slope was inversely proportional to the flexural rigidity (EI) and the intercept was inversely proportional to the shear rigidity (KAG). Comparing the results with Giroux's (2000), testing two connected panels did not effect the total deflection nor the strength of the sheet pile. Thus, the results obtained are representative of the sheet pile.

Eleven independent tests were conducted to obtain the flexural and shear rigidities. These were based on midpoint and quarter point deflection data under the four point bending tests. The values of the flexural and the shear rigidity determined from different cross-sections along the span (mid and quarter point) were in good agreement, indicating that the method used is suitable for this purpose.

The first part of Timoshenko's equation which only incorporate bending was plotted against the span to depth ratio, thus giving the relation of the apparent flexural rigidity and the span to depth ratio. As expected the apparent flexural rigidity varied with the span to depth ratio, indicating that indeed shear did have a significant effect on the

determination of EI . In both curves (mid and quarter point) the apparent flexural rigidity increased with the increase of the span to depth ratio. Both curves asymptotically reached the true flexural rigidity value but only after a span to depth ratio of about 55:1. Thus the suggested ratio of 16:1 by ASTM D790 was not suitable for composite sections, a similar conclusion was made by Zweben (1979) and Bank (1987), where both found that a ratio of at least 60:1 was needed to attain the true flexural rigidity value.

During data processing it was noticed that the flexural rigidity (EI) was insensitive to the span and the number of data points included in the linear fit. However, the value of the shear rigidity (KAG) varied depending on how the data points were processed. When only larger spans were included, KAG deviated, and its value increased. Therefore, it is conclusive that by using Timoshenko's two-term equation, EI can be determined consistently even with only three small-span tests. However to obtain KAG with reasonable accuracy, tests of different spans ranging from large to small are required. The small spans played an important role in obtaining a consistent KAG value.

The strain readings from the failure test were compared to strain readings from a uni-axial tensile coupon test of the same coupon material. It was observed that the tensile strains developed in composite sheet piles when excessively deflected to $L/46$ were only 14% of failure strains in uni-axial tensile coupons. Obviously, excessive deflection is a typical failure mode for this type of structure. Therefore, it is imperative to develop a deflection-based design method for composite sheet pile wall to complement the traditional strength-based design method.

Composites are flexible materials, their stiffness is much lower than that of steel or wood. As aforementioned, the flexibility depends on the span of the wall, it was Rowe (1952) who modeled such an observation. Rowe introduced a flexibility coefficient, which was directly dependent on the wall height raised to the power of 4 and inversely dependent on the material flexural rigidity. Since the combination of Rowe's model and the free earth support method provided for a variety of flexibility, it was chosen as the basic method for the deflection based design for FRP composite sheet pile wall.

The bilinear earth pressure distribution on the active side of the loading diagram was a rather complicated one when a deflection analysis was required. Thus a simplified loading diagram was proposed whereby the bilinear distribution is converted into a linear load distribution with a water level correction. The correction factor guaranteed a maximum moment with linear pressure diagram equivalent to that from bilinear load.

In order to introduce the deflection-based design, deflection equations were derived. Target equations were set, which related the maximum bending moment to the maximum bending deflection, as well as the maximum shear force to the maximum shear deflection. With the use of Rowe's moment reduction method, it was convenient to calculate the maximum deflection using reduced bending moment and shear force. In order to find the shear effect on the maximum deflection, the shear factor, ξ , was introduced.

Therefore, for a given deflection limit (L/x) that was set by the design engineer, the deflection generated by the bending moment and shear force is compared with the limit. If the deflection limit is not satisfied, the penetration depth will be increased, leading to the reduction in both maximum moment and deflection. Design graphs are developed for two deflection limits, $L/100$ and $L/60$. They are applicable only to the same soil conditions and top anchor position. To include all possible soil conditions and different anchor positions, more design charts are necessary or a computer software can be developed to produce the exact answer instead of forming the design charts.

For the currently practiced short wall (1.5 m - 3.5 m) with FRP composite sheet piling, the deflection based method designs a wall with height between that of the free-earth support method and the fixed earth support method. The benefit of having a deflection-based design for short wall is not obvious, as the difference in extra penetration depth is marginal. In the future however, with a better understanding of the composite material and more available field data, the composite sheet pile walls will be built taller, and the deflection-based design will become unavoidable.

References

ASTM (1998). "Standard Test Methods for Unreinforced and Reinforced Plastics and Electrical Insulating Materials". *ASTM D790-98*. pp. 148-156.

Bank, L. C. (1989). "Flexural and Shear Moduli of Full Section Fiber Reinforced Plastic (FRP) Pultruded Beams". *Journal of Testing and Evaluation*, Vol. 17, pp. 40-45.

Bank, L. C. (1987). "Shear Coefficient for Thin Walled Composite Beams". *Composite Structures*, 8, pp. 47-61.

Blum, H., (1955). "Berchnung einfach oder nicht verankerter spundwände in grundbau Taschenuch". *Berling Ernst*, 1:328-333

Bowles, J. E. (1996), Foundation Analysis and Design, 5th Edition., McGraw-Hill Book Co. New York, N.Y. 1996.

Brooks, R. J. and G. J. Truvey (1995). "Lateral Buckling of Pultruded FRP Shapes under Bending". *Composite: Part B*, 27B, pp.295-305.

"Canadian Foundation Engineering Manual"(1992). Canadian Geotechnical Society, 3rd Edition. Vancouver.

Cernica, J. N. (1995). "Geotechnical Engineering: Foundation Design". New York: Wiley, c1995, pp. 358-378.

Chambers, R. E. (1997). "ASCE Design Standard For Pultruded Fiber-Reinforced-Plastic (FRP) Structures". *Journal of Composites for Construction*, pp 26-38.

Clayton, C. R. I., Milititsky, J., Woods, R. I. (1993). “Earth Pressure and Earth-retaining Structures”. Glasgow, Blackie Academic & Professional, pp. 88-223.

Cornick, H. F. (1958). Dock and Harbour Engineering. London, C. Griffin & Co. Ltd. Pp. 80-104.

Das, B. M. (1995). “Principles of Foundation Engineering”. Boston: PWS Pub. Co., c1995, pp. 378-411.

Das, B. M. (1987). “Theoretical Foundation Engineering”. Amsterdam ; New York : Elsevier, pp. 131-159.

“Design of Sheet Pile Walls” (1996). Technical Engineering and Design Guides as Adapted from the US Army Corps of Engineers, No. 15. American Society of Civil Engineer.

Fisher, S., Roman, I., Harel, H., Marom, G., and Wagner H. D. (1981). “Simultaneous Determination of Shear and Young’s Moduli in Composites”. *Journal of Testing and Evaluation*, Vol. 9, pp. 303-307.

Giroux, C. (2000). “Analysis of the Flexural behaviour of a Fibreglass Composite Seawall”. McGill University, Montreal, Quebec.

Hagerty, D. J. and Nofal, M. M. (1992). “Design aids: anchored bulkheads in sand”. *Canadian Geotechnical Journal*. Vol. 29, pp. 789-795.

Henry, F. D. (1956). The design and construction of engineering foundations. New York, McGraw-Hill, 1956, pp273-281

Iskander, M. G. (1998). “State of the Practice Review in FRP composite Piling”. *Journal of Composites for Construction*, Vol. 2, pp. 116-120.

Kouadio, K. S.P. (2001). "Durability of Fiberglass Composite Sheet Piles in Water". McGill University, Montreal, Quebec.

Lampo, R., et al. (1998). "Development and Demonstration of FRP Composite Fender, Load bearing, and Sheet Piling Systems". *US Army Corps of Engineers Construction Engineering Research Laboratory Technical Report 98/123*. Septmeber 1998.

Lasebnik, G. Y. (1969). "Investigation of anchored sheet pile bulkheads". Ph.D. thesis, Kiev Politechnical Institue, Kiev, U.S.S.R.

Nagaraj, V., and GangaRao, V. S. (1997). "*Static Behavior of Pultruded GFRP Beams*". *Journal of Composites for Construction*, Vol. 1, pp. 120-129.

Nataraj, M. S. and Hoadley, P. G. (1984). "Design of Anchored Bulkheads in Sands". *Journal of Geotechnical Engineering*. Vol. 110, pp. 505-515.

Rowe, P. W. (1952). "Anchored Sheet-Pile Walls". *Proceedings of the Institute of Civil Engineering*, Vol. 1, pp.27-70.

Timoshenko, S. (1995). *Strength of Materials*. New York: Litton Educational Publishing, Inc. pp.170-175.

Tomlinson, M. J. (1994). Pile Design and Construction Practice, 4th Edition, E & FN Spon, London, UK, pp. 361-368.

Tschebotarioff, G. P. (1949), "Large Scale Model Earth Pressure Tests on Flexible Bulkheads", *Transactions of American Society of Civil Engineers*, Vol. 114, pp. 415-454.

Tsinker, G. P. (1997). Handbook of Port and Harbor Engineering: Geotechnical and Structural Aspects. New York : Chapman & Hall : International Thomson Pub., c1997, pp. 623-643.

Tsinker, G. P. (1983). "Anchored Sheet Pile Bulkheads: Design Practice". *Journal of Geotechnical Engineering*. Vol. 109, pp. 1021-1037.

Zweben, C., Smith, W. S., and Wardle, M. W. (1979). "Test Methods for Fiber Tensile Strength, Composite Flexural Modulus, and Properties of Fabric-Reinforced Laminates". *Composite Materials: Testing and Design (Fifth conference) ASTM*, pp. 228-262.

Appendix A.

For the proposed simplified pressure diagram (figure 1), the expected deflection profile is given in figure 2. The deflection at points A and B is equal to zero since they are hinges, the maximum deflection lies somewhere between point A and B at a distance 'x' from the left end.

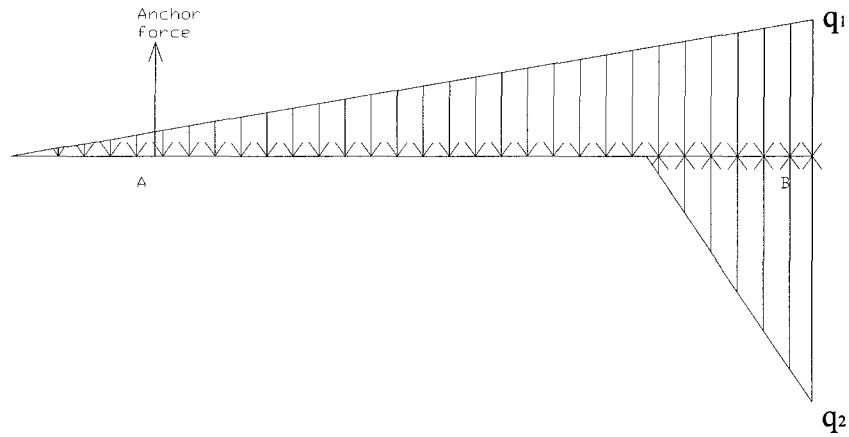


Figure 1: Simplified pressure loading diagram.

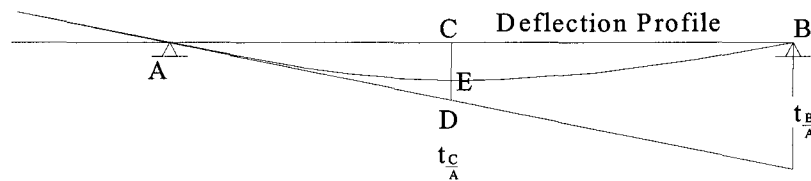


Figure 2: Deflection profile

In order to reach the required deflection equations, the moment and the shear diagrams have to be found. Breaking up the pressure diagram, the load can be analyzed in a more simplistic manner than dealing with the whole pressure diagram. The break up of the loading diagram is shown in Figure 3.

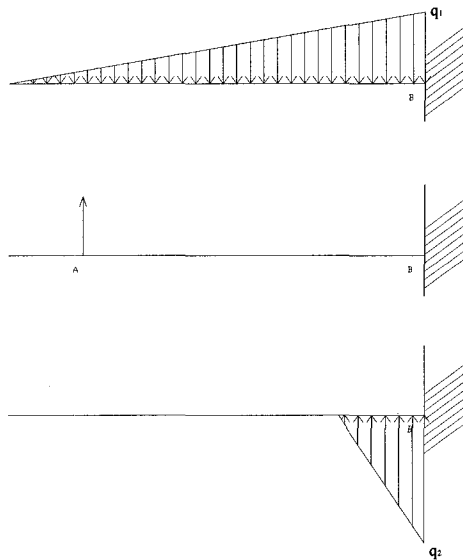


Figure 3: Break up of loading diagram

Bending Deflection:

The following three bending moment diagrams given in Figure 4, correspond to the three load diagrams given in Figure 3.

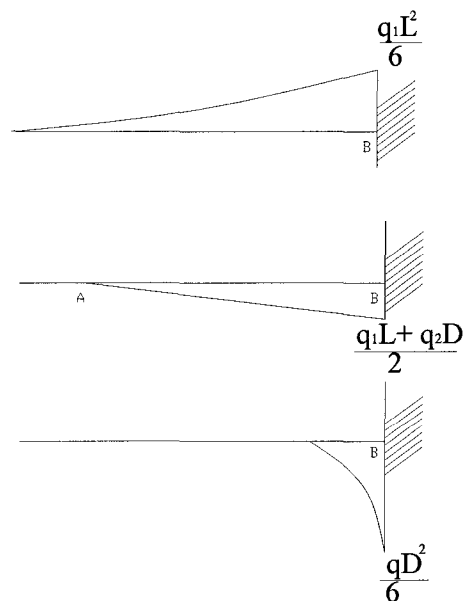


Figure 4: Moment diagrams corresponding to the load diagrams

From the principle of the moment area theorem, the vertical cord $T_{B/A}$ in Figure 2 is found by computing the product between the area under the moment diagram between point A and B and the distance from the area's centroid to point B. To facilitate the area computations the area in the first diagram in Figure 4 is segmented into two areas (as shown in Figure 5).

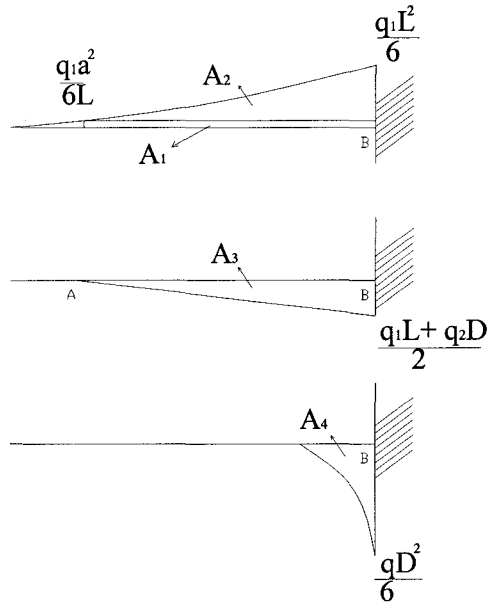


Figure 5: Segmenting of areas, to find the vertical cord

If 'A' denotes the area, and 'x' the distance between the area's centroid and the point B, then:

$$A_1 = \frac{qa^3(L-a)}{6L}$$

$$x_1 = \frac{(L-a)}{2}$$

$$A_2 = \frac{q_1}{6} \left(L^2 - \frac{a^3}{L} \right) \frac{(L-a)}{4}$$

$$A_2 = \frac{q_1}{24} \left(L^2 - \frac{a^3}{L} \right) (L-a)$$

$$x_2 = \frac{(L-a)}{5}$$

$$A_3 = \frac{(L-a)^2 (q_1L - q_2D)}{4}$$

$$x_3 = \frac{(L-a)}{3}$$

$$A4 = q_2 \frac{D^2}{6} \frac{D}{4} = \frac{q_2 D^3}{24}$$

$$t_{\frac{B}{A}} = A_1 x_1 + A_2 x_2 - A_3 x_3 - A_4 x_4$$

$$t_{\frac{B}{A}} = \frac{q_1 a^3}{12L} (L-a)^2 + \frac{q_1}{120} \left(L^2 - \frac{a^3}{L} \right) (L-a)^2 - \frac{1}{12} (L-a)^3 (q_1 L - q_2 D) - \frac{q_2 D^4}{120}$$

Using similar triangles:

$$\frac{CD}{x-a} = \frac{T_{\frac{B}{A}}}{L-a}$$

Thus:

$$CD = T_{\frac{B}{A}} \frac{(x-a)}{(L-a)}$$

$$CD = \frac{(x-a)}{12} \left[\frac{q_1 a^3}{L} (L-a) + \frac{q_1}{10} \left(L^2 - \frac{a^3}{L} \right) (L-a) - (L-a)^2 (q_1 L - q_2 D) - \frac{q_2 D^4}{10(L-a)} \right]$$

Since CD is known, the small vertical cord $T_{C/A}$ can be found, suppose point C is a distance x away from the left end, by which $a < x < H$. The area between point A, and C, for a given x is:

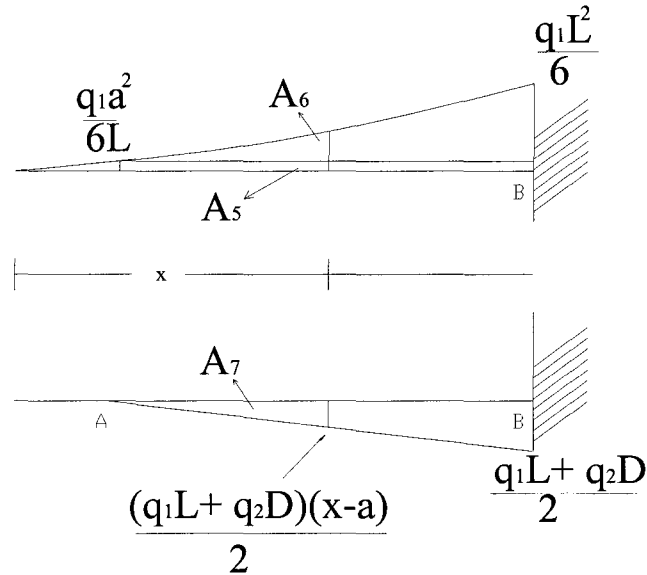


Figure 6: Area between C and A

$$\frac{T_C}{A}$$

$$A_5 = \frac{q_1 a^3}{6L}(x-a)$$

$$x_5 = \frac{(x-a)}{2}$$

$$A_6 = \frac{q_1}{6L}(x^3 - a^3) \frac{(x-a)}{4}$$

$$A_6 = \frac{q_1}{24L}(x^3 - a^3)(x-a)$$

$$x_6 = \frac{(x-a)}{5}$$

$$A_7 = \frac{1}{2}(q_1 L - q_2 D) \frac{(x-a)^2}{2}$$

$$x_7 = \frac{(x-a)}{3}$$

Since the third (last loading in Figure 5) diagram lies outside the region of interest:

$$A_8 = 0$$

$$x_8 = 0$$

Thus;

$$\frac{T_C}{A} = A_5 x_5 + A_6 x_6 - A_7 x_7$$

$$\frac{T_C}{A} = \frac{q_1 a^3}{12L}(x-a)^2 + \frac{q_1}{120L}(x^3 - a^3)(x-a)^2 - \frac{1}{12}(q_1 L - q_2 D)(x-a)^3$$

Since the bending deflection, $Y_b = CD - \frac{T_C}{A}$ then:

$$Y_b = \frac{1}{12EI}(x-a) \left[\frac{q_1 a^3}{L}(L-a) + \frac{q_1}{10} \left(L^2 - \frac{a^3}{L} \right) (L-a) - (L-a)^2 (q_1 L - q_2 D) - \frac{q_2 D^4}{10(L-a)} \right. \\ \left. - (x-a) \frac{q_1 a^3}{L} - \frac{q_1}{10L} (x^3 - a^3)(x-a) + (q_1 L - q_2 D)(x-a)^2 \right]$$

Shear Deflection:

$V(x)$ for $a < x < H$, thus the only the first two diagrams from Figure 3 are included in the analysis.

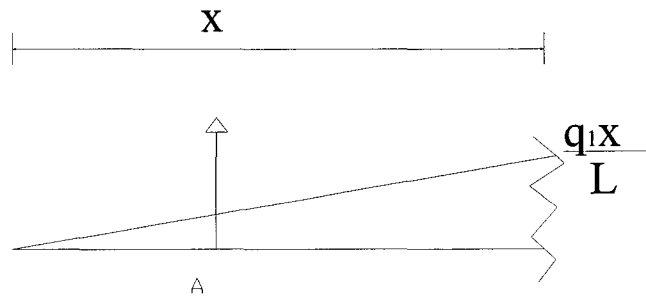


Figure 7: Shear value at a given distance x from the left end

From basic principles

$$\frac{dy}{dx} = \frac{V(x)}{KAG}$$

$$\int_0^{Y(x)} dy = \int_a^x \frac{V(x)}{KAG} dx$$

$$V(x) = q_1 \frac{x}{L} \frac{x}{2} - \frac{1}{2}(q_1 L - q_2 D)$$

$$V(x) = \frac{1}{2} \left[q_1 \frac{x^2}{L} - (q_1 L - q_2 D) \right]$$

$$Y_s = \frac{1}{2KAG} \int_a^x q x^2 - (q_1 L - q_2 D) dx$$

$$Y_s = \frac{1}{2KAG} \left[\frac{q}{3L} (x^3 - a^3) - (x - a)(q_1 L - q_2 D) \right]$$

Maximum Moment:

The maximum moment occurs at a depth 'x' where $\sum F = 0$, thus:

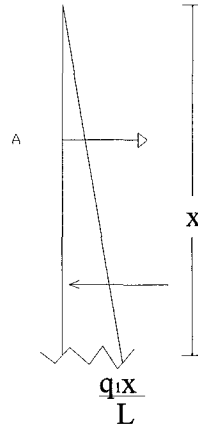


Figure 8: Location of maximum moment

Equating the soil pressure to the anchor pull force the depth x is found:

$$q_1 \frac{x}{L} \frac{x}{2} = \frac{1}{2} (q_1 L - q_2 D)$$

$$x = \sqrt{\frac{L(q_1 L - q_2 D)}{q_1}}$$

Moment at x = Mmax

$$M_{\max} = \frac{1}{2} \left[(q_1 L - q_2 D)(x - a) - q_1 \frac{x^3}{3L} \right]$$